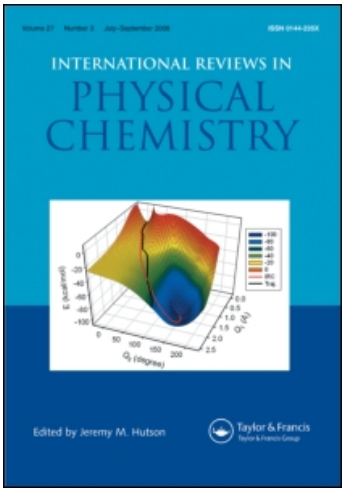

International Reviews in Physical Chemistry
Publication details, including instructions for authors and subscription information:
http://www.informaworld.com/smpp/title~content=t713724383

Photo induced three body decay

Christof Maul; Karl-Heinz Gericke

Online publication date: 26 November 2010

To cite this Article Maul, Christof and Gericke, Karl-Heinz(1997) 'Photo induced three body decay', International Reviews in Physical Chemistry, 16: 1, 1 — 79
To link to this Article: DOI: 10.1080/014423597230307
URL: http://dx.doi.org/10.1080/014423597230307

INTERNATIONAL REVIEWS IN PHYSICAL CHEMISTRY, 1997, VOL. 16, NO. 1, 1–79

Photo induced three body decay

by CHRISTOF MAUL† and KARL-HEINZ GERICKE

Institut für Physikalische und Theoretische Chemie der Johann Wolfgang Goethe-Universität, Marie-Curie-Straße 11, D-60439 Frankfurt/Main, Germany

The photo induced three body decay: $ABC + h\nu \rightarrow A + B + C$, where a molecule ABC decays into three fragments A, B and C upon irradiation, is reviewed. Various experimental and theoretical techniques for the investigation of this reaction and their application to a wide range of molecular species are discussed. Emphasis is laid on the distinction between concerted and stepwise processes, consisting of one single or two consecutive kinetic events, respectively. The concerted fragmentation scheme is further classified as being of either synchronous or asynchronous character, depending on whether or not the bond breaking processes take place in unison. The three body decays of acetone, azomethane and s-tetrazine are discussed in detail as prototypes for these mechanisms. A novel kinematic analysis approach, based on the evaluation of fragment kinetic energy distributions, is presented and applied to the ultraviolet photodissociation of phosgene. Competing pathways are found to be operative, dominated by the asynchronous concerted mechanism with preferential forward scattering of the carbon monoxide fragment. The synchronous concerted decay plays a minor role under significant excitation of the in-plane and out-of-plane bending modes of the parent molecule. Finally the power of the newly developed method for the analysis of the three body decay of a small polyatomic molecule is highlighted.

Contents

† Present address: Universidad de Puerto Rico, Recinto Río Piedras, Departamento de Química, Buzon 23346, San Juan P.R. 00931-3346, Puerto Rico, USA.

0144–235X/97 $12·00

1. Introduction

The issue of a concerted chemical reaction has interested the community of chemists for decades. Concertedness in this context means the breaking and making of different chemical bonds in a single kinetic event, as opposed to a sequence of individual reactions independently following each other. While the general existence of concerted reactions cannot seriously be doubted, there has been some fundamental disagreement in the past about the nature of such processes, especially in the field of organic chemistry [1, 2], triggered by the development of the theory of orbital symmetry by Woodward and Hoffmann in 1969 [3].

A challenging aspect of this subject, which is directly accessible to experimental investigation due to the relative simplicity of the studied systems, is three body photodissociation, where a molecule ABC is excited by absorbing a photon $h\nu$ at time t_0 and subsequently decays into three particles A, B and C:

$$\mathrm{ABC} + h\nu \xrightarrow{t_0} \mathrm{ABC}^* \rightarrow \mathrm{A} + \mathrm{B} + \mathrm{C}. \quad (1)$$

The use of A, B and C merely represents any final fragments and does not imply that these fragments are necessarily atomic. The simplicity of the system allows one to

obtain insight into the dynamics of concerted bond-breaking in a molecule. Therefore, the study of three body dissociation is of fundamental interest in the field of reaction dynamics. Apart from this fundamental aspect the results are important for understanding complex reaction schemes that, for example, govern atmospheric chemistry or combustion processes where the encounter of three collision partners is essential for many reactions.

Accordingly, after a relatively long period where three body decays have been regarded as a more or less exotic subject rarely ever touched, there has been a dramatic increase in the number of such studies in the last few years, a process that seems to have only just started if one takes into account the development of the last few months. Therefore, the objective of this review is twofold. The first aim is to compile and review existing data on three body decays, which has never systematically been done before. Secondly, we wish to present our own contributions to this interesting aspect of dissociation dynamics, which we hope will stimulate further investigation related to this tropic.

Since the discussion of concertedness has a long history, several phrases that have been used for its description do not always agree, or worse, have been used contradictorily. In this work we use the following expressions, based on terms that were originally developed by Dewar [2]. According to this system a *concerted decay* will take place in a single kinetic event as opposed to a *sequential decay* that is characterized by a sequence of two independent dissociation steps where the decay of AB is not influenced by forces from the first fragment C. We will define the kinetic event by a molecular time frame that manifests itself in the mean rotational period τ_{rot} of the primary intermediate decay product. Thus, a three body decay will be called sequential if the time span $\Delta t = t_2 - t_1$ between the times t_1 and t_2 of the first, resp. the second bond cleavage is greater than the mean rotational period of the primary fragment AB: $\Delta t \geqslant \tau_{\mathrm{rot}}$, and equation (1) may be rewritten as:

$$ABC + h\nu \xrightarrow{t_0} \mathrm{ABC}^* \xrightarrow{t_1} \mathrm{AB}^* + \mathrm{C} \xrightarrow{t_2} \mathrm{A} + \mathrm{B} + \mathrm{C}. \qquad (2)$$

Here, the asterisks indicate particles which are internally excited above their dissociation thresholds with respect to separation into final ground state fragments. As a consequence the orientation of the decaying primary fragment AB* at time t_2 carries no memory of the orientation of the excited parent ABC* at time t_1 apart from conservation of total angular momentum. The energy partitioning in the final fragments for a given set of quantum states is therefore governed by the conservation laws only.

As Δt becomes smaller than τ_{rot}, such a memory will be preserved, and the two decay processes are no longer independent of each other. This poses a geometrical constraint on the final products, in addition to the conservation laws, and leads to an energy partitioning in the fragments that is characteristic of the decay process. Thus, even chemically identical products A, B and C, in identical quantum states that have been generated via different decay mechanisms, are distinguishable by their energy content and their spatial distribution, both of which are experimentally observable physical properties.

Now consider a symmetric molecule ABA: As Δt approaches zero, the energy that is being transferred onto the products B + 2A will be identical for the two fragments A: all bond-breaking processes take place in unison [2]. Such a process is the

Table 1. Classification for sequential, concerted, synchronous and asynchronous mechanisms. The distinguishing criterion is the mean rotational period τ_{rot} of the intermediate fragment. Δt designates the time difference between the two bond cleavages.

	Three body decay process
$\Delta t/\tau_{rot} > 1$	Sequential
$\Delta t/\tau_{rot} < 1$	Concerted
$\Delta t/\tau_{rot} = 0$	Synchronous concerted
$0 < \Delta t/\tau_{rot} < 1$	Asynchronous concerted

asymptotic limit of the general concerted decay discussed above for vanishing Δt and will be called the *synchronous concerted* mechanism in order to distinguish it from the *asynchronous concerted* decay with $0 < \Delta t \leqslant \tau_{rot}$. The concept of synchronicity is not limited to symmetric molecules and can easily be generalized to any molecule ABC, provided the linear momenta transferred in the fragments A and C are identical.

Table 1 lists the vocabulary and definitions used for describing three body fragmentation processes. We will not use the terms 'simultaneous', 'instantaneous', or 'stepwise' for the characterization of the decay process since these terms have been used ambiguously before for distinguishing both between synchronicity and non-synchronicity and between concertedness and non-concertedness.

Some authors suggest using the vibrational period rather than the rotational period as the internal molecular clock for distinguishing between concertedness and non-concertedness [4–7]. The difference in the conceptual approach is smaller than it might appear at first sight. In order to distinguish between one single and two consecutive kinetic events one has to decide whether the second step is independent of the first one or if an influence from the departing first fragment is still being felt at the time when the second step takes place. In other words, the intermediate primary fragment AB may be called stable only if it has existed for a (however short) period of time without feeling the force of another particle C. The completion of a full rotation of the intermediate AB is a better criterion for stability in this sense then relating to vibrational or rotational periods of the intermediate that might not even be well known. We suggest using the mean rotational period as the distinguishing criterion, defined as the average time for completing a full rotation at a given rotational excitation which, in fact, has been the working criterion in many of the multiple photofragmentation studies. We prefer this criterion for a number of reasons. First, since the rotational energy transfer is taken into account, the stability criterion characterizes the fragmentation process rather than the intermediate particle AB as such, which is more appropriate for studying the nature of multiple photodissociation. Second, the stability criterion is related to an observable quantity rather than to a calculated property that depends on the geometry and the structure of the intermediate. Third, for polyatomic intermediate fragments the time difference between the different definitions becomes small due to the relatively long periods of the low energy vibrational modes and significant rotational excitation of the intermediate. Fourth, in cases where different criteria have been used no contradictory results have been obtained, even if the lifetime of the intermediate lies between its vibrational and its rotational period [7, 8]. Fifth, apart from the more general considerations outlined above, applying the vibrational criterion strictly leads to the classification of most asynchronous processes as being of intermediate rather than pure character [4] which makes it doubtful whether it can serve as a good operating criterion.

Regardless of whether the vibrational or the mean rotational criterion is thought to be appropriate to classify a three body decay, the vibrational period serves to illustrate the synchronous and asynchronous concerted mechanisms by decays via the symmetric and the anti-symmetric stretching modes of a linear ABC parent molecule, respectively [9]. In this picture the excitation of the symmetric stretching mode causes both bonds A–B and B–C to lengthen in phase, and both fragments will depart from the parent at exactly the same time, $\Delta t = 0$, characteristic for a synchronous decay. With the excitation of the antisymmetric stretching mode with vibrational period τ_{vib} the lengthening of one bond occurs together with contraction of the other. So the oscillations in bond length are phase shifted against each other, in this simple picture by 180°, and the second fragment will depart half a vibrational period later than the first one, $\Delta t = \tau_{vib}/2$, which is characteristic for an asynchronous decay. If the bond breaking itself is assumed to be an instantaneous process, then the energy transfer must be different for the two fragments because of the different 'collision partners' in the respective half-collision processes at times t_1 and t_2. One must bear in mind, however, that this picture is oversimplifying the process, even when the vibrational criterion is applied, and that the trajectories of the fragments on the potential energy surface that governs the fragmentation will be significantly more complex. Thus, the symmetric and antisymmetric pathways appear to be the simplest examples for synchronous and asynchronous concerted decays only.

Evidence of particles decaying into three fragments was found as early as the late 1920s, when the thermal and the light induced decomposition of azomethane [10, 11] and acetone [12] were studied. The nature of the dissociation mechanism was even addressed by indirect methods with respect to the appearance of stable intermediates. More recently the direct investigation of three body decays has been made possible (a) by the development of intense monochromatic light sources such as lasers and synchrotron radiation that allow the deposition of a large and well-defined amount of energy in a molecule; and (b) by novel experimental detection schemes that allow the direct observation of internal and kinetic energy distributions and spatial fragment distributions. These physical properties are characteristic for the process by which the fragments have been produced. Among these the most important scheme is photofragment translational spectroscopy (PTS) [13, 14] and its refinements [15, 16]. Another promising approach is coincidence measurements (photoelectron–photoion–photoion coincidence: PEPIPICO) [17] although so far their application is limited to the investigation of the dissociation of molecular ions and the detection of nascent ionic fragments. The most direct observations that can be made for rapidly dissociating systems have been performed in time-resolved picosecond or even femtosecond experiments where the fragment build-up is directly monitored [18, 19]. The refined experimental procedures appeared alongside the development of a number of theoretical models for describing various aspects of three body decays based on kinematic and statistical analyses.

The first part of this review, §§2–4, presents an overview of the most common experimental procedures and theoretical models that have been used to study three body decays, and of some of the most thoroughly investigated molecular systems. The second part, §§5 and 6, will summarize our own work, in which a kinematic model will be presented that is based on the evaluation of fragment kinetic energy distributions rather than angular distributions. Experimental results on the ultraviolet photodissociation of phosgene will be presented. The analysis according to our model will show that competing pathways are active, with the asynchronous concerted

mechanism being the major fragmentation channel. Finally, the applicability of the newly developed model will be discussed.

2. Experimental methods

In the sections below some typical experimental set-ups are described that are commonly employed in order to obtain data characterizing three body decays. There are numerous variations of these set-ups, and their applicability is by no means limited to the investigation of three body decays. A number of dissociation techniques for determining product state distributions have successfully been applied, e.g. laser induced fluorescence (LIF), resonance enhanced multiphoton ionization (REMPI), coherent anti-Stokes Raman scattering (CARS), chemiluminescence, etc.; but these techniques will not be discussed in more detail in this work.

2.1. *Photofragment translational spectroscopy*

The PTS method was developed in 1970 by Wilson and co-workers [13] and yielded for the first time the possibility of directly observing fragment kinetic energy distributions. In its original form it made use of a crossed laser–molecular beam apparatus, connected to a mass spectrometer, consisting of an electron impact ionization source, a mass filter and an ion detector in a fixed geometry [13]. Later set-ups have been improved by introducing the possibility of rotating either the mass spectrometer [20] or the molecular beam source [21]. Neutral photofragments are produced in the low pressure intersection region of the laser with the molecular beam and will travel under collision-free conditions with the fragment velocity obtained in the dissociation process, superimposed by the velocity of the molecular beam. The fraction of the photofragments that passes the entrance of the mass spectrometer becomes ionized and will be detected as a function of time of flight (TOF). The measured fragment property is the laboratory frame particle velocity. The standard PTS experiment is capable of detecting all fragment species, and the spatial anisotropy can be explored by changing the angle of the detector with the molecular beam and the laser polarization vector. The experimental set-up is blind, however, for product state distributions, and spatial and energy distributions are necessarily averaged over all product states. One has also to deal with signal contributions from the fragmentation of molecular ions of higher mass(es) that might significantly obscure the desired data. Kinetic energy distributions are obtained by transferring the laboratory time of flight data into the centre of mass system and finding the best distribution by the forward convolution method [22–24].

2.2. *Resonance enhanced multiphoton ionization–time of flight*

The two difficulties encountered in the PTS experiment can be circumvented by state-selectively ionizing the neutral fragments at the place where they are born via a resonant intermediate state with a second laser system [25, 26] and letting the ions rather than the neutrals move towards the particle detector [27, 28]. The resonance enhancement applies solely for a single selected state of the species under investigation, thus providing state selectivity and absence of fragmentation contributions. Otherwise the set-up is similar to the PTS experiment described above. The production of ions in the interaction region yields the additional advantage of being able to make use of all features provided by ion optical techniques. Applying an acceleration field, for instance, greatly enhances the number of particles incident on the detector, thus increasing signal intensity and improving the signal to noise ratio. Information on the

initial kinetic energy of a particle is then contained in the broadening of the respective TOF mass peak. The measured quantity in this case is the laboratory frame velocity component along the spectrometer axis instead of the velocity itself. Clearly, to obtain the three-dimensional velocity distribution, experiments under different detection geometries have to be performed.

Apart from the increased experimental effort, some other price has to be paid for obtaining the desired features as described before. In general, not all fragments will be accessible to observation, since an appropriate resonance state is required. Signal intensity and/or temporal resolution may be affected due to the fact that the charged particles are sensitive to space charge effects and stray fields. Data evaluation proceeds in analogy to the PTS experiments as long as the particles are detected after drifting with their initial velocity obtained in the dissociation process. If an acceleration field is applied the evaluation procedure has to be modified accordingly. Variations are too numerous to be listed here and depend on the type and geometry of the spectrometer design used. An example is presented in §6.

2.3. *High Rydberg time of flight*

A novel method that combines the advantages of PTS and REMPI–TOF is the high Rydberg time of flight (HRTOF) method first introduced by Welge and co-workers in 1990 [15]. The resonance enhanced ionization is spatially and temporally separated into two stages. A two-step excitation into a high-lying electronic Rydberg state of the species under investigation, via a resonant intermediate state, is performed in the interaction region. The ionization of the particle takes place later at the entrance to the mass spectrometer by field ionization. Thus, state selectivity and absence of fragmentation contributions are guaranteed and combined with a superb temporal resolution due to the insensitivity of the drifting particles to electrical perturbations. A variation of this method has recently been reported by Wodtke and co-workers who, instead of exciting the fragments into a Rydberg state, resonantly populate a metastable triplet state whose energy is sufficient to induce the emission of an electron when the excited fragment hits the detector [29]. Both refinements of the REMPI–TOF technique require highly sophisticated laboratory equipment, and their application is even more limited with respect to the choice of appropriate particles than the standard technique. The increase in temporal resolution that can be achieved with the two methods described in this section has to be compared to the ultimately achievable temporal resolution, which in photofragment spectroscopy is always limited by the temperature of the parent molecules in the molecular beam and by the ratio of the fragment masses [30]. In the light of this, both methods are ideally suited for observing light fragments in light–heavy half-collision processes. As a consequence the HRTOF method has so far only been applied for the detection of hydrogen and deuterium atoms, respectively.

2.4. *Photofragment imaging*

In another modification of the REMPI–TOF technique, pioneered by Chandler and Houston [31], the standard particle detector is replaced by a position-sensitive detector, e.g. by accelerating the electrons produced in a multichannel plate assembly onto a scintillating screen, where the resulting photons are accumulated in time, dependent on their position on the screen. Instead of measuring one velocity component along the spectrometer axis by the temporal deviation from the centre of the time of flight profile, the two velocity components perpendicular to the axis are monitored simultaneously by the spatial deviation from the axis. If the experimental

set-up is chosen such that the fragment distribution is rotationally symmetrical about an axis perpendicular to the spectrometer axis, the three-dimensional velocity distribution can be reconstructed by an Abel transform [32]. Whereas the latter requirement imposes restrictions on the polarization of the light interacting with the parent molecules as well as with the fragments, it yields very illustrative data on the fragment kinetic energies, especially for anisotropic fragment distributions. An extensive review of this method has recently been published [33].

2.5. *Coincidence measurements* (*PEPIPICO*)

The PEPIPICO method [17, 34–38] makes use of coincidence measurements of photofragments generated in the same dissociation event. So far, in the context of molecular photofragmentation, it has only been applied to the fragmentation of multiply ionized parent molecules. Light from a rare gas discharge lamp or synchrotron radiation, usually with a photon energy of 20–100 eV, is used to eject two photoelectrons in the parent molecule, which subsequently decay into two fragment ions and one neutral fragment. One of the photoelectrons is monitored and sets the zero point for the time of flight measurement of the photoions in a standard acceleration TOF spectrometer [39]. If both fragment ions are monitored, their respective TOF can be correlated with each other giving rise to a two-dimensional PEPIPICO spectrum. The magnitude of the flight time T for each ion identifies its mass, whereas the deviation ΔT of the flight time T from its nominal value T_0 (for an ion initially at rest) gives the initial momentum component p_{sp} of the ion along the mass spectrometer axis, $\Delta T \sim p_{sp}$. If the velocity projections onto the spectrometer axis of two fragments have been measured, the corresponding component of the third particle is unambiguously determined by the conservation of linear momentum.

If the flight times T_A and T_B of pairs of ions A^+ and B^+ are accumulated and plotted against each other, the contour of the peak is determined by the correlation of the momentum components $p_{sp,\,A}$ and $p_{sp,\,B}$. If a two body decay is investigated, it is obvious from momentum conservation that the two momentum components must be of equal magnitude and opposite sign, so the observed contour will be a straight line with negative unit slope centred around the time pair $(T_{0,A}, T_{0,B})$. The length of the line reflects the maximum flight time deviation, which depends on the energetics of the process, and is therefore determined by the conservation of energy. If a third fragment has to be taken into account, as is the case for a three body decay, energy and momentum conservation allow for a certain area in the TOF correlation diagram. Any specific contour or specific slope for the correlated TOF data therefore reflects restrictions imposed onto pairs of momentum components by the dissociation mechanism. For a synchronous concerted decay a characteristic oval contour is expected, whereas for a sequential decay with zero energy release in the second step a narrow bar will be observed with a negative slope given by the ratio of the mass of the observed fragment to the mass of the intermediate [5]. Analysing the observed peak contours with respect to their shapes and slopes and comparison to the predictions of dissociation models therefore yields information on the dynamics of the process [4, 40].

A most promising refinement of the PEPIPICO technique, although not yet implemented in reality, is the replacement of the conventional particle detector by a position sensitive detector [17]. Thus, instead of one momentum vector component, the complete momentum vector could be determined, one component from the time deviation ΔT, as before, and two by the position monitoring.

3. Theoretical methods

The general procedure for the analysis of a two body decay according to

$$XY + h\nu \rightarrow X + Y \tag{3}$$

is based on the evaluation of the energy balance in the centre of mass frame of the parent molecule XY:

$$E_{av} = E_{int}(XY) + h\nu - E_{diss}(X\text{–}Y) = E_{int}(X) + E_{kin}(X) + E_{int}(Y) + E_{kin}(Y), \tag{4}$$

where the E_{int} are the internal energies of the parent molecule and of the fragments prior to and after the decay, respectively, E_{kin} are the kinetic energies of the fragments, $h\nu$ is the photon energy, and E_{diss} is the dissociation energy of the parent. The available energy E_{av} is given by the sum of the well-characterized quantities on the left-hand side of equation (4). Observing the fragment X by a state-selective, kinetic energy sensitive method yields $E_{int}(X)$ and $E_{kin}(X)$, leaving $E_{int}(Y)$ and $E_{kin}(Y)$ as unknown quantities, which are unambiguously determined by the conservation laws for linear momentum and energy. It is not important whether fragment X or fragment Y is observed. Thus, performing such an experiment on either fragment from reaction (3) yields the complete information about all quantities in equation (4), and therefore provides a complete view of the dissociation process.

Analysing the three body decay (1) equivalently, one has to deal with two additional terms, $E_{int}(C)$ and $E_{kin}(C)$, on the right-hand side of the energy balance equation:

$$E_{av} = E_{int}(A) + E_{kin}(A) + E_{int}(B) + E_{kin}(B) + E_{int}(C) + E_{kin}(C). \tag{5}$$

Performing the same experiment as for the two body case again yields two energy values, e.g. $E_{int}(A)$ and $E_{kin}(A)$, but now one is left with four unknown quantities on the right-hand side of equation (5), only two of which are determined by the conservation laws. Therefore, contrary to the situation encountered for two body decays, one is confronted with the fact that the kinetic equations describing the fragmentation process are underdetermined. If no additional experimental information is obtained, eg. via coincidence measurements, one has to introduce dissociation models or make assumptions about partial or complete energy redistribution in the parent molecule prior to its decay.

3.1. *Kinematic analysis*

A common analysis of experimental data is based on a formalism of Herschbach [41, 42] that was originally developed for interpreting crossed molecular beam experiments. The aim was to understand the spatial fragment distribution in the centre of mass system of a long-lived collision complex with respect to the relative velocity vector of the reactants. In multiple photodissociation an analogous situation is encountered in the case of a sequential decay mechanism, characterized by equation (2), with the long-lived intermediate primary fragment AB* replacing the collision complex and the velocity vector $\mathbf{v}_{AB}$ replacing the reactants' relative velocity vector. The first application of this formalism to a multiple photodissociation problem was performed by Kroger and Riley in 1977 [43, 44]. Their analysis is subject to a restriction concerning the orientation of total angular momentum of the intermediate AB* in that it is confined to the plane perpendicular to the velocity vector. The spatial fragment distributions for various cases have been rigorously treated in a series of publications by Grice and co-workers [45–49] and were recently reviewed [50].

A general feature of the spatial fragment distribution $d\sigma/d\Omega$ after a sequential decay is the forward–backward symmetry:

$$\frac{d\sigma_A}{d\Omega}(\theta_A) = \frac{d\sigma_A}{d\Omega}(\theta_A - \pi), \tag{6}$$

where $d\sigma_A/d\Omega(\theta_A)$ denotes the signal intensity of the fragment A at an angle θ_A of the velocity vector $\mathbf{v}_A$ of fragment A in the centre of mass frame of the intermediate AB with the laboratory velocity vector $\mathbf{v}_{AB}$ of the intermediate AB itself. Since momentum conservation requires that $\theta_A + \theta_B = \pi$, the treatment of fragment B proceeds analogously, and nothing new can be learned by analysing the spatial distribution of B. Therefore in the following discussion we will restrict ourselves to looking at fragment A only and thus omit the subscript A. We will also follow the common convention of not explicitly expressing the dependence of the spatial fragment distribution on the azimuth angle ϕ. One must bear in mind, however, that the differential cross-section $d\sigma/d\Omega(\theta)$ actually means the signal intensity for a fixed value of ϕ when observing an ensemble of particles. We will denote this quantity as the scattering angle distribution as opposed to the decay angle distribution as defined below in equation (7). The use of the scattering angle definition gives rise to the so-called glory effect [51]: signal accumulation in the forward and backward direction. Apart from the transformation from laboratory to centre of mass coordinates this is the quantity observed in a PTS experiment as described above, if the signal is integrated in time. The signal intensity $d\sigma/d\theta(\theta)$ for all values of ϕ that will be used in the analysis in the second part of this work will be denoted for $f_\theta(\theta)$, the decay angle distribution, and is given by the integral:

$$f_\theta(\theta) = \frac{d\sigma}{d\theta}(\theta) = \int_0^{2\pi} \frac{d\sigma}{d\Omega}(\theta, \phi) \sin\theta \, d\phi, \tag{7}$$

which in the case of a symmetrical spatial distribution with respect to the intermediate velocity vector $\mathbf{v}_{AB}$ becomes

$$f_\theta(\theta) = 2\pi \sin\theta \, d\sigma/d\Omega(\theta). \tag{8}$$

Note that no glory effect is observed for $f_\theta(\theta) = d\sigma/d\theta(\theta)$. The explicit form of the spatial distribution $d\sigma/d\Omega(\theta)$ depends, other than the forward–backward symmetry which is always present, on the orientation of the total angular momentum vector $\mathbf{J}_{AB}$ with respect to the velocity vector $\mathbf{v}_{AB}$ of the intermediate AB, as described by the $\langle \mathbf{v}_{AB} \cdot \mathbf{J}_{AB} \rangle$ vector correlation [52]. For a purely isotropic decay, characterized by an equal probability for every possible orientation of $\mathbf{J}_{AB}$ with respect to $\mathbf{v}_{AB}$, i.e. $\langle \mathbf{v}_{AB} \cdot \mathbf{J}_{AB} \rangle = 0$, the distribution $d\sigma/d\Omega(\theta)$ will not show any dependence on the angle θ:

$$d\sigma/d\Omega(\theta) = \text{const.}, \quad \langle \mathbf{v}_{AB} \cdot \mathbf{J}_{AB} \rangle = 0. \tag{9}$$

A positive $\langle \mathbf{v}_{AB} \cdot \mathbf{J}_{AB} \rangle$ correlation indicating a preference for a parallel alignment of $\mathbf{J}_{AB}$ with respect to $\mathbf{v}_{AB}$ will cause the distribution $d\sigma/d\Omega(\theta)$ to show a maximum at $\theta = \pi/2$ with minima in the forward and backward directions, whereas a negative $\langle \mathbf{v}_{AB} \cdot \mathbf{J}_{AB} \rangle$ correlation will manifest itself in forward–backward peaking of $d\sigma/d\Omega(\theta)$ with a minimum at $\theta = \pi/2$ [50]. The latter case is often dealt with in reaction dynamics, not only in crossed molecular beam studies [41, 42], but also in photodissociations that produce an atomic fragment in the first step, which does not carry any angular momentum or that proceed in the impulsive limit [53] for other reasons. The impulsive dissociation should be understood as a process where an instantaneous

bond cleavage takes place, with forces acting between the two adjoining atoms only, while any other atoms remain spectators. Thus, nuclear rotation is generated with an angular momentum vector perpendicular to the recoil velocity vector of the molecule, and the inferred internal energy is determined by the mass ratio of spectators to actors. The significance of this case has led to the following considerations. If the $\mathbf{J}_{AB}$ vector is strictly constrained to lie within a plane of perpendicular orientation with respect to the velocity vector $\mathbf{v}_{AB}$, then in the classical limit without explicit ϕ dependence the fragment distribution is given by

$$\frac{d\sigma}{d\Omega}(\theta) = \frac{1}{4\pi^2 \sin\theta}, \quad \mathbf{J}_{AB} \perp \mathbf{v}_{AB}. \tag{10}$$

An intermediate case between the strictly perpendicular and the isotropic cases may be approximated by combining expressions (9) and (10) to yield

$$\frac{d\sigma}{d\Omega}(\theta) = \begin{cases} \text{const.} = c & 0 < \theta < \theta^*,\ \pi - \theta^* < \theta \to \pi \\ c\dfrac{\sin\theta^*}{\sin\theta} & \theta^* \leqslant \theta \leqslant \pi - \theta^* \end{cases} \qquad \langle \mathbf{v}_{AB} \cdot \mathbf{J}_{AB} \rangle < 0 \tag{11}$$

where c is a normalization constant. This expression has been widely used in analysing three body decays from the very beginning of kinematic analysis [43, 44] to date [54]. The parameter θ^* can be used to estimate the orientation of $\mathbf{J}_{AB}$ with respect to $\mathbf{v}_{AB}$, where $\theta^* \to \pi$ describes the isotropic limit, whereas the perpendicular limit is realized for $\theta^* \to 0$. Although the assumption of a negative $\langle \mathbf{v}_{AB} \cdot \mathbf{J}_{AB} \rangle$ correlation is not justified in general, it seems reasonable to use expression (11) as a trial distribution, if it yields good agreement between observed and calculated fragment distributions.

Besides determining the parameter θ^*, expression (11) can be used to verify if the dissociation proceeds via a long-lived intermediate. If this were not the case, then the forward–backward symmetry which is characteristic for a sequential decay mechanism regardless of the specific form of $d\sigma/d\Omega(\theta)$, would not be observed. A failure in achieving a satisfactory agreement between the observed and the calculated spatial fragment distributions on the basis of expression (11) may therefore be evidence of a concerted decay mechanism.

3.2. *Statistical unimolecular decay*

If the excited molecule ABC* lives for a considerable period of time before breaking apart, i.e. if its energy can be completely redistributed into all available degrees of freedom, then the statistical theory of unimolecular decay [55, 56] can be used to describe the decay of ABC* into the final fragments A, B and C [57]. The advantage of this approach is that under favourable conditions the observation of the mean kinetic and internal energies of the final products is sufficient to determine the fragmentation mechanism.

The decay is characterized by a temperature parameter $\beta = 1/kT$ according to the following considerations. For a statistical decay the available energy E_{av}, as defined in equation (4), is equipartitioned into the product degrees of freedom:

$$E_{av} = \frac{1}{2\beta}[3(f-1) + R + 2V - N], \tag{12}$$

where f denotes the number of fragments and R and V are the rotational and vibrational degrees of freedom, respectively. N accounts for a reduction in the

translational and rotational degrees of freedom for a decay into two or three fragments due to conservation of angular momentum and vanishes otherwise. The fractions f_{trans}, f_{rot} and f_{vib} $(0 \leqslant f_i \leqslant 1)$ of the available energy that are channelled into translational, rotational and vibrational energy are easily calculated from equation (12) by counting the respective degrees of freedom.

If a three body decay ($f = 3$) proceeds in concerted manner, R and V have to be determined with respect to the three final fragments A, B and C. The process will be characterized by a single temperature parameter β with E_{av} defined as the difference between the photon energy $h\nu$ and the dissociation energy E_{diss}(A–B–C) that is necessary to separate the ground state parent ABC into the final ground state fragments A, B and C, $E_{av} = h\nu - E_{diss}$(A–B–C), if the internal energy of the parent prior to the decay is negligibly small.

For a sequential decay the description is qualitatively different. According to reaction (2), two separate dissociations, each one into two fragments ($f_1 = f_2 = 2$), have to be considered:

$$\text{step 1:} \quad \mathrm{ABC}^* \xrightarrow{t_1} \mathrm{AB}^* + \mathrm{C} \tag{13a}$$

$$\text{step 2:} \quad \mathrm{AB}^* \xrightarrow{t_2} \mathrm{A} + \mathrm{B}. \tag{13b}$$

Each step is characterized by the respective degrees of freedom R_i and V_i $(i = 1, 2)$, by the appropriate value for the available energy $E_{av,\,i}$ and by a resulting individual temperature parameter β_i. The available energy for the first step is analogously defined as in the case of a concerted decay with E_{diss}(A–B–C) replaced by the dissociation energy E_{diss}(AB–C) that is necessary to produce the ground state intermediate AB and the ground state final product C:

$$E_{av,\,1} = h\nu - E_{diss}(\mathrm{AB–C}). \tag{14a}$$

The available energy for the second step is a result of the energy equipartitioning of the first step and is calculated from the difference between the internal excitation $E^*_{AB} = E_{rot}(\mathrm{AB}) + E_{vib}(\mathrm{AB})$ of the intermediate AB and the dissociation energy E_{diss}(A–B) that most be provided to separate the ground state intermediate AB into the ground state final products A and B:

$$E_{av,\,2} = E^*_{AB} - E_{diss}(\mathrm{A–B}). \tag{14b}$$

It is evident that the two procedures will yield different results for the translational as well as for the internal excitation of the final fragments. If, therefore, a three body decay is known to proceed statistically, then knowledge of the mean kinetic and internal energies may be sufficient to distinguish between a concerted and a sequential decay mechanism. This method has, for example, been applied to the multiphoton multifragmentation of benzene [58], for which a concerted dissociation of a superexcited molecule can be ruled out, and to the dissociation of ionic molecular clusters [59].

3.3 *Maximum entropy analysis*

The idea of this analysis [9, 60] is to determine the most likely joint probability distribution $P_j(q_A, q_B, q_C)$ that is consistent with the observed experimental data by maximizing the entropy of P_j by information theoretic techniques [61–63]. q_A is a shorthand notation for the electronic state, the vibrational state, the rotational state and the kinetic energy content of fragment A. q_B and q_C are defined analogously. The joint probability distribution is a matrix, the dimension of which depends on the

number and on the nature of the fragments and contains information on the chance that fragment A in the specific state q_A will coincidently be generated with fragment B in state q_B and fragment C in state q_C. Needless to say the joint probability distribution P_j is the ultimate datum that can be determined in reaction dynamics, since it contains virtually all information about the products of a reactive process. Nevertheless, its complexity prohibits the desirable direct experimental observation, although progress has been made in directly determining subdomains of P_j by experiment [29, 64–66]. This complexity is significantly reduced by replacing the fully quantum state resolved joint probability distribution P_j by the three-dimensional total energy joint probability matrix $P_j'(E_{tot}^A, E_{tot}^B, E_{tot}^C)$ that determines the probability of the coincident occurrence of three specific values of total fragment energies rather than the coincident occurrence of a set of specific quantum numbers for all fragments. E_{tot} is defined as the sum of all possible energy forms (electronic, vibrational, rotational and translational) of one fragment: $E_{tot} = E_{el} + E_{vib} + E_{rot} + E_{trans}$.

Once the most likely joint probability distribution has been determined from the experimental observations [67–70], all fragment properties that have not been experimentally observed may be predicted by a suitable projection method. Among them the angular fragment distribution $f(\theta) = d\sigma/d\theta(\theta)$ can be obtained, the knowledge of which in turn allows the discrimination of a sequential mechanism against a concerted one.

A maximum entropy analysis has been successfully performed for a number of multiple photodissociation events, among them the fragmentation of phosgene [71], carbon suboxide [9], s-tetrazine [9] and acetone [9, 72]. Although the conservation of angular momentum is not incorporated in the formalism, the maximum entropy analysis yields good agreement with the mechanisms determined by different methods. The reduction of the fully quantum state resolved joint probability distribution P_j to the total energy joint probability matrix P_j' is not always justified, however, and must be employed with some caution [72].

4. Applications to some molecular systems

There have been manifold applications of one or more of the above presented experimental and theoretical methods to molecular systems that decay upon irradiation into more than two fragments. In general every molecular system consisting of at least three atoms may exhibit such a behaviour, if enough energy is deposited into the parent. In this work we will focus on near-threshold three body decays and will therefore not consider systems for which the energy of the photon inducing the dissociation process is by one or several orders of magnitude larger than the energy of the bonds that are to be broken. Since the energy of a chemical bond lies in the range of several electron volts, usually light in the ultraviolet (UV) or in the vacuum ultraviolet (VUV) spectral region will suffice in order to start a near-threshold three body decay. There will be one exception, however: the soft X-ray double photoionization of molecules followed by the disintegration of the molecular ion. We feel that the coincidence measurements, employing this excitation scheme, are also a very powerful and promising tool for near-threshold systems. In fact, one such application has very recently been accomplished (§4.5) [73]. The experimental data presented in this section are compiled in table 2 for quick reference.

Table 2. Compilation of molecular systems that have been investigated with respect to their three body decay. In cases where a large number of studies exists, only the most recent ones are listed (for details consult the text in § 4).

Parent molecule	Products	λ (nm)	Method	Mechanism	Ref.
Azomethane	$N_2 + 2\,CH_3$	193	PTS	conc.	[54]
$(CH_3)_2N_2$		351	PTS	conc.	[79]
s-tetrazine	$N_2 + 2$ HCN	248 551	PTS	conc.	[97]
$C_2N_4H_2$		475–530	S-PES	conc.	[99]
triazine $C_3N_3H_3$	3 HCN	193 248	PTS	syn. conc.	[93]
acetone	$CO + 2CH_3$	193	PTS	seq./asyn. conc.	[91]
$(CH_3)_2CO$		193	IR	seq.	[72]
		193 248	PTS	seq.	[8]
		140 154[a]	TRS	seq.	[7]
acetyl iodide	$CH_3 + CO + I$	266	PTS	seq.	[43]
CH_3COI					
CF_3COI	$CF_3 + CO + I$	266	PTS	conc.	[44]
acetyl bromide	$CH_3 + CO + Br$	266 280	REMPI–TOF	seq.	[123]
CH_3COBr					
acetyl chloride	$CH_3 + CO + Cl$	236	PI	seq.	[122]
CH_3COCl		236	REMPI	seq.	[121]
phosgene	$CO + 2$ Cl	230	REMPI–TOF	asyn. conc.	[184][b]
$COCl_2$		235 237	REMPI–TOF	asyn. conc.	[71, 208]
thionyl chloride	$SO + 2$ Cl	193	LIF	conc.	[110]
$SOCl_2$		248	LIF	seq.	[110]
		193	PTS	conc.	[111, 113]
DMSO $(CH_3)_2SO$	$SO + 2\,CH_3$	193	REMPI, LIF	conc.	[114]
glyoxal	$H_2 + 2$ CO	440–460	VUV-LIF	conc.	[130]
$H_2C_2O_2$		440	PTS	conc.	[129]
water H_2O	$2H + O$	121·6	HRTOF	syn. conc.	[106]
ozone O_3	3 O	193	PTS		[108]

carbon suboxide C_3O_2	$C + 2\,CO$	157	VUV-LIF	seq.	[109]
methane	$CH + H_2 + H/$	121·6	RFS		[107]
CH_4	$CH_2 + 2\,H$	121·6	PTS		[132]
CF_2I_2	$CF_2 + 2\,I$	248–351	PTS	seq./syn. conc.	[135, 136]
$CFCl_3$	$CFCl + 2\,Cl$	106–200	EPA		[137]
CF_2Cl_2	$CF_2 + 2\,Cl$	106–200	EPA		[137]
		147–213	ES		[137]
CF_3Cl	$CF_2 + F + Cl$	147–213	ES		[137]
CH_2ICH_2OH	$I + OH + C_2H_4$	266	LIF	seq.	[140]
CH_2BrCH_2OH	$Br + OH + C_2H_4$	202	LIF	seq.	[140]
		193	PTS	seq.	[141]
CH_2ClCH_2OH	$Cl + OH + C_2H_4$	193	PTS	seq.	[141]
$Cd(CH_3)_2$	$Cd + 2\,CH_3$	UV	PI	asyn. conc.	[115]
$Hg(CH_3)_2$	$Hg + 2\,CH_3$	193 248	IRCL	seq.	[117]
Ar_3^+	$Ar^+ + 2\,Ar$	460–620	TOF		[142][c]
		532	PNPNCO		[73]
$HgCl_2^-$	$Hg + Cl + Cl^-$	0–7 eV	DEA	syn. conc.	[177, 178]
$HgBr_2^-$	$Hg + Br + Br^-$	0–7 eV	DEA	syn. conc.	[178]
ABC^{2+}	$A + B^+ + C^+$	10–60	PEPIPICO		[4][c]

[a] Two photon dissociation for $\lambda = 280$ nm, 307 nm.

[b] See also this work, § 6.

[c] See also references therein.

DEA: dissociative electron attachment; PNPNCO: photoneutral–photoneutral coincidence; IRCL: infrared chemiluminescence; ES: emission spectroscopy; EPA: end product analysis; RFS: resonance fluorescence spectroscopy; PI: photofragment imaging; S-PES: synchrotron photoelectron spectroscopy; IR: infrared spectroscopy.

4.1. *Azomethane—the asynchronous concerted case*

To our knowledge azomethane was the first molecule for which a three body decay was found to occur, from experimental evidence as early as 1929 [11]

$$H_3C{-}N_2{-}CH_3 \rightarrow 2\,CH_3 + N_2. \quad (15)$$

The endothermicity for reaction (15) originating from the azomethane S_0 ground state is 12040 cm^{-1}. Another 5425 cm^{-1} are required for the formation of the CH_3N_2 intermediate, the decay of which into the final products proceeds via a barrier with an estimated height of less than 850 cm^{-1}. Both sequential and concerted pathways are therefore energetically accessible after $\pi^* \leftarrow$ n excitation of the S_1 state of azomethane in the near UV region.

By comparing the heats of activation for differently substituted azoalkanes, Ramsperger was able to propose a concerted three body decay without formation of a stable intermediate CH_3N_2 [11]. For reasons of exactness we mention at this point that these experiments referred to thermal decomposition rather than to photodecomposition, which had been dealt with in an earlier experiment [10], although not under the aspect of multiple dissociation. As internal conversion into the electron S_0 ground state takes place after photoexcitation of azomethane into the S_1 state, this distinction should become insignificant. An extensive review of the early work on the decomposition of azoalkanes was given by Engel in 1980 [74].

Surprisingly in view of this history, azomethane has recently become a subject of renewed interest in the nature of its photodecomposition, as the question of the mechanism underlying the fragmentation has again been raised by contradictory experimental evidence. In a series of nanosecond time-resolved experiments, employing coherent anti-Stokes Raman scattering, Weisman and co-workers monitored product build-up times and vibrational and rotational state distributions of both CH_3 and N_2 fragments in the 355 nm photodissociation of azomethane [75–78]. From their observations they postulated a sequential decay mechanism that rapidly originates from the excited S_1 potential energy surface and produces a long-lived methyldiazenyl (CH_3N_2) intermediate. Lee and co-workers performed a PTS experiment dissociating azomethane at 351 nm [79], in which they observed a pronounced bimodal kinetic energy distribution for the methyl fragments, but were not able to observe methyldiazenyl nor any spatial anisotropy in the fragment distributions. The latter result led them to conclude that the lifetime of the photoexcited parent molecule is substantially longer than its rotational period. While the bimodality of the kinetic energy distribution in the methyl fragments is evidence against synchronous concertedness, modelling the distribution of the basis of a sequential mechanism resulted in violating forward–backward symmetry. Therefore they further concluded that the mechanism is of asynchronous concerted type with the second dissociation step being rapid and the first one being slow. Recent *ab initio* calculations [80] support this view, as well as experiments with more energy deposited into the parent by photodissociating at a wavelength of 193 nm, where the process is undoubtedly concerted [54]. The bimodality in the methyl kinetic energy distribution vanishes, and a synchronous mechanism might even be operative. Although the molecule has more than a 65 year history in three body photodissociation studies, research on this topic has not yet come to an end.

4.2. *Acetone—the sequential case*

The history of photodecomposition studies on acetone is almost as long as for azomethane and dates back to 1934, when Norrish and co-workers postulated a three body decay upon irradiation in the first absorption band [12]. The early photochemical work on acetone has been reviewed by Lee and Lewis [81]. The absorption spectrum of acetone [82, 83] consists of an unstructured continuum in the near ultraviolet extending from 220 nm to 320 nm which is due to the $\pi^* \leftarrow$ n excitation into the S_1 state. A second, structured absorption band extends below 220 nm into the VUV and is associated with the 3s $\leftarrow$ n excitation into the predissociating S_2 Rydberg state (84, 85]. The threshold wavelength for three body decay is 301 nm although a barrier in the three body exit channel causes three body decay to begin at wavelengths below 283 nm only [86]. At 248 nm the three body decay accounts for 30% of the total dissociation events [8]. The domain of three body decay of acetone is photon absorption into the second continuum, however. End product analysis [82, 87] proved a unity quantum yield for the reaction

$$(CH_3)_2CO + h\nu \rightarrow 2\,CH_3 + CO \tag{16}$$

at dissociation wavelengths below 200 nm. These results were confirmed by the failure to observe acetyl (CH_3CO) in a millisecond time-resolved absorption spectroscopy experiment [88]. While these studies could not yet answer the question for the decomposition mechanism, subsequent work in which product state distributions were determined by monitoring infrared emission of vibrationally excited fragments led to ruling out the synchronous concerted mechanism due to the large rotational excitation of the CO molecule [89, 90]. The authors argued that for a synchronous decay the angular momenta inferred onto the CO molecule by the departure of the methyl fragments tend to cancel each other. Indeed it appears very difficult, although not impossible, to explain the observed high rotational excitation of the CO molecule with a significant excitation of the out-of-plane bending modes in the parent molecule within a synchronous decay mechanism. The results of a refined experiment that allowed the direct observation of the fragments in their vibrational ground states by vacuum ultraviolet laser induced fluorescence (VUV LIF) (for CO) and REMPI (for CH_3) confirmed the earlier results [91] and could neither be explained on the grounds of statistical models [92–94] or by a synchronous concerted mechanism, or by a sequential decay with a rapid impulsive first step. The observed average kinetic energy of the CO fragment obtained from VUV LIF Doppler profile analysis [95] is much too large to be consistent with the predictions of the statistical methods, whereas for the synchronous mechanism, apart from less rotational excitation of the CO fragment, a higher kinetic energy for the methyl fragment and a lower kinetic energy for the CO fragment would be expected than those observed in the experiment. A similar analysis for a sequential decay with a rapid impulsive first step gives rise to inconsistency with the experiment in that the observed average methyl kinetic energy is too low. From these considerations and from a subsequent maximum entropy analysis [9] the authors concluded that the dominant mechanism should be considered to be asynchronous concerted with a mild preference only for the two methyl fragments to recoil in the same direction, thus actually constituting an intermediate case between concertedness and sequentiality. Later Hall and co-workers reinvestigated the acetone system by time-resolved diode laser absorption and gain spectroscopy in order to more completely determine the CH_3 internal state distribution than had been possible by the REMPI–TOF technique and found the methyl fragments to be vibrationally hotter by a significant amount than had been observed before [72]. They also reanalysed the

experimental results by the maximum entropy method with a less severe approximation than the reduction of the joint probability matrix $\mathbf{P}_j$ to total fragment energies. From their analysis they characterized acetone three body fragmentation to be purely sequential with a non-impulsive first fragmentation step.

So far, none of the experiments had especially been designed to address the nature of the three body decay. Only very recently was one such experiment performed by Lee and co-workers [8], confirming the results obtained before by more indirect methods. The kinetic energy distributions of all fragments were observed in a PTS experiment at dissociation wavelengths of 193 nm and 248 nm. Single TOF peaks for all fragments were observed, an experimental result hinting at a synchronous concerted dissociation when two chemically identical fragments are generated. However, an attempt to simulate the observed data on the basis of a synchronous decay mechanism failed. Thus, an asynchronous mechanism must operate that generates similar kinetic energy distributions for the two methyl fragments. By comparison with the kinetic energy data from the photodissociation of various acetyl halide compounds [43, 96] they concluded that a fully sequential mechanism is operative. They interpret their data successfully with what they call the barrier impulsive model, where the energy contained in the intermediate fragment is divided into a portion equal to the barrier height in the exit channel, which is impulsively distributed onto the final fragments, and a second portion exceeding the barrier height, which is statistically distributed among all degrees of freedom of the final products. A similar behaviour has been found for the three body photodissociation of s-tetrazine (§4.3) [97]. Although no results are presented on the lifetime of the parent molecule, the failure to observe any anisotropy in the spatial fragment distribution supports the view that the first bond cleavage (CH_3–CH_3CO) is not impulsive in character.

In addition to the studies of acetone photodissociation via the S_2 state discussed above, Zewail and co-workers recently investigated the photodissociation of acetone and its deuterated analogue in real-time by a femtosecond experiment with impressive temporal resolution, employing two-photon absorption into the 4s ← n Rydberg state of $(CH_3)_2CO$ at 280 nm and 307 nm [7]. They observed a fast decay of the parent and an equally fast build-up of the CH_3CO intermediate with a time constant of $\sim$ 50 fs, followed by a slower decay of the intermediate in the time range of 500 fs. Due to the higher available energies (the equivalent one-photon wavelengths would be 140 nm and 153·5 nm, the first one almost doubling the 193 nm value for the available energy) the results do not directly compare to the data discussed above. However, apart from the authors' assumption of an impulsive first step, which implies for the first CH_3 fragment a correspondingly low internal energy that is not observed in the S_2 dissociation, the picture of a sequential decay remains basically unchanged. The exit channel barrier discussed in some detail by Lee and co-workers [96] seems to be of negligible influence at these high energies.

Thus, as is also the case for azomethane, there is renewed interest in the three body photodissociation of acetone, making the molecule subject to recent investigation on the nature of the process.

4.3. *s-Tetrazine—the synchronous concerted case*

The photodecomposition of s-tetrazine into a nitrogen and two hydrogen cyanide molecules in their respective ground states:

$$C_2N_4H_2 \leftarrow N_2 + 2\,HCN, \tag{17}$$

is exothermic by 20160 cm^{-1} and requires a comparatively low activation energy of 16450 cm^{-1}. Sufficient energy to overcome the activation barrier may be deposited into the system by exciting the $^1B_{3u}(S_1)$ state, which lies 18130 cm^{-1} above the $^1A_g(S_0)$ ground state, corresponding to a $\pi^* \leftarrow n$ excitation at wavelengths below 551·6 nm. The three body photodissociation was first proposed by Hochstrasser and King [97] and has later been confirmed by numerous experimental [98–104] and theoretical [9, 105] investigations. Contrary to earlier observations [100] no bimodality in any one fragment kinetic energy distribution in the photodissociation of s-tetrazine has been observed [97] in PTS experiments at 248 nm and at 551 nm, corresponding to initially exciting the $^1B_{2u}$ and the $^1B_{3u}$ states, respectively. The authors developed a kinematic model, calculating the kinetic energy distributions from the geometry of the recoiling fragments, taking into account conservation of linear momentum and energy, which led them to propose a concerted decay mechanism. The most probable angles of the recoil direction of the fragments with respect to each other, and the width of this angular distribution, served as parameters to fit the model to the experimental data. They obtained a symmetric geometry for the transition state with decreasing HCN–HCN recoil angle for increasing energy of the photolysing photon. From the similarity of the fragment kinetic energy distributions at the different photolysis wavelengths they concluded that both dissociation events proceed on the same potential energy surface of the electronic ^1A_g ground state after internal conversion from the respective initially excited states, with the mean fragment kinetic energy reflecting the barrier height in the exit channel [105]. The HCN–HCN recoil angle decrease is ascribed to a strong HCN–HCN repulsion which is likely to distort the transition state geometry more easily if more excess energy is deposited in the parent molecule. An attempt to interpret these observations on the basis of a sequential decay mechanism was unsuccessful in that the velocity vectors of the second step would have to be strongly correlated in order to reproduce the observed data, which by definition cannot be the case for a sequential decay. The internal conversion from the initially excited potential energy surface is fast compared to the subsequent three body dissociation at either wavelength and, thus, there is sufficient time to redistribute the energy before the bond breaking takes place. The observation of an anisotropic fragment angular distribution in the photodissociation at 248 nm, however, is evidence of a drastically reduced lifetime of s-tetrazine after internal conversion to the ground state. RRKM calculations suggest a decrease in lifetime from 50 ns at an excitation wavelength of 551 nm to less than 1 ps at an excitation wavelength of 248 nm. Very cold fragment vibrational state distributions of N_2 and HCN have been monitored by synchrotron radiation photoelectron spectroscopy [99] and agree closely with the findings of Zhao *et al.* [98] in that the only significantly populated vibrational excitation is the HCN bending mode. A maximum entropy analysis [9] resulted in proposing not only a concerted, but also a synchronous, mechanism which is fully consistent with the experimental observations.

4.4. *Other molecular systems*

In this section we will consider some molecules exhibiting three body decay, either because of their fundamental simplicity or their abundance in everyday life and/or in chemical laboratories, because of their historical importance in three body decay studies or because of their importance with respect to their role in reaction chains.

The first group includes molecules such as water, ozone and ammonia. Direct or indirect evidence for the occurrence of three body decays has been observed in detail

for the following dissociation processes: the photodissociation of water at 121·6 nm [106, 107], ozone at 193 nm [108], ammonia at 121·6 nm [107], carbon suboxide (C_3O_2) at 157 nm [109], thionyl chloride ($SOCl_2$) at 193 nm and 248 nm [110–113] and dimethyl sulphoxide ($SO(CH_3)_2$) at 193 nm [114]. This list does not aim to be complete, but seeks to demonstrate the large bandwidth and the abundance of molecular systems exhibiting three body decay. For some of the reactions mentioned above the three body channel is of minor importance and has only been considered in order to explain deviations from the expected behaviour of the system producing two fragments. Since the three body decay has not been the focus of the investigation, none or only scarce data are available on the dynamics of this channel. A wealth of information is waiting to be gathered for these systems.

In the second, historical, group, we will consider, in the chronological order in which the results were published, the three body decays of various metal dimethyl compounds, of acetyl iodide (CH_3COI) and its fluorinated analogue trifluoroacetyl iodide (CF_3COI), and of glyoxal ($H_2C_2O_2$).

Some of the earliest work on three body photodissociation was inspired by a photofragment imaging experiment on the dissociation of cadmium dimethyl ($Cd(CH_3)_2$) [115], in which the authors reported a three body decay via the asymmetric stretching mode of the parent molecule. A number of later publications have addressed the same or similar systems (in general $Me(CH_3)_2$ with Me = Cd, Hg, Zn), by performing trajectory calculations or chemiluminescence experiments monitoring the fragment internal state distributions [116–119]. Although the applied models are very simple due to the confinement to linear geometries, these early investigations have attracted the attention of scientists to the issue of three body decay.

The investigation of a three body decay focused on the dynamics of the process for the first time in the PTS experiments of Kroger and Riley on the photodissociation of CH_3COI [43] and CF_3COI [44]. The results that they derived from the data of the 266 nm photodissociation of CH_3COI were interpreted as due to a sequential decay mechanism via a highly internally excited, long-lived intermediate CH_3CO particle:

$$CH_3COI + h\nu \rightarrow CH_3CO^* + I \rightarrow CH_3 + CO + I. \qquad (18)$$

Their analysis was carried out according to the kinematic procedure described in §3.1, employing an angular distribution according to equation (11). Their results were confirmed by the satisfactory agreement with the predictions of a statistical model based on the unimolecular decay of the intermediate CH_3CO. The observed anisotropy in the angular distribution of the final fragments was found to result from the first step in the sequential mechanism, implying that this step is fast compared to the rotational period of the parent molecule. The anisotropy is consequently carried over onto the final fragments, influencing the heavy and therefore slow CO fragment to a higher degree than the lighter and faster CH_3. In order to verify the mechanism by complementary data, the authors performed the same experiment on the fluorinated species CF_3COI. The anisotropy behaviour should have been reversed when substituting the light hydrogen atoms in the methyl group by heavy fluorine atoms, because the higher mass should have reduced the speed of the CF_3 fragment to lower values than the speed of the CO fragments, thus giving rise to a more pronounced anisotropy for CF_3 than for CO. The expected anisotropy change has, however, not been observed at all—on the contrary, the angular distribution of the corresponding fragments was virtually unchanged. The kinematic analysis on the basis of a sequential decay mechanism was no longer applicable, and the authors concluded that the

substitution of methyl by trifluoromethyl changed the reaction mechanism from sequential to concerted:

$$CF_3COI + h\nu \rightarrow CF_3 + CO + I. \tag{19}$$

This change might be due to a fast rotational predissociation of CF_3CO due to its large moment of inertia giving rise to large rotational excitation. This unexpected behaviour demonstrates the complexity of three body decays and illustrates that the kinematic model described in §3.1 is applicable only for a sequential decay process and fails to correctly describe the concerted mechanism.

As is the case of the three molecules that were discussed in some detail in the preceding sections, some very recent experiments have investigated the three body decays of the acetyl halides CH_3COCl [120–122] and CH_3COBr [123]. The remarkable photofragment imaging experiments of Hess and co-workers have yielded the most complete set of experimental data for a three body decay to date. All studies agree in proposing sequential decay mechanisms similar to the one presented above for the CH_3COI molecule.

Although the photochemistry of glyoxal ($H_2C_2O_2$) had been addressed very early [124, 125], what makes the molecule unique in the context of this work is a theoretical investigation [126, 127] explaining earlier experimental results [128] by the contribution of the concerted three body decay according to

$$H–CO–CO–H + h\nu \rightarrow H_2 + 2\,CO, \tag{20}$$

which was designated the 'triple whammy'. The authors calculated a planar transition state on the electronic ground state potential energy surface that leads to the synchronous formation of two CO molecules and one H_2 molecule from the terminating H atoms via a bending mode. Inspired by this work Lee and co-workers were able to identify the contribution of this channel to be 28% as compared to the main dissociation channel (65%) leading to $H_2CO + CO$ [129]. These findings have been confirmed in a later experiment monitoring the internal state distributions of the CO and H_2 fragments [130].

The third group deals with the photodecomposition of pure and halogenated alkane and alcohol compounds. The nature of these photodissociation process is not only of interest for the physical chemistry researcher, but also bears consequences for the composition of the atmospheres of distant moons and planets, as far as methane is concerned, and, for whom this might still not seem 'important' enough, for changes in the composition of the atmosphere of our own planet, as far as chlorofluorocarbons (CFCs) and related compounds used as aerosol propellants, refrigerants, or their substitutes are concerned.

Methane, as the simplest molecule representing this class, has been known for a long time to undergo three body decay in the photodissociation at 121·6 nm, based on the determination of the hydrogen atom quantum yield significantly exceeding the value of 1 [107]. Methane photodissociation has only recently been investigated in a PTS experiment [131]. The two body decay

$$CH_4 + h\nu \rightarrow CH_3 + H \tag{21\,a}$$

has been found to be the dominant process. Whether the three body channel, most likely

$$CH_4 + h\nu \rightarrow CH + H_2 + H \tag{21\,b}$$

is of concerted or sequential nature has not yet been finally determined. The halogenated analogue that has been investigated most intensively using the PTS technique is CF_2I_2 [132, 133]. The three body decay

$$CF_2I_2 + h\nu \rightarrow CF_2 + 2\,I \tag{22}$$

is energetically accessible at the employed dissociation wavelengths in the range from 248 nm to 351 nm. At 351 nm and at 308 nm contributions from two body and sequential three body decay dominate, whereas the synchronous concerted mechanism contributes to a minor degree at 308 nm, becoming the major pathway at 248 nm. However, the applied kinematic model for the concerted decay is limited to synchronous mechanisms for specific geometries, thus neglecting the asynchronous channel. Earlier experiments on the photodissociation of CCl_2F_2 and CCl_3F, monitoring light emission after irradiation with VUV synchrotron radiation, led the authors to propose three body decay to be operative at the high energies necessary to produce electronically excited products, but did not yield data specific enough to determine the nature of the process [134].

A somewhat more complicated system, namely the photodissociation of tetrafluorodiiodoethane

$$C_2F_4I_2 + h\nu \rightarrow C_2F_4 + 2\,I \tag{23}$$

in the wavelength range from 278 nm to 308 nm has been investigated by picosecond time-resolved spectroscopy, monitoring the build-up times for ground and excited spin–orbit state iodine atoms, $I(^2P_{3/2})$ and $I^*(^2P_{1/2})$, respectively [135, 136]. The authors observed a fast build-up (< 1 ps) for I* atoms and a slow but biexponential build-up for ground state I atoms. These results are interpreted as stemming from a sequential decay mechanism, with the first step producing $C_2F_4I + I^*$, the second one producing $C_2F_4 + I$ from C_2F_4I of the first step. The biexponential behaviour is explained by a broad distribution of the internal excitation of the C_2F_4I intermediate and by the dependence of its dissociation rate on its internal excitation.

For a set of halogenated ethanols, in two studies employing sub-Doppler resolved LIF [137] and PTS [138] measurements, the sequential mechanism was found to be exclusively active, according to $XCH_2CH_2OH + h\nu \rightarrow X + C_2H_4 + OH$ (X = Cl, Br, I), with the first bond cleavage producing $X + C_2H_4OH$, and the second producing $C_2H_4 + OH$.

In summary, all possible dissociation pathways have been proposed for different members of the alkane family. Despite the relatively large number of studies, it is not possible at present to obtain a general picture of the nature of their three body decomposition. One of the reasons is the diversity of the applied experimental methods and models used in the data analysis. A more comprehensive approach could help to reveal the influence of different substituents on the three body mechanism.

4.5. *Cluster ions*

Cluster ions that possess bond energies of 1 eV or more, as opposed to neutral van der Waals molecules, can behave more like covalently bound molecules than like loosely bound molecular aggregates. Among the cluster ions that have been studied in photodissociation experiments similar to those for the covalently bound species, multiple fragmentation was observed for Ar_n^+ [73, 139–148], $(CO_2)_3^+$ [149] and $(NO)_3^+$

[150]. Most intensively investigated are the argon systems, however, that have been studied to cluster sizes of up to 40 atoms [148]. It is clear from spectroscopic data [148, 151, 152] as well as from the dissociation studies [140, 142, 148] that up to clusters of 6 atoms Ar_3^+ is the chromophore core determining photophysical and photochemical properties, while the remaining Ar atoms constituting the cluster can be regarded as solvent particles. Therefore, we will constrain ourselves to what is known about the photodissociation of AR_3^+.

The first absorption band of Ar_3^+ is centred around 520 nm and has a large cross-section of $1{\cdot}5 \times 10^{-16}$ cm^2 at the maximum [148, 153]. A second band is observed in the UV near 300 nm [154, 155], which resembles the Ar_2^+ absorption spectrum. The structure of Ar_3^+ is still not precisely known. A number of theoretical investigations [156–165] suggest a linear conformation, although there is disagreement on the issue of symmetry. To our knowledge no experimental evidence has been found in order to support $D_{\infty h}$ or $C_{\infty v}$ symmetry. The dimer ion Ar_2^+ has a relatively high dissociation energy of 10 500 cm^{-1} [166], and the exothermicity for the addition of another argon atom to form Ar_3^+ is still 1700 cm^{-1}, whereas this value drops below 600 cm^{-1} for larger clusters, thus supporting the view of larger Ar_n^+ clusters as being an Ar_3^+ core dissolved in argon [167].

The excitation of Ar_3^+ in the visible part of the spectrum (most commonly applied is the convenient dissociation wavelength of 532 nm [73, 139–142, 147, 148], although various other wavelengths have been employed in the range from 460 nm to 620 nm [143, 145, 146]) leads to the complete fragmentation of the cluster ion:

$$Ar_3^+ + h\nu \rightarrow Ar^+ + Ar + Ar. \tag{24}$$

The first experiments focused on determining the kinetic energy distribution of the Ar^+ ionic fragment after irradiating polarized light onto a mass-selected Ar_3^+-beam [140, 142–148]. All experimental findings agree that there are two types of Ar^+ fragments that are distinguishable (a) by their kinetic energy content and (b) by their spatial distribution. A fast component is observed, showing a preference for being ejected along the polarization vector of the dissociating laser, while a slow component with negligible translational excitation shows no anisotropy at all.

More recent experiments have focused on the detection of the neutral fragments [73, 139–141] containing more information about the dissociation process, since two of them are generated in every event as compared to only one ion. The detection of neutral, atomic argon fragments is made possible by accelerating the parent Ar_3^+ ion beam to energies of several keV and deflecting the ionic fragments after dissociation, but before detection takes place. Thus, only high energy neutral fragments impinge on the particle detector. The kinetic energy distribution of the neutral photofragments is very similar to that of the photoions. Again, there are two components with different behaviour with respect to their kinetic energy content and their spatial distribution: a fast component, aligned preferentially parallel to the polarization vector of the laser, and a slow one, distributed isotropically. In order to explain these experimental data several dissociation models have been invoked that are not always consistent with each other, because the structure of the Ar_3^+ parent is not unambiguously known [139]. None of the proposed models is capable of accounting for all of the experimental results. Thus, competing channels must operate in the dissociation process. Clearly more detailed experimental data are needed to identify the underlying mechanisms.

One important step towards gaining such data is a recently performed experiment by Stace and co-workers [73], which rules out the possibility of more than one fast

fragment being generated in a single event. They employed a variation of the PEPIPICO method in order to observe correlations between the kinetic energy contents of the two neutral photofragments. Their experimental set-up differs from the original PEPIPICO scheme in that (a) the start pulse setting time zero for the TOF measurements of coincidently generated fragments is given by the laser pulse rather than by an ejected photoelectron and (b) the TOF correlation is measured between photoneutrals instead of photoions. In this experiment at least two processes operating in the photodissociation of Ar_3^+ could be identified: one generating two slow, isotropically distributed argon atoms at the same time, the other one generating one fast, anisotropically distributed and one slow, isotropically distributed fragment at a time. For reasons of energy conservation, the generation of two slow neutrals must coincide with the generation of a fast ion, while the generation of one fast and one slow neutral occurs together with the production of a slow ion. The experimental results allow an even deeper understanding from the analysis of the peak contours, which proves the competition between a sequential and a concerted mechanism [4, 5, 40, 73].

To our knowledge, this experiment is the only one so far to exploit coincidence measurements for the near-threshold dissociation of molecular systems induced by outer shell electronic excitation. This experiment bridges the gap between the soft X-ray PEPIPICO experiments described in the following section and the traditional molecular systems which are the subject of this review, therefore opening the door for a much wider application of this technique in molecular reaction dynamics.

At this point a class of experiments in neutral van der Waals complexes should be mentioned that are not usually thought of in terms of three body decays. These studies were developed by Wittig and co-workers in order to study photoinitiated geometry constrained binary reactions in a van der Waals complex consisting of a precursor molecule and a reactant [168]. Upon photodissociating the precursor, one of its photoproducts reacts with the reactant while the second photoproduct is thought to be a spectator. Comparison with the corresponding gas phase experiments showed, however, that it is rather the rule than the exception that the presence of the second photoproduct influences the reaction. Thus, the photodissociation in the van der Waals complex, together with the subsequent bimolecular reaction, can be viewed as a special case of a three body decay. Further references on this topic can be found in a series of recent reviews [169, 170].

4.6. *Molecular ions*

A number of molecular ions have been investigated for which fragmentation into more than two fragments occurs. Most intensively studied have been the dissociation processes of doubly positively charged ions [4–6, 17, 171–174], but three body fragmentation is known to commonly occur for triply positively charged molecular ions [172, 175] as well as for singly negatively charged ions [176–179].

The negative ions HgX_2^- (X = Cl, Br) decay completely into their constituents subsequent to electron attachment to the neutral parent molecules [176, 178]:

$$HgX_2 + e^- \rightarrow HgX_2^- \rightarrow Hg + X + X^- \quad (X = Cl, Br). \tag{25}$$

From the TOF measurement of the ionic fragment the authors identified a fast synchronous concerted decay mechanism to be operative, for the X^- ion carries almost half of the available energy as translational energy with a narrow width of the distribution. Due to the linear geometries of the neutral parent as well as of the ionic fragments the remaining 50% of the available energy must be transferred onto the

neutral X fragment, leaving the central Hg atom almost without any translational energy at all. This result has been obtained by kinematic analysis of the fragment energy and angular distributions and confirmed by classical trajectory calculations. Although not a photoinduced three body decay, it is of greater significance to the photodissociation studies of neutral molecules than the dissociation of doubly charged ions due to the comparable energy range of the applied electron beam inducing the electron attachment.

The study of doubly charged molecular ions includes a wide range of compounds, such as SO_2 [17, 174], OCS [17], CS_2 [17, 173], NO_2 [17], CH_3I [17, 180], SF_6 [17], XCN (X = H, D, CD_3, CF_3, F, Br, I) [5], XNO (X = F, Cl, Br) [171] and XN_3 (X = H, Cl, I) [4] where the photon energies lie in the range between 20 eV and 100 eV, enough to induce double ionization and fragmentation, following inner shell photoionization and Auger cascade:

$$ABC + h\nu \rightarrow ABC^{2+} \rightarrow A + B^+ + C^+. \tag{26}$$

In general, all possible charge distributions in the three body dissociation will occur that are energetically allowed (i.e. $A + B^+ + C^+$, $A^+ + B + C^+$ and $A^+ + B^+ + C$) [5]. Additionally two body channels are open, producing e.g. $AB^+ + C^+$ and the respective permutations.

The earliest model of the CH_3I fragmentation introduced the idea of Coulomb explosion [180], a synchronously acting repulsion of separately charged particles as the result of the ionization process. It turned out that this simple model could not account for some of the peak contours observed in PEPIPICO experiments. Consequently, new more refined models were introduced including the concept of sequential mechanisms [17], some features, the so-called 'twisted peaks', still remained unexplained, and further model refinements were necessary which included the possibility of charge delocalization, where the charge of the molecular ion can be shared by the fragments that are to be born prior to the departure from the interaction region (charge exchange model). For the XN_3 studies [4] this model describes the fragmentation scheme sufficiently well by stating that it can neither be characterized as being purely sequential or purely synchronous. Within the nomenclature of the charge exchange model, it is contributed to by what the authors call concerted, fast sequential, and slow sequential decays with a range of different reaction rates depending on the excitation energy. Within the nomenclature of this review, this would be characterized as an asynchronous concerted mechanism competing with a sequential mechanism where the contribution of the two channels depend on the excitation energy. Especially for low excitation energies, a significant contribution by a (slow) sequential decay channel is observed, which is reduced by increasing the photon energy. Although for each reaction channel of reaction (26), generating chemically distinct fragments, the peak contours can be analysed separately in the PEPIPICO set-up, thus allowing the determination of the reaction mechanism in a manner which is specific to the respective channel, the description of the fragmentation process is complicated due to the large number of competing reaction channels. Energy redistribution prior to fragmentation of the parent ion must take place, since the contribution of the different reaction channels in (26) can be well described by a Boltzmann distribution [5] characterized by a temperature coefficient.

5. A novel approach in kinematic analysis

Faced with the problem of underdetermined kinetic equations in analysing momenta and kinetic energies of three body decay fragments, we will introduce physically meaningful parameters for each type of decay: the sequential mechanism, the synchronous concerted mechanism, and linking these extremes, the asynchronous concerted mechanism. Then, for a given parameter value there exists a well-defined relation between the kinetic fragment properties and the initially excited state of the parent molecule. Consequently, a known distribution of parameter values yields a specific kinetic energy distribution for each fragment. Once these relationships are known, the procedure can be reversed: from experimentally observing kinetic energy distributions, one can fit the experimental data by adjusting parameter distributions for the appropriate decay mechanism(s). This procedure needs not to be unambiguous in general, but it will be when the mechanism is pure, i.e. when no competition between different mechanisms takes place. We are confident however that in most cases, even for competing pathways, an unambiguous assignment is possible. This confidence is based on our work on the photodissociation of phosgene, which is presented in §6, where this very situation has been encountered.

There exist several examples in the literature where for selected mechanisms single values or limited ranges of parameters have been used in the analysis of the three body decays. However, there has not been an attempt to comprehensively characterize the three body decay in general in this way, and therefore we feel it is justified to claim novelty in the following approach.

In this section the parameters for each mechanism are introduced, their role in the energy partitioning is discussed, and the relationships between fragment kinetic energy distributions and parameter distributions are derived.

5.1. *Mechanisms and parameters*

The dividing line between concertedness and sequentiality will be drawn at the mean rotational period, the average time needed for the intermediate fragment to complete a full rotation. Furthermore, our criterion (§1) of unison motion for distinguishing between synchronicity and non-synchronicity is used.

5.1.1. *The synchronous mechanism*

The synchronous three body decay is to be understood as the process where a particle ABC fragments into the three particles A, B and C, with the bonds AB and BC breaking strictly simultaneously. Then the momenta transferred onto the particles A and B must be equal to one another. Satisfying this condition guarantees the identity of the dynamics of the two bond cleavage processes. Moreover, it determines the axis of motion of particle B to equally divide the bond angle α. The bond angle, defined as the angle formed by the three particles A, B and C at the time of fragmentation, is the only parameter quantity necessary to unambiguously describe the synchronous three body decay. The axis defined by the direction of motion of particle B will be denoted the x axis of the coordinate system describing the kinetics of the fragments throughout this section. Correspondingly the y axis designates the direction perpendicular to x within the ABC plane. Figure 1 illustrates the quantities as defined above.

The starting point for the determination of the fragment kinetic energies is the conservation of linear momentum:

$$\mathbf{p}_A + \mathbf{p}_B + \mathbf{p}_C = \mathbf{p}_{ABC} = 0, \tag{27}$$

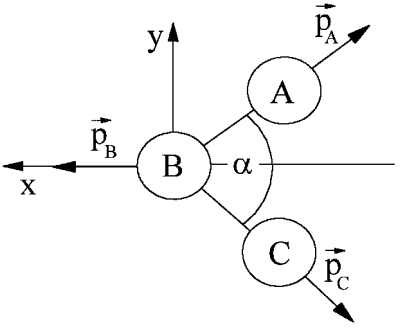

Figure 1. Coordinate system for the description of the synchronous three body decay. The x axis is fixed to the direction of motion of fragment B and as a consequence equally divides the bond angle α.

which can be expressed by

$$\begin{pmatrix} p_{Ax} \\ p_{Ay} \end{pmatrix} + \begin{pmatrix} p_{Bx} \\ 0 \end{pmatrix} + \begin{pmatrix} p_{Cx} \\ p_{Cy} \end{pmatrix} = \begin{pmatrix} 0 \\ 0 \end{pmatrix}. \tag{28}$$

The second criterion for synchronicity, $|\mathbf{p}_A| = |\mathbf{p}_C| = p$, which accounts for the equal division of the bond angle α by the x axis, allows one to rewrite this equation as

$$p \begin{pmatrix} \cos(\alpha/2) \\ \sin(\alpha/2) \end{pmatrix} + p_B \begin{pmatrix} 1 \\ 0 \end{pmatrix} + p \begin{pmatrix} \cos(\alpha/2) \\ -\sin(\alpha/2) \end{pmatrix} = \begin{pmatrix} 0 \\ 0 \end{pmatrix}. \tag{29}$$

Therefore the absolute values for the linear momentum p_B, respectively for the kinetic energy $E_{kin,\,B}$ of particle B, are given by

$$p_B = -2p\cos(\alpha/2) \tag{30}$$

$$E_{kin,\,B} = \frac{p_B^2}{2m_B} = \frac{2p^2}{m_B}\cos^2(\alpha/2). \tag{31}$$

The conservation of energy yields the additional condition that is necessary to express the kinetic energy of particle B and, once this has been done, of the remaining particles A and C as well, using the bond angle α as parameter:

$$E_{kin,\,A} + E_{kin,\,B} + E_{kin,\,C} = \frac{p^2}{2m_A} + \frac{p_B^2}{2m_B} + \frac{p^2}{2m_C} = E_{av} - \sum_{A,\,B,\,C} E_{int} = \varepsilon. \tag{32}$$

E_{kin} denotes the kinetic energies and E_{int} the internal energies of the fragments A, B and C, respectively, the sum of which must be equal to the total available energy E_{av}. In the case of atomic fragments E_{int} equals zero if no electronic excitation is present. For a more general treatment we also include the case where the fragments A, B or C are molecules themselves that possess internal degrees of freedom. If these are not present, then the total kinetic energy ε of all fragments is identical to the available energy E_{av} ($\varepsilon = E_{av}$; $E_{av} = h\nu + E_{int,\,ABC} - D_{diss}(\text{A–B–C})$).

The conservation of energy yields for p:

$$p = [2\mu_{AC}(\varepsilon - E_{kin,\,B})]^{1/2}, \tag{33}$$

where $\mu_{AC} = m_A m_C/(m_A+m_C)$ is the reduced mass of the particles A and C, and for $E_{kin,\,B}$:

$$E_{kin,\,B} = \frac{\varepsilon}{1+(m_B/4\mu_{AC})\,[1+\tan^2(\alpha/2)]}. \tag{34}$$

Once the kinetic energy of particle B is known, the kinetic energies of the partner fragments A and C can be calculated to be

$$E_{kin,\,C} = \frac{\varepsilon}{4(m_C/m_B)\cos^2(\alpha/2)+[(m_A+m_C)/m_A]}$$

$$E_{kin,\,A} = \frac{\varepsilon}{4(m_A/m_B)\cos^2(\alpha/2)+[(m_A+m_C)/m_C]}. \tag{35}$$

As illustrative limiting cases we will discuss a linear molecule ($\alpha = 180°$) and a symmetric molecule ($m_A = m_C$). For the linear molecule the central particle B will stay at rest, while the kinetic energies for the particles A and C are given by the inverse ratio of their masses:

$$E_{kin,\,B} = 0, \quad E_{kin,\,A} = \varepsilon\frac{m_C}{m_A+m_C}, \quad E_{kin,\,C} = \varepsilon\frac{m_A}{m_A+m_C}. \tag{36}$$

For equal masses of A and C ($m_A = m_C = m$), i.e. for a symmetric molecule ABA, the kinetic energies for arbitrary values of the bond angle α are

$$E_{kin,\,B} = \frac{\varepsilon}{1+\{m_B/[2m\cos^2(\alpha/2)]\}} \tag{37a}$$

$$E_{kin,\,A} = E_{kin,\,C} = \frac{1}{2}\frac{\varepsilon}{1+2(m/m_B)\cos^2(\alpha/2)}. \tag{37b}$$

For a linear symmetric molecule one gets analogously to equation (36):

$$E_{kin,\,B} = 0, \quad E_{kin,\,A} = E_{kin,\,C} = \varepsilon/2. \tag{38}$$

The case of equal masses with $\alpha = 0°$ describes the two body decay of the particle ABA into a particle B and molecule A_2, if the additional bond energy of the A_2 molecule is added to the total kinetic energy ε. Note that this is not true for different masses of A and C, since in this case the speeds of A and C would be different due to the equality of their momenta.

The case of synchronous decay of a linear symmetric molecule has been observed for the dissociative electron attachment to $HgCl_2$ [177], whereas the 'degenerate' two body decay of a symmetric molecule—sometimes termed the molecular channel—has been found to occur in addition to three body channels e.g. for formaldehyde (H_2CO) [181, 182], thionyl chloride ($SOCl_2$) [110–113] and thiophosgene ($CSCl_2$) [183]. We will also consider the possible existence of the molecular channel in the photodissociation of phosgene [184].

5.1.2. *The sequential mechanism*

The description of the sequential mechanism is divided into two parts. First, the two decay steps are treated as two independent two body decays. Second, a transformation of the centre of mass coordinates of the second step into the laboratory

coordinates has to be performed. The description starts off as before: the particle ABC is assumed to be at rest prior to its decay and carries the energy E_{av} exceeding the dissociation energy into the three final products A, B and C, so that the initial conditions are given, as before, by equation (27).

From the conservation of energy and momentum the following relations hold between the fragments of the first dissociation step:

$$E_{av} = E_{int,\,AB} + E_{kin,\,AB} + E_{int,\,C} + E_{kin,\,C} \tag{39}$$

$$|p_C| = m_C|v_C| = m_{AB}|v_{AB}| = |p_{AB}| \tag{40}$$

from which one can calculate the kinetic energies of the primary fragments:

$$E_{kin,\,C} = \frac{m_{AB}}{m_C}E_{kin,\,AB} = \frac{m_{AB}}{m_{ABC}}(E_{av} - E_{int,\,AB} - E_{int,\,C}) \tag{41a}$$

$$E_{kin,\,AB} = \frac{m_C}{m_{AB}}E_{kin,\,C} = \frac{m_C}{m_{ABC}}(E_{av} - E_{int,\,AB} - E_{int,\,C}) \tag{41b}$$

While $E_{int,\,C}$, the internal energy of the final fragment C, is an observable quantity, the energy deposition $E_{AB} = E_{int,\,AB}$, the internal energy temporarily deposited in the intermediate particle AB, cannot be observed experimentally. However, it governs the distribution of the kinetic energy of the final fragment C as well as influencing the distributions of the kinetic energies for the final fragments A and B, as explained below. In this context the energy deposition E_{AB} is defined as that portion of the internal energy of AB that exceeds the dissociation energy of AB. This is consistent with the definition of the available energy E_{av} with respect to the three final products A, B and C in their respective ground states.

The situation prior to the second decay step is more complicated than for the first step, since the momentum p_{AB} of the AB centre of mass, resulting from the first dissociation step, has to be taken into account.

Initially we treat the second step analogously to the first step, however, i.e. in the centre of mass coordinate system of the intermediate particle, indicated by the superscript 'CM'. Where necessary, laboratory quantities will be marked by the superscript 'LAB'. With this convention, the situation prior to the first bond cleavage is described by:

$$p_{AB}^{CM} = 0 \quad E_{AB}^{CM} = E_{AB}. \tag{42}$$

Correspondingly equations (39) and (40) can be written as

$$E_{kin,\,A}^{CM} + E_{kin,\,B}^{CM} + E_{int,\,A} + E_{int,\,B} = E_{AB} \tag{43}$$

$$|p_A^{CM}| = |p_B^{CM}|. \tag{44}$$

The internal energies $E_{int,\,A}$ and $E_{int,\,B}$ of the fragments A and B are independent of the coordinate system and, thus, do not require the superscript CM. In order to transform the centre of mass quantities into the laboratory system, where measurements are performed, one needs to introduce the decay angle θ, serving as a parameter. This angle is identical to the angle θ from §3.1, i.e. the angle of the direction of motion of the AB centre of mass in the laboratory with the direction of motion of the final fragment in the centre of mass coordinate system of AB. The relevant quantities are illustrated in figure 2, where θ is—arbitrarily—defined for fragment A.

Prior to the transformation of the centre of mass into the laboratory coordinates

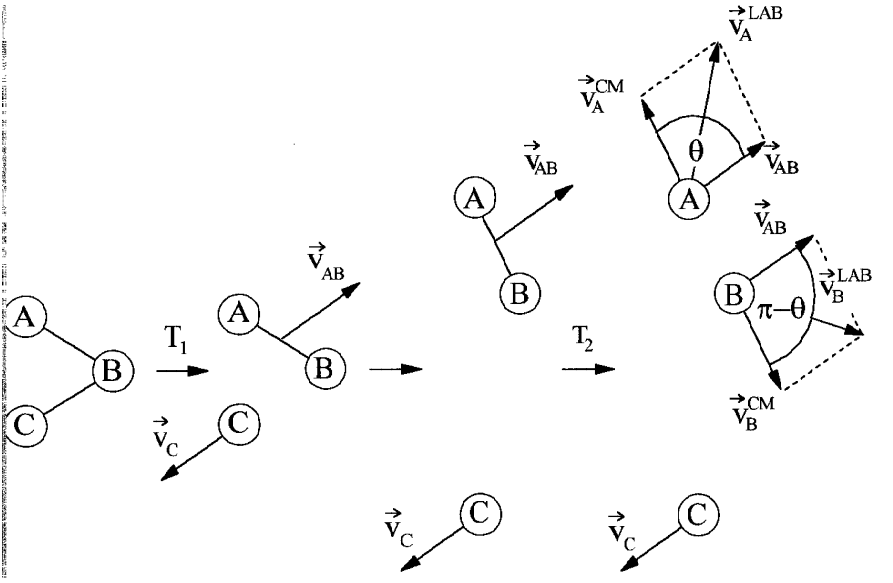

Figure 2. Illustration of the quantities used for the description of the sequential decay mechanism. $\mathbf{v}_{AB}^{LAB}$ is the velocity of the intermediate AB particle in the laboratory system, $\mathbf{v}_{A}^{CM}$ and $\mathbf{v}_{B}^{CM}$ are the velocities of the final fragments A and B in the centre of mass system of the intermediate AB, while $\mathbf{v}_{A}^{LAB}$ and $\mathbf{v}_{B}^{LAB}$ are the observable laboratory velocities of the fragments A and B. θ is the decay angle of the direction of motion of the intermediate AB with the centre of mass velocity $\mathbf{v}_{A}^{CM}$ of particle A.

one has to derive the connecting relations between them. It is obvious that the laboratory velocities of the fragments A and B are given by the vector addition of the centre of mass velocity $\mathbf{v}_{AB}^{LAB}$ of AB in the laboratory and the fragment velocities $\mathbf{v}_{A}^{CM}$ resp. $\mathbf{v}_{B}^{CM}$ in the centre of mass system of AB:

$$\begin{aligned} \mathbf{v}_{A}^{LAB} &= \mathbf{v}_{AB}^{LAB} + \mathbf{v}_{A}^{CM} \\ \mathbf{v}_{B}^{LAB} &= \mathbf{v}_{AB}^{LAB} + \mathbf{v}_{A}^{CM}. \end{aligned} \tag{45}$$

The limiting values for the laboratory velocities $\mathbf{v}_{A}^{LAB}$ and $\mathbf{v}_{B}^{LAB}$ are thus given by the triangular relation as the sum and the difference of the respective velocities:

$$\begin{aligned} \left|v_{AB}^{LAB} - v_{A}^{CM}\right| \leqslant v_{A}^{LAB} \leqslant \left|v_{AB}^{LAB} + v_{A}^{CM}\right| \\ \left|v_{AB}^{LAB} - v_{B}^{CM}\right| \leqslant v_{B}^{LAB} \leqslant \left|v_{AB}^{LAB} + v_{B}^{CM}\right|. \end{aligned} \tag{46}$$

Subsequently the fragment laboratory velocities are calculated quantitatively. According to figure 2 the angle of $\mathbf{v}_{A}^{CM}$ with $\mathbf{v}_{AB}^{LAB}$ is equal to θ, and the angle of $\mathbf{v}_{B}^{CM}$ with $\mathbf{v}_{AB}^{LAB}$ is equal to $\pi - \theta$, so that the absolute values of the respective velocities are determined by

$$v_{A}^{LAB\,2} = v_{AB}^{LAB\,2} + v_{A}^{CM\,2} + 2v_{AB}^{LAB}\, v_{A}^{CM} \cos\theta \tag{47a}$$

$$v_{B}^{LAB\,2} = v_{AB}^{LAB\,2} + v_{B}^{CM\,2} - 2v_{AB}^{LAB}\, v_{B}^{CM} \cos\theta. \tag{47b}$$

Using these equations, all fragment laboratory velocities can be calculated, provided the available energy E_{av}, the decay angle θ and the energy deposition E_{AB} in the intermediate are known.

From now on we will restrict ourselves to looking at fragment A only. The procedure for fragment B is analogous to the one presented below for fragment A, and

Table 3. Synchronous mechanism: relationships between the fragment kinetic energies $E_{\mathrm{kin}A,\,B,\,C}$ and the bond angle α and between the corresponding distributions.

Parameter	$\alpha_0, \Delta\alpha$
$f_\alpha(\alpha)$	$f_\alpha(\alpha) \approx \exp\left[-\frac{(\alpha-\alpha_0)^2}{2\Delta\alpha^2}\right]$
$E_{\mathrm{kin},\,A}$	$E_{\mathrm{kin},\,A} = \frac{\varepsilon}{4(m_A/m_B)\cos^2(\alpha/2)+[(m_A+m_C)/m_C]}$
$E_{\mathrm{kin},\,B}$	$E_{\mathrm{kin},\,B} = \frac{\varepsilon}{1+(m_B/4\mu_{AC}\cos^2(\alpha/2))} = \frac{\varepsilon}{1+(m_B/4\mu_{AC})[1+\tan^2(\alpha/2)]}$
$E_{\mathrm{kin},\,C}$	$E_{\mathrm{kin},\,C} = \frac{\varepsilon}{4(m_C/m_B)\cos^2(\alpha/2)+[(m_A+m_C/m_A]}$
$\alpha(E_{\mathrm{kin},\,A})$	$\alpha(E_{\mathrm{kin},\,A}) = 2\arccos\left[\frac{m_B}{4m_A}\left(\frac{\varepsilon}{E_{\mathrm{kin},\,A}}-\frac{m_A+m_C}{m_C}\right)\right]^{1/2}$
$\alpha(E_{\mathrm{kin},\,B})$	$\alpha(E_{\mathrm{kin},\,B}) = 2\arctan\left[\frac{4\mu_{AC}}{m_B}\left(\frac{\varepsilon}{E_{\mathrm{kin},\,B}}-1\right)-1\right]^{1/2} = 2\arccos\left[\frac{m_B}{4\mu_{AC}}\left(\frac{E_{\mathrm{kin},\,B}}{\varepsilon-E_{\mathrm{kin},\,B}}\right)\right]^{1/2}$
$\alpha(E_{\mathrm{kin},\,C})$	$\alpha(E_{\mathrm{kin},\,C}) = 2\arccos\left[\frac{m_B}{4m_C}\left(\frac{\varepsilon}{E_{\mathrm{kin},\,C}}-\frac{m_A+m_C}{m_A}\right)\right]^{1/2}$
$f_E(E_{\mathrm{kin},\,A})$	$f_E^{\mathrm{syn}}(E_{\mathrm{kin},\,A}) = \frac{\varepsilon}{E_{\mathrm{kin},\,A}^2} f_\alpha[\alpha(E_{\mathrm{kin},\,A})] \Big/ \left\{\left[\frac{4m_A}{m_B}-\left(\frac{\varepsilon}{E_{\mathrm{kin},\,A}}-\frac{m_A+m_C}{m_C}\right)\right] \times \left(\frac{\varepsilon}{E_{\mathrm{kin},\,A}}-\frac{m_A+m_C}{m_C}\right)\right\}^{1/2}$
$f_E(E_{\mathrm{kin},\,B})$	$f_E^{\mathrm{syn}}(E_{\mathrm{kin},\,B}) = \frac{\varepsilon}{E_{\mathrm{kin},\,B}(\varepsilon-E_{\mathrm{kin},\,B})} f_\alpha[\alpha(E_{\mathrm{kin},\,B})] \Big/ \left[\frac{4\mu_{AC}}{m_B}\left(\frac{\varepsilon}{E_{\mathrm{kin},\,B}}-1\right)-1\right]^{1/2}$
$f_E(E_{\mathrm{kin},\,C})$	$f_E^{\mathrm{syn}}(E_{\mathrm{kin},\,C}) = \frac{\varepsilon}{E_{\mathrm{kin},\,C}^2} f_\alpha[\alpha(E_{\mathrm{kin},\,C})] \Big/ \left\{\left[\frac{4m_C}{m_B}-\left(\frac{\varepsilon}{E_{\mathrm{kin},\,C}}-\frac{m_A+m_C}{m_A}\right)\right] \times \left(\frac{\varepsilon}{E_{\mathrm{kin},\,C}}-\frac{m_A+m_C}{m_A}\right)\right\}^{1/2}$

no new information can be gained from fragment B. The results for B are presented at the end of this section in tables 3–5. Quantities not marked by a superscript are referenced to the laboratory coordinate system.

The aim of the subsequent considerations is to determine the influence of the two parameters θ and E_{AB} on the kinetic energy of the final fragments, in other words to derive the relationship $E_{\mathrm{kin}}(\theta, E_{AB})$.

One obtains for the kinetic energies of the fragments in the centre of mass system of AB:

$$E_{\mathrm{kin},\,A}^{\mathrm{CM}} = \frac{m_B}{m_A} E_{\mathrm{kin},\,B}^{\mathrm{CM}}, \tag{48}$$

and the corresponding centre of mass velocity:

$$v_A^{\mathrm{CM}} = \left(\frac{2E_{\mathrm{kin},\,A}^{\mathrm{CM}}}{m_A}\right)^{1/2} = \left[\frac{2m_B}{m_A m_{AB}}(E_{AB} - E_{\mathrm{int},\,A} - E_{\mathrm{int},\,B})\right]^{1/2}. \tag{49}$$

Table 4. Sequential mechanism: relationships between the fragment kinetic energies $E_{\mathrm{kin}A,\,B,\,C}$, the decay angle θ and the energy deposition E_{AB} and between the corresponding distributions.

Parameter	$E_{AB,\,0}$, ΔE_{AB}
$f_\theta(\theta)$	$f_\theta(\theta) = \text{const.} = c_\theta$
$f_{AB}(E_{AB})$	$f_{AB}(E_{AB}) \approx \exp\left[-\dfrac{(E_{AB}-E_{AB,\,0})^2}{2\Delta E_{AB}^2}\right]$
$E_{\mathrm{kin},\,A}$	$E_{\mathrm{kin},\,A} = p_0(E_{\mathrm{int}}) + M_{AB}\,E_{AB} + M_\theta \cos\theta[p_2(E_{\mathrm{int}}) + p_1(E_{\mathrm{int}})\,E_{AB} - E_{AB}^2]^{1/2}$
$E_{\mathrm{kin},\,A}$	$E_{\mathrm{kin},\,A} = p_0'(E_{\mathrm{int}}) + M'_{AB}\,E_{AB} + M'_\theta \cos\theta[p_2(E_{\mathrm{int}}) + p_1(E_{\mathrm{int}})\,E_{AB} - E_{AB}^2]^{1/2}$
$E_{\mathrm{kin},\,C}$	$E_{\mathrm{kin},\,C} = \dfrac{m_{AB}}{m_C}E_{\mathrm{kin},\,AB} = \dfrac{m_{AB}}{m_{ABC}}(E_{av} - E_{AB} - E_{\mathrm{int},\,C})$
$f_E(E_{\mathrm{kin},\,A})$	$f_E^{\mathrm{seq}}(E_{\mathrm{kin},\,A}) = \displaystyle\int_{a(E_{\mathrm{kin},\,A})-[a(E_{\mathrm{kin},\,A})^2+b(E_{\mathrm{kin},\,A})]^{1/2}}^{a(E_{\mathrm{kin},\,A})+[a(E_{\mathrm{kin},\,A})^2+b(E_{\mathrm{kin},\,A})]^{1/2}} \mathrm{d}E_{AB} \times\left\{\dfrac{f_{AB}(E_{AB})\,c_\theta}{[-E_{AB}^2 + 2a(E_{\mathrm{kin},\,A})\,E_{AB} + b(E_{\mathrm{kin},\,A})]^{1/2}}\right\}$
$f_E(E_{\mathrm{kin},\,A})$	$f_E^{\mathrm{seq}}(E_{\mathrm{kin},\,B}) = \displaystyle\int_{a'(E_{\mathrm{kin},\,B})-[a'(E_{\mathrm{kin},\,B})^2+b'(E_{\mathrm{kin},\,B})]^{1/2}}^{a'(E_{\mathrm{kin},\,B})+[a'(E_{\mathrm{kin},\,B})^2+b'(E_{\mathrm{kin},\,B})]^{1/2}} \mathrm{d}E_{AB} \times\left\{\dfrac{f_{AB}(E_{AB})\,c_\theta}{[-E_{AB}^2 + 2a'(E_{\mathrm{kin},\,B})\,E_{AB} + b'(E_{\mathrm{kin},\,B})]^{1/2}}\right\}$
$f_E(E_{\mathrm{kin},\,C})$	$f_E^{\mathrm{seq}}(E_{\mathrm{kin},\,C}) = f_{AB}[E_{AB}(E_{\mathrm{kin},\,C})]\dfrac{m_{AB}}{m_{ABC}}$

Analogously the laboratory velocity of the AB centre of mass is given by

$$v_{AB} = \left(\frac{2E_{\mathrm{kin},\,AB}}{m_{AB}}\right)^{1/2} = \left[\frac{2m_C}{m_{ABC}\,m_{AB}}(E_{av} - E_{AB} - E_{\mathrm{int},\,C})\right]^{1/2}. \tag{50}$$

Inserting equations (49) and (50) into equation (47*a*) shows that the laboratory velocity of fragment A can be calculated from the following expression:

$$v_A^2 = \frac{2m_B}{m_A\,m_{AB}}(E_{AB} - E_{\mathrm{int}A} - E_{\mathrm{int}B}) + 2\frac{m_C}{m_{AB}\,m_{ABC}}(\varepsilon - E_{AB} - E_{\mathrm{int}C}) + \frac{4}{m_{AB}}\left(\frac{m_B\,m_C}{m_A\,m_{ABC}}\right)^{1/2}\cos\alpha[(\varepsilon - E_{AB} - E_{\mathrm{int}C})\,(E_{AB} - E_{\mathrm{int}A} - E_{\mathrm{int}B})]^{1/2}. \tag{51}$$

The dependence of the fragment kinetic energy on the energy deposition and the decay angle can be expressed by

$$E_{\mathrm{kin},\,A}(E_{AB},\theta) = p_0(E_{\mathrm{int}}) + M_{AB}\,E_{AB} + M_\theta\cos\theta[p_2(E_{\mathrm{int}}) + p_1(E_{\mathrm{int}})E_{AB} - E_{AB}^2]^{1/2}, \tag{52}$$

where the following abbreviations have been used in order to clarify the parameter contributions:

Table 5. Asynchronous concerted mechanism: relationships between the values of the fragment kinetic energies $E_{\mathrm{kin}A,\ B,\ C}$, the decay angle θ and the energy deposition E_{AB} and between the corresponding distributions.

Parameter	$\theta_0, \Delta\theta, E_{\mathrm{AB},\ 0}\ \Delta E_{\mathrm{AB}}$
$f_\theta(\theta)$	$f_\theta[\theta(E_{\mathrm{kin}}, E_{\mathrm{AB}})] \approx \exp\left[-\frac{(\theta(E_{\mathrm{kin}}, E_{\mathrm{AB}}) - \beta\theta_0)^2}{2\Delta\theta^2}\right]$
$f_{\mathrm{AB}}(E_{\mathrm{AB}})$	$f_{\mathrm{AB}}(E_{\mathrm{AB}}) \approx \exp\left[-\frac{(E_{\mathrm{AB}} - E_{\mathrm{AB},\ 0})^2}{2\Delta E_{\mathrm{AB}}^2}\right]$
$E_{\mathrm{kin},\ \mathrm{A}}$	$E_{\mathrm{kin},\ \mathrm{A}} = p_0(E_{\mathrm{int}}) + M_{\mathrm{AB}}\, E_{\mathrm{AB}} + M_\theta \cos\theta[p_2(E_{\mathrm{int}}) + p_1(E_{\mathrm{int}})\, E_{\mathrm{AB}} - E_{\mathrm{AB}}^2]^{1/2}$
$E_{\mathrm{kin},\ \mathrm{B}}$	$E_{\mathrm{kin},\ \mathrm{B}} = p_0'(E_{\mathrm{int}}) + M'_{\mathrm{AB}}\, E_{\mathrm{AB}} + M'_\theta \cos\theta[p_2(E_{\mathrm{int}}) + p_1(E_{\mathrm{int}})\, E_{\mathrm{AB}} - E_{\mathrm{AB}}^2]^{1/2}$
$E_{\mathrm{kin},\ \mathrm{C}}$	$E_{\mathrm{kin},\ \mathrm{C}} = \frac{m_{\mathrm{AB}}}{m_{\mathrm{C}}} E_{\mathrm{kin},\ \mathrm{AB}} = \frac{m_{\mathrm{AB}}}{m_{\mathrm{ABC}}}(E_{\mathrm{av}} - E_{\mathrm{AB}} - E_{\mathrm{int},\ \mathrm{C}})$
$\theta(E_{\mathrm{kin},\ \mathrm{A}})$	$\theta(E_{\mathrm{AB}}, E_{\mathrm{kin},\ \mathrm{A}}) = \arccos\left\{\frac{E_{\mathrm{kin},\ \mathrm{A}} - p_0(E_{\mathrm{int}}) - M_{\mathrm{AB}}\, E_{\mathrm{AB}}}{M_\theta[p_2(E_{\mathrm{int}}) + p_1(E_{\mathrm{int}})\, E_{\mathrm{AB}} - E_{\mathrm{AB}}^2]^{1/2}}\right\}$
$\theta(E_{\mathrm{kin},\ \mathrm{B}})$	$\theta(E_{\mathrm{AB}}, E_{\mathrm{kin},\ \mathrm{B}}) = \arccos\left\{\frac{E_{\mathrm{kin},\ \mathrm{B}} - p_0'(E_{\mathrm{int}}) - M'_{\mathrm{AB}}\, E_{\mathrm{AB}}}{M'_\theta[p_2(E_{\mathrm{int}}) + p_1(E_{\mathrm{int}})\, E_{\mathrm{AB}} - E_{\mathrm{AB}}^2]^{1/2}}\right\}$
$f_{\mathrm{E}}(E_{\mathrm{kin},\ \mathrm{A}})$	$f_{\mathrm{E}}^{\mathrm{conc}}(E_{\mathrm{kin},\ \mathrm{A}}) = \int_{a(E_{\mathrm{kin},\ \mathrm{A}}) - [\,a(E_{\mathrm{kin},\ \mathrm{A}})^2 + b(E_{\mathrm{kin},\ \mathrm{A}})]^{1/2}}^{a(E_{\mathrm{kin},\ \mathrm{A}}) + [\,a(E_{\mathrm{kin},\ \mathrm{A}})^2 + b(E_{\mathrm{kin},\ \mathrm{A}})]^{1/2}} \mathrm{d}E_{\mathrm{AB}} \times \left\{\frac{f_{\mathrm{AB}}(E_{\mathrm{AB}}) f_\theta[\theta(E_{\mathrm{kin},\ \mathrm{A}}, E_{\mathrm{AB}})]}{[-E_{\mathrm{AB}}^2 + 2a(E_{\mathrm{kin},\ \mathrm{A}})\, E_{\mathrm{AB}} + b(E_{\mathrm{kin},\ \mathrm{A}})]^{1/2}}\right\}$
$f_{\mathrm{E}}(E_{\mathrm{kin},\ \mathrm{B}})$	$f_{\mathrm{E}}^{\mathrm{conc}}(E_{\mathrm{kin},\ \mathrm{B}}) = \int_{a'(E_{\mathrm{kin},\ \mathrm{B}}) - [\,a'(E_{\mathrm{kin},\ \mathrm{B}})^2 + b'(E_{\mathrm{kin},\ \mathrm{B}})]^{1/2}}^{a'(E_{\mathrm{kin},\ \mathrm{B}}) + [\,a'(E_{\mathrm{kin},\ \mathrm{B}})^2 + b'(E_{\mathrm{kin},\ \mathrm{B}})]^{1/2}} \mathrm{d}E_{\mathrm{AB}} \times \left\{\frac{f_{\mathrm{AB}}(E_{\mathrm{AB}}) f_\theta[\theta(E_{\mathrm{kin},\ \mathrm{B}}, E_{\mathrm{AB}})]}{[-E_{\mathrm{AB}}^2 + 2a'(E_{\mathrm{kin},\ \mathrm{B}})\, E_{\mathrm{AB}} + b'(E_{\mathrm{kin},\ \mathrm{B}})]^{1/2}}\right\}$
$f_{\mathrm{E}}(E_{\mathrm{kin},\ \mathrm{C}})$	$f_{\mathrm{E}}^{\mathrm{conc}}(E_{\mathrm{kin},\ \mathrm{C}}) = f_{\mathrm{AB}}[E_{\mathrm{AB}}(E_{\mathrm{kin},\ \mathrm{C}})]\frac{m_{\mathrm{AB}}}{m_{\mathrm{ABC}}}$

$$p_0(E_{\mathrm{int}}) = \frac{m_{\mathrm{A}} m_{\mathrm{C}}}{m_{\mathrm{AB}}\, m_{\mathrm{ABC}}}(E_{\mathrm{av}} - E_{\mathrm{int},\ \mathrm{C}}) - \frac{m_{\mathrm{B}}}{m_{\mathrm{AB}}}(E_{\mathrm{int},\ \mathrm{A}} + E_{\mathrm{int},\ \mathrm{B}}) \tag{53a}$$

$$p_1(E_{\mathrm{int}}) = E_{\mathrm{av}} - E_{\mathrm{int},\ \mathrm{C}} + E_{\mathrm{int},\ \mathrm{A}} + E_{\mathrm{int},\ \mathrm{B}} \tag{53b}$$

$$p_2(E_{\mathrm{int}}) = (E_{\mathrm{int},\ \mathrm{A}} + E_{\mathrm{int},\ \mathrm{B}})(E_{\mathrm{int},\ \mathrm{C}} - E_{\mathrm{av}}) \tag{53c}$$

$$M_{\mathrm{AB}} = \frac{m_{\mathrm{B}}}{m_{\mathrm{AB}}} - \frac{m_{\mathrm{A}} m_{\mathrm{C}}}{m_{\mathrm{AB}}\, m_{\mathrm{ABC}}} \tag{53d}$$

$$M_\theta = 2\left(\frac{m_{\mathrm{A}} m_{\mathrm{B}} m_{\mathrm{C}}}{m_{\mathrm{AB}}^2\, m_{\mathrm{ABC}}}\right)^{1/2}. \tag{53e}$$

The contributions of the quantities $E_{\mathrm{int},\ \mathrm{A}}$, $E_{\mathrm{int},\ \mathrm{B}}$ and $E_{\mathrm{int},\ \mathrm{C}}$ that are accessible to experimental observations are combined in the coefficients p_0, p_1 and p_2, whereas the dependence on the parameter values is given explicitly. p_0 contains the kinetic energy that would be transferred onto fragment A, if there were no energy deposited in the

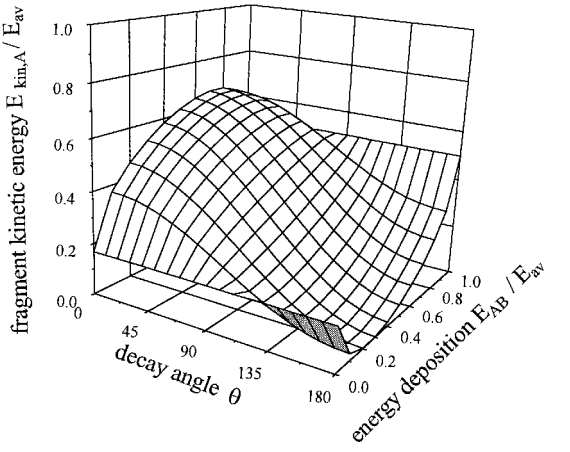

Figure 3. Kinetic energy hypersurface $E_{\mathrm{kin,\,A}}(\theta, E_{\mathrm{AB}})$ illustrating the dependence of the kinetic energy of fragment A on the parameter values θ and E_{AB}.

intermediate AB at all. p_1 is the total kinetic energy of all fragments and is reduced to the available energy E_{av} without internal excitation of any one of the fragments, whereas p_2 is only different from zero if at least one of the final fragments A and B is internally excited.

For the fragment B one obtains a formally identical equation by consequently exchanging the masses m_{A} and m_{B}, where the coefficients p_0, M_{AB} and M_θ have to be replaced by the correspondingly redefined constants p_0', M'_{AB} and M'_θ.

One should pause here to become familiar with the function $E_{\mathrm{kin,\,A}}(\theta, E_{\mathrm{AB}})$, which depends on the two variables θ and E_{AB} as described by equation (52). The parameter ranges are $0 \leqslant E_{\mathrm{AB}} \leqslant E_{\mathrm{av}}$ and $0 \leqslant \theta \leqslant \pi$, respectively. An illustration of the energy surface defined by $E_{\mathrm{kin,\,A}}(E_{\mathrm{AB}}, \theta)$ is given in figure 3. The upper limit for the energy deposition E_{AB} is reached when all available energy is deposited into the intermediate. In this case the two particles AB and C would rest next to each other with AB being highly internally excited—not a very probable scenario, but useful for imagining the limiting case. The lower limit for E_{AB} is characterized by exclusively partitioning the energy in the translational degrees of freedom. The restriction of θ to values equal to or smaller than π originates from the symmetry of the process for a reflection at a plane containing the axis of motion of the intermediate. In other words, the energy transfer onto a fragment does not depend on whether it rotates clockwise or counter-clockwise, but only on the absolute value of the decay angle. A decay angle $\theta = 0$ describes complete forward scattering, where fragment and centre of mass velocities have the same directions, whereas $\theta = \pi$ describes complete backward scattering, where fragment and centre of mass velocities have opposite directions.

The function $E_{\mathrm{kin,\,A}}(\theta)$ is monotonic with respect to the decay angle θ, i.e. the kinetic energy of the fragment continually decreases when changing the decay angle from forward to backward scattering. Consequently, the maximum kinetic energy will be found of forward scattering, and the minimum kinetic energy for backward scattering, which is, of course, what is expected. The dependence on the second parameter, the energy deposition E_{AB}, does not show a monotonic behaviour, however. The same kinetic energy can be induced in fragment A, even for identical decay angles, by different values of the energy deposition in the intermediate.

For minimum and maximum energy deposition the transfer of kinetic energy in the

fragment is constant, i.e. independent of the decay angle, as is the case for a two body decay. Indeed, these two cases are the borderlines between three body and two body decay, since there is no momentum transfer onto the products, either in the first step, if $E_{AB} = E_{av}$, or in the second step, if $E_{AB} = 0$. Thus, the respective fragments will not separate from each other, and the decay angle is not well-defined. Any other value for the energy deposition produces a more or less broad range of fragment kinetic energies, that can be accessed via different decay angles.

Although it is not immediately necessary for discussing the kinetic energy distributions, we want to point out that the maximum and the minimum kinetic energies that can be transferred in the fragments by a sequential decay mechanism will not be realized by one of the limiting values of the energy deposition, but by some intermediate value, which depends on the masses and internal energies of the final fragments. This behaviour is a consequence of the above-mentioned non-monotonic dependence of the fragment kinetic energy on the energy deposition E_{AB}. In the case of forward scattering ($\theta < \pi/2$) the fragment kinetic energy increases with increasing energy deposition E_{AB}, until it reaches a maximum (figure 3). If the energy deposition is further increased, the fragment kinetic energy starts decreasing. The analogous behaviour is found for backward scattering ($\theta > \pi/2$): the minimum of the kinetic energy is not realized for $E_{AB} = 0$, but for some value in between 0 and E_{av}, and a further decrease in the energy deposition occurs together with an increase in the fragment kinetic energy. Only for the decay angle $\theta = \pi/2$ is there a strictly positive correlation between the energy deposition in the intermediate and the fragment kinetic energy.

The energy depositions E_{AB}^{max} resp. E_{AB}^{min} that induce maximum and minimum kinetic energies in the fragment are given by

$$E_{AB}^{max}(\theta, E_{int}) = \frac{p_+}{2}\left[1 + M_{AB}\left(\frac{1 + 4p_2/p_1^2}{M_{AB}^2 + M_\theta^2 \cos^2\theta}\right)^{1/2}\right] \quad \text{for } 0 \leqslant \theta \leqslant \pi/2 \qquad (54a)$$

$$E_{AB}^{max}(\theta, E_{int}) = p_1 \quad \text{for } \pi/2 \leqslant \theta \leqslant \pi \qquad (54b)$$

$$E_{AB}^{min}(\theta, E_{int}) = 0 \quad \text{for } 0 \leqslant \theta \leqslant \pi/2 \qquad (54c)$$

$$E_{AB}^{min}(\theta, E_{int}) = \frac{p_+}{2}\left[1 - M_{AB}\left(\frac{1 + 4p_2/p_1^2}{M_{AB}^2 + M_\theta^2 \cos^2\theta}\right)^{1/2}\right] \quad \text{for } \pi/2 \leqslant \theta \leqslant \pi. \qquad (54d)$$

In the case of atomic fragments, where no internal fragment excitation is possible, for a given value of the decay angle θ the energy depositions E_{AB}^{max} and E_{AB}^{min} are given by

$$E_{AB}^{max/min}(\theta) = \frac{E_{av}}{2}\left[1 \pm \left(\frac{M_{AB}^2}{M_\theta^2 \cos^2\theta + M_{AB}^2}\right)^{1/2}\right] \qquad (55)$$

This expression tends to E_{av} and to 0, respectively, if M_θ is small compared to M_{AB}, which is always the case if at least one of the fragments is light compared to the other fragments. This will be important for the sequential decay of hydrogen-containing compounds. However, the mathematical description then resembles the two body decay concept, for in the dissociation step, in which the hydrogen atom separates from the precursor, it will take along almost all kinetic energy, and the partner can to a fair approximation thought to be at rest.

It is easily seen from equation (55) that for $\theta = \pi/2$ the function $E_{\mathrm{kin,\,A}}(E_{\mathrm{AB}})$ does not possess minima or maxima, but monotonically depends on E_{AB}.

According to the considerations presented above, the absolute maximum and the absolute minimum of the fragment kinetic energy are realized for forward and backward scattering, i.e. for $\theta = 0$ and $\theta = \pi$, where $\cos\theta = 1$:

$$E_{\mathrm{AB}}^{\mathrm{max/min}}\ (\theta = 0, \pi) = \frac{E_{\mathrm{av}}}{2}\left[1 \pm \left(\frac{M_{\mathrm{AB}}^2}{M_\vartheta^2 + M_{\mathrm{AB}}^2}\right)^{1/2}\right]. \tag{56}$$

5.1.3. *The asynchronous mechanism*

The asynchronous concerted three body decay links the cases of the synchronous and the sequential decays discussed above. One would expect therefore that describing the asynchronous concerted mechanism would be most easily performed by correspondingly modifying the synchronous model. Although the two concerted mechanisms are close to each other in one's imagination, it is more appropriate to adapt the sequential model and perform necessary alterations. The formalism for describing the synchronous mechanism is not suitable because it explicitly makes use of the equality of momentum transfer onto the fragments A and C, a condition that is in general not satisfied for the asynchronous case.

The asynchronous decay will subsequently be discussed analogously to the sequential decay, i.e. the action of the forces governing the first bond cleavage at time t_1 is supposed to be over when the second bond cleavage takes place at time t_2. The momenta and the kinetic energies of the final fragments can then be described, as is the case for the sequential decay, by introducing the decay angle θ and the energy deposition E_{AB} as parametric quantities. As before, no other parameter is needed in order to characterize the energy partitioning of the process. This implies that the description of the asynchronous concerted decay is formally identical with the description of the sequential case, and the same equation (52) gives the relationship between the fragment kinetic energy and the parameter values not only for the sequential, but also for the asynchronous concerted mechanism, as well as all subsequent considerations on maximum and minimum energy transfer hold in both cases.

The difference between the two cases is found in the dependence of the second decay step on the first one, such that there remains a memory of the geometry of the parent molecule at time t_1. For this reason the probability of realizing a certain decay angle is not equally distributed among all possible values as before, but is determined by the first decay step. Whereas the energy surface of figure 3, derived for the sequential mechanism, remains the same, the accessible region is restricted by a non-uniform distribution of the decay angle θ. The differences will become prominent below, when the influences of parameter distributions on the fragment kinetic energy distributions are discussed, and it will be seen that, although the equations describing the two different mechanisms are formally the same, the kinetic energy distributions can be very different, so that the experimental observation of the latter allows one to distinguish between these two mechanisms.

5.2. *Parameter distributions and fragment kinetic energy distributions*

The analytic relationship between the kinetic fragment energies and the parameter values has been established in the preceding section, and this section focuses on the

effects that parameter distributions have on the probability of observing a certain value for the kinetic energy of a fragment. Here we present an illustrative approach, while the rigorous mathematical derivation of the formulae is given elsewhere [184].

For the following general considerations the parameter quantities that were introduced in the preceding chapters are denoted by P_i where i is a running number, counting the parameter quantities. In principle, there is no upper limit for the total number N_P of parameters, but if it becomes too large, it might become impossible to actually calculate the kinetic energy distribution, or the analysis might not yield physically meaningful results. The models presented above need at most two parameter quantities, so that calculations of kinetic energy distributions from a given set of parameter distributions should be easily performed, as it will be possible in general to interpret observed kinetic energy distributions in terms of the underlying mechanisms and their parameter distributions.

The probability of realizing a certain fragment kinetic energy E_kin within an interval ΔE_kin is determined by the abundance of parameter values P_i that cause a kinetic energy in the given interval ΔE_kin. The determination of this abundance requires, independently of the exact form of the parameter distribution, knowledge of the width of the respective parameter intervals ΔP_i, within which the parameter P_i will give rise to a kinetic energy $E_\mathrm{kin}(P_i)$ in the interval ΔE_kin. If the gradient $\partial E_\mathrm{kin}/\partial P_i$ has a large value in the interval ΔP_i, i.e. if a small change in the value of P_i induces a large change in the kinetic energy $E_\mathrm{kin}(P_i)$, then the corresponding interval ΔP_i is small, and so is the probability of finding a parameter value P_i within this interval ΔP_i. On the contrary, for weak gradients $\partial E_\mathrm{kin}/\partial P_i$ the corresponding interval ΔP_i is large, i.e. the probability of finding a parameter value P_i within this interval ΔP_i is large also. Of course, if there is more than one parameter, all of them have to be considered at the same time, since they depend not only on the kinetic energy value E_kin, but also on one another: $P_i = P_i(E_\mathrm{kin}, P_j)$. Only if the total number of parameters $N_\mathrm{P} = 1$, is the influence of the parameter distribution reduced to the gradient, which even in this simple case has still to be weighted by the amplitude of the parameter distribution function. In general, the process corresponds to a projection of the N_P-dimensional hypersurface $E_\mathrm{kin}(P_i)$ onto the E_kin axis. The considerations up to this point are sufficient in those cases where all parameter distributions $f_i(P_i)$ have constant amplitudes. Then the projection onto the E_kin axis describes the kinetic energy distribution $f_\mathrm{E}(E_\mathrm{kin})$ completely and correctly. If this is not the case, i.e. if only one parameter is not equally distributed, then the parameter intervals ΔP_i that belong to the interval of the kinetic energy ΔE_kin have to be weighted with the amplitudes of the parameter distributions $f_i(P_i)$.

For the cases relevant to our studies, i.e. for $N_\mathrm{P} = 1$ and $N_\mathrm{P} = 2$, one obtains:

$$f_\mathrm{E}(E_\mathrm{kin}) = f_1[P_1(E_\mathrm{kin})]\left|\frac{\partial P_1}{\partial E_\mathrm{kin}}(E_\mathrm{kin})\right| \qquad \text{for } N_\mathrm{P} = 1 \quad (57a)$$

$$f_\mathrm{E}(E_\mathrm{kin}) = \int_{\mathrm{L}(E_\mathrm{kin})}^{\mathrm{U}(E_\mathrm{kin})} \mathrm{d}P_2 \left\{ f_2(P_2) f_1[P_1(E_\mathrm{kin}, P_2)] \left|\frac{\partial P_1}{\partial E_\mathrm{kin}}(E_\mathrm{kin}, P_2)\right| \right\} \qquad \text{for } N_\mathrm{P} = 2 \quad (57a)$$

Equation (57*a*) is valid without any restrictions for arbitrary parameter distribution functions P_i, as long as the derivative $\partial P_i/\partial E_\mathrm{kin}$ exists for E_kin, which is always the case for physically sensible distributions. Equation (57*b*) is valid only where a monotonic dependence $E_\mathrm{kin}(P_i)$ exists, i.e. if within the integration range from $\mathrm{L}(E_\mathrm{kin})$ to $\mathrm{U}(E_\mathrm{kin})$

the expression $\partial P_1/\partial E_{kin}$ is unambiguously defined and does not change its sign. If these requirements are not met, the absolute values of the derivatives $\partial P_1/\partial E_{kin}$ have to be summed up for every monotonic segment of the function $E_{kin}(P_1)$. Subsequently we assume that the monotony condition for $E_{kin}(P_1)$ is fulfilled so that no multiple integration is required and that the integrand is completely represented by the absolute value of the derivative of the inverse function $P_1(E_{kin})$ multiplied by the amplitudes of the parameter distribution functions. The determination of the integration limits that have rather formally been designated $L(E_{kin})$ and $U(E_{kin})$ in equation (57*b*) demands another critical examination. In general, it is not possible to derive an analytic expression for the calculation of the integration limits. Instead, it is necessary in every single case to determine $L(E_{kin})$ and $U(E_{kin})$ as those minimum and maximum values of the parameter P_2 (which is the one integrated over) that can realize the kinetic energy value E_{kin} for any parameter value P_1 (which is not integrated over). This can in general be accomplished by the determination of the minima and the maxima of the inverse function $P_2(E_{kin}, P_1)$. One has to take into account, however, the restriction with respect to the monotony of $E_{kin}(P_1, P_2)$.

Equation (57*a*) has to be evaluated for the discussion of synchronous three body decays, since the only parameter necessary in the characterization of such a process is the bond angle α at the fragmentation time. On the contrary, two parameters, the decay angle θ and the energy deposition E_{AB}, are needed for the analysis of the sequential and the asynchronous concerted decays. Thus, in the latter cases equations (57*a*) and (57*b*) form the basis for the calculation and the interpretation of the kinetic energy distributions, depending on whether fragment C resulting from the first, or fragments A and B, resulting from the second bond cleavage, are being investigated.

5.2.1. *The synchronous mechanism*

Accordingly, in the case of a synchronous decay, the kinetic energy distribution $f_E^{syn}(E_{kin})$ is related to the parameter distribution $f_\alpha(\alpha)$ of the bond angle via the following equation:

$$f_E^{syn}(E_{kin}) = f_\alpha[\alpha(E_{kin})]\left|\frac{\partial\alpha}{\partial E_{kin}}(E_{kin})\right|. \tag{58}$$

In order to calculate the kinetic energy distribution, the inverse functions $\alpha(E_k)$ from equations (34) and (35) have to be known, which connect the fragment kinetic energies with the bond angle α:

$$\alpha(E_{kin,A}) = 2\arccos\left[\frac{m_B}{\mu_{AC}}\left(\frac{\varepsilon}{E_{kin,A}} - \frac{m_A+m_C}{m_C}\right)\right]^{1/2} \quad \text{for fragment A} \tag{59a}$$

$$\alpha(E_{kin,B}) = 2\arccos\left[\frac{m_B}{4\mu_{AC}}\left(\frac{E_{kin,B}}{\varepsilon - E_{kin,B}}\right)\right]^{1/2} \quad \text{for fragment B} \tag{59b}$$

$$\alpha(E_{kin,C}) = 2\arccos\left[\frac{m_B}{4m_C}\left(\frac{\varepsilon}{E_{kin,C}} - \frac{m_A+m_C}{m_A}\right)\right]^{1/2} \quad \text{for fragment C} \tag{59c}$$

Owing to the bond angle range $0 \leqslant \alpha \leqslant \pi$, the inverse functions are unambiguously defined and the kinetic energy distributions are given by inserting expressions (59) into equation (58):

$$f_{\mathrm{E}}^{\mathrm{syn}}(E_{\mathrm{kin,\,A}}) = \frac{\varepsilon}{E_{\mathrm{kin,\,A}}^2} f_\alpha[\alpha(E_{\mathrm{kin,\,A}})] \Big/ \left\{ \left[\frac{4m_{\mathrm{A}}}{m_{\mathrm{B}}} - \left(\frac{\varepsilon}{E_{\mathrm{kin,\,A}}} - \frac{m_{\mathrm{A}}+m_{\mathrm{C}}}{m_{\mathrm{C}}} \right) \right] \left(\frac{\varepsilon}{E_{\mathrm{kin,\,A}}} - \frac{m_{\mathrm{A}}+m_{\mathrm{C}}}{m_{\mathrm{C}}} \right) \right\}^{1/2} \tag{60a}$$

$$f_{\mathrm{E}}^{\mathrm{syn}}(E_{\mathrm{kin,\,B}}) = \frac{\varepsilon}{E_{\mathrm{kin,\,B}}(\varepsilon - E_{\mathrm{kin,\,B}})} f_\alpha[\alpha(E_{\mathrm{kin,\,B}})] \Big/ \left[\frac{4\mu_{\mathrm{AC}}}{m_{\mathrm{B}}} \left(\frac{\varepsilon}{E_{\mathrm{kin,\,B}}} - 1 \right) - 1 \right]^{1/2} \tag{60b}$$

$$f_{\mathrm{E}}^{\mathrm{syn}}(E_{\mathrm{kin,\,C}}) = \frac{\varepsilon}{E_{\mathrm{kin,\,C}}^2} f_\alpha[\alpha(E_{\mathrm{kin,\,C}})] \Big/ \left\{ \left[\frac{4m_{\mathrm{C}}}{m_{\mathrm{B}}} - \left(\frac{\varepsilon}{E_{\mathrm{kin,\,C}}} - \frac{m_{\mathrm{A}}+m_{\mathrm{C}}}{m_{\mathrm{A}}} \right) \right] \left(\frac{\varepsilon}{E_{\mathrm{kin,\,C}}} - \frac{m_{\mathrm{A}}+m_{\mathrm{C}}}{m_{\mathrm{A}}} \right) \right\}^{1/2}. \tag{60c}$$

Using the relations derived in equations (60) the kinetic energy distribution can be described unambiguously, provided the internal energies of all fragments that are contained in the 'effective' available energy ε, the fragment masses and the parameter distribution $f_\alpha(\alpha)$ are known. Except for the latter, all these quantities are observable, so that it is possible to determine the parameter distribution from the measurement of the kinetic energy distribution. This determination is most effectively performed by adjusting a trial distribution by a least squares fit, until the parameter distribution is best described in accordance with the observed kinetic energy distribution.

Up to now no assumptions have been made in the description of the model of the decay mechanism. Now the explicit choice of a trial distribution, however, requires us to do so, which has to be taken into account when physically interpreting the results. In order to minimize the number of fitting parameters, we will assume that the bond angle is distributed around one single value α_0, such that the parameter distribution can be described by a Gaussian distribution of width $\Delta\alpha$. Then the fit procedure has to yield the values of α_0 and of $\Delta\alpha$. The use of a Gaussian distribution function:

$$f_\alpha(\alpha) \approx \exp\left[-\frac{(\alpha-\alpha_0)^2}{2\Delta\alpha^2} \right] \quad \text{where } \alpha = \alpha(E_{\mathrm{kin}}), \tag{61}$$

also includes the cases of a sharp, delta-like distribution function (for $\Delta\alpha \to 0$) and of constant amplitudes (for $\Delta\alpha \to \infty$).

5.2.2. *The sequential mechanism*

The analogous description of the sequential and the asynchronous concerted mechanism requires the evaluation of either equation (57*a*) or of equation (57*b*), depending on which fragmentation step produces the studied fragment. For fragment C, which is produced in the first fragmentation step, only the energy deposition E_{AB} has to be taken into account, whereas for the fragments A and B the decay angle θ has to be dealt with also. In principle, any one of the two parameters could be integrated over, but in this case it is useful to choose the energy deposition E_{AB} as the integration variable, because for a given value of E_{kin} the decay angle θ and its derivative $\partial\theta/\partial E_{\mathrm{kin}}$ are unambiguously defined when integrating over E_{AB}. This is not the case if the integration variable is chosen to be the decay angle θ (see discussion of monotony of $E_{\mathrm{kin}}(E_{\mathrm{AB}}, \theta)$ in the preceding section).

The kinetic energy distribution $f_{\mathrm{E}}(E_{\mathrm{kin,\,C}})$ for particle C generated in the first fragmentation step is, analogously to equation (58), given by

$$f_{\mathrm{E}}^{\mathrm{seq}}(E_{\mathrm{kin,\,C}}) = f_{\mathrm{AB}}[E_{\mathrm{AB}}(E_{\mathrm{kin,\,C}})] \left| \frac{\partial E_{\mathrm{AB}}}{\partial E_{\mathrm{kin,\,C}}}(E_{\mathrm{kin,\,C}}) \right|. \tag{62}$$

Making use of the inverse function $E_{AB}(E_{kin,\,C})$:

$$E_{AB}(E_{kin,\,C}) = E_{av} - E_{int,\,C} - \frac{m_{ABC}}{m_{AB}} E_{kin,\,C}, \tag{63}$$

one obtains the simple proportional relationship

$$f_E^{seq}(E_{kin,\,C}) = f_{AB}[E_{AB}(E_{kin,\,C})] \frac{m_{AB}}{m_{ABC}} \tag{64}$$

between the distribution $f_E^{seq}(E_{kin,\,C})$ of the kinetic energy of fragment C and the distribution $f_{AB}(E_{AB})$ of the energy deposition in the intermediate particle.

In order to calculate the kinetic energy distributions of the fragments A and B, generated in the second fragmentation step, one has to determine the respective inverse functions $\theta(E_{AB}, E_{kin})$ and their derivatives with respect to E_{kin}:

$$\theta(E_{AB}, E_{kin,\,A}) = \arccos\left[\frac{E_{kin,\,A} - p_0 - M_{AB} E_{AB}}{M_\theta (p_2 + p_1 E_{AB} - E_{AB}^2)^{1/2}}\right] \tag{65}$$

$$\frac{\partial \theta}{\partial E_{kin,\,A}}(E_{AB}, E_{kin,\,A}) = \frac{1}{M_1[-E_{AB}^2 + 2a(E_{kin,\,A}) E_{AB} + b(E_{kin,\,A})]^{1/2}}, \tag{66}$$

where M_1, $a(E_{kin,\,A})$ and $b(E_{kin,\,A})$ are the following abbreviations:

$$M_1 = (M_\theta^2 + M_{AB}^2)^{1/2} \tag{67a}$$

$$a(E_{kin,\,A}) = \frac{M_\theta^2 p_1 + 2M_{AB}(E_{kin,\,A} - p_0)}{2(M_\theta^2 + M_{AB}^2)} \tag{67b}$$

$$b(E_{kin,\,A}) = \frac{M_\theta^2 p_2 - (E_{kin,\,A} - p_0)^2}{M_\theta^2 + M_{AB}^2}. \tag{67c}$$

The expression under the integral of equation (57*b*) is now determined. Considerations as to whether the integral can analytically be solved follow after the determination of the integration limits $L(E_{kin,\,A})$ and $U(E_{kin,\,A})$. Due to the unambiguity of the inverse function $\theta(E_{AB}, E_{kin,\,A})$ the integration limits are the minimum and the maximum values of the inverse function $E_{AB}(\theta, E_{kin,\,A})$. The calculation of the inverse is not difficult, but nevertheless tedious, so it is useful to think for a while about those decay angles that correspond to the extreme values of the inverse function for a given kinetic energy. As has been discussed before, the maximum and the minimum values for the energy deposition for a given kinetic energy are realized for forward and backward scattering, respectively, i.e. either for $\theta = 0$ or for $\theta = \pi$, in any case for $\cos^2\theta = 1$. This is easily understood, if it is considered that for forward and backward scattering the energy deposited in the intermediate AB is completely used up for accelerating or decelerating the respective fragment instead of changing its direction of motion. Since the bond angle θ appears only as $\cos^2\theta$ when taking the inverse function, the abbreviations defined in equations (67) can be used, and the inverse E_{AB} ($\theta = 0, \pi; E_{kin,\,A}$) is given by

$$E_{AB}(\theta = 0, \pi; E_{kin,\,A}) = a(E_{kin,\,A}) \pm [a(E_{kin,\,A})^2 + b(E_{kin,\,A})]^{1/2}. \tag{68}$$

Thus, the integration limits can be expressed as

$$\begin{aligned} L(E_{kin,\,A}) &= a(E_{kin,\,A}) - [a(E_{kin,\,A})^2 + b(E_{kin,\,A})]^{1/2} \\ U(E_{kin,\,A}) &= a(E_{kin,\,A}) + [a(E_{kin,\,A})^2 + b(E_{kin,\,A})]^{1/2} \end{aligned} \tag{69}$$

so that the kinetic energy distribution of fragment A becomes

$$f_{\mathrm{E}}^{\mathrm{seq}}(E_{\mathrm{kin,\,A}}) = \int_{a(E_{\mathrm{kin,\,A}})-[a(E_{kin,A})^2+b(E_{\mathrm{kin,\,A}})]^{1/2}}^{a(E_{\mathrm{kin,\,A}})+[a(E_{kin,A})^2+b(E_{\mathrm{kin,\,A}})]^{1/2}} \mathrm{d}E_{\mathrm{AB}} \left\{ \frac{f_{\mathrm{AB}}(E_{\mathrm{AB}})\, c_\theta}{[-E_{\mathrm{AB}}^2 + 2a(E_{\mathrm{kin,\,A}})\, E_{\mathrm{AB}} + b(E_{\mathrm{kin,A}})]^{1/2}} \right\}. \quad (70)$$

with the integration limits determined above the integral yields real values only, as is required for an observable quantity.

We have replaced the distribution function $f_\theta(\theta) = \mathrm{d}\sigma/\mathrm{d}\theta$ by a constant value c_θ, thus implying that every decay angle is equally probable to be realized. We note again at this point that the distribution function $f_\theta(\theta)$ is the integral over the differential cross-section $\mathrm{d}\sigma/\mathrm{d}\Omega$ and might be also viewed as the two-dimensional distribution function of a dissociation process confined to a plane, in which case the consequences of the specific form of $f_\theta(\theta)$ are more easily rationalized than for the integrated quantity. In neither case must $f_\theta(\theta) = \mathrm{d}\sigma/\mathrm{d}\theta$ and $\mathrm{d}\sigma/\mathrm{d}\Omega$ be confused with each other. The latter is the scattering angle distribution observed in a standard PTS experiment and is therefore often dealt with in data analyses, causing the prominent forward–backward peaking for long-lived intermediates [41–44]. These differences are not contradictory, but merely due to the definitions used.

The specific form of a constant distribution function for the planar decay angle is correct only, however, if the rotational angular momentum vector is strictly perpendicular with respect to the velocity vector of the intermediate. While this is indeed a limitation of the presented equations, it is not at all a limitation with respect to the application of the model. The same is true, of course, for the observable PTS scattering angle distribution. Where the strictly negative $\langle \mathbf{v}\cdot\mathbf{J}\rangle$ correlation does not hold, the analytic expression for $f_\theta(\theta)$ has to be changed correspondingly [46–50]. The fully isotropic delay would result in a decay angle distribution which is proportional to $\sin\theta$ within our model, and in a constant scattering angle distribution without the common forward–backward peaking feature. We restrict ourselves to the impulsive case because for the photodissociation of phosgene presented below, the negative $\langle \mathbf{v}\cdot\mathbf{J}\rangle$ correlation must hold due to the atomic nature of the dissociation partner in the first step ($COCl_2 + h\nu \rightarrow COCl + Cl$), where the spin of the Cl atom has not been considered.

Accordingly to obtain the kinetic energy distribution one has to evaluate the integral over the following expression:

$$\frac{f_{\mathrm{AB}}(E_{\mathrm{AB}})}{[-E_{\mathrm{AB}}^2 + 2a(E_{\mathrm{kin,\,A}})\, E_{\mathrm{AB}} + b(E_{\mathrm{kin,\,A}})]^{1/2}}. \quad (71)$$

The value of the integral depends on the parameter distribution $f_{\mathrm{AB}}(E_{\mathrm{AB}})$. Using the same arguments as before, we will choose a Gaussian distribution function as a trial function, which is centred around $E_{\mathrm{AB,\,0}}$ with a characteristic width of ΔE_{AB}:

$$f_{\mathrm{AB}}(E_{\mathrm{AB}}) \approx \exp\left[-\frac{(E_{\mathrm{AB}} - E_{\mathrm{AB,\,0}})^2}{2\Delta E_{\mathrm{AB}}^2} \right]. \quad (72)$$

The integral resulting from this trial function cannot in general be solved analytically. A numerical evaluation, however, can always be performed, allowing the optimization of $E_{\mathrm{AB,\,0}}$ and ΔE_{AB} by a nonlinear least squares method. We will present some limiting cases below that can be solved analytically and also some numerically calculated

kinetic energy distributions for those cases where this cannot be done due to the complexity of the parameter distribution function $f_{AB}(E_{AB})$.

5.2.3. *The asynchronous mechanism*

The asynchronous concerted mechanism can be described similarly to the sequential mechanism. The difference is that the decay angle θ is not equally distributed. Of course, this difference can be felt only in the second fragmentation step, so that without further considerations the kinetic energy distribution for fragment C is given by the same expression as in equation (64).

For the second fragmentation step, the explicit form of the decay angle distribution function $f_\theta(\theta)$ has to be taken into account in calculating the integral according to equation (57*b*), so that in general the kinetic energy distribution has to be calculated numerically. The integration limits remain unchanged, because they do not depend on the specific form of $f_\theta(\theta)$. The kinetic energy distribution for fragment A is then given by

$$f_E^{\text{conc}}(E_{\text{kin, A}}) = \int_{a(E_{\text{kin, A}})-[a(E_{\text{kin, A}})^2+b(E_{\text{kin, A}})]^{1/2}}^{a(E_{\text{kin, A}})+[a(E_{\text{kin, A}})^2+b(E_{\text{kin, A}})]^{1/2}} \mathrm{d}E_{AB} \times \left\{ \frac{f_{AB}(E_{AB}) f_\theta[\theta(E_{\text{kin, A}}, E_{AB})]}{[-E_{AB}^2 + 2a(E_{\text{kin, A}})E_{AB} + b(E_{\text{kin, A}})]^{1/2}} \right\}. \tag{73}$$

Useful trial functions for the parameter distribution functions are again Gaussian distributions:

$$f_{AB}(E_{AB}) \approx \exp\left[-\frac{(E_{AB} - E_{AB,0})^2}{2\Delta E_{AB}^2} \right] \tag{74}$$

$$f_\theta[\theta(E_{\text{kin}}, E_{AB})] \approx \exp\left[-\frac{(\theta(E_{\text{kin}}, E_{AB}) - \theta_0)^2}{2\Delta\theta^2} \right]. \tag{75}$$

In order to fit the parameter distributions $f_{AB}(E_{AB})$ and $f_\theta(\theta)$ to the experimentally observed kinetic energy distributions' four fit parameters θ_0, $\Delta\theta$, $E_{AB,0}$ and ΔE_{AB} are to be used.

Tables 3–5 contain the general relationships between kinetic energy distributions and parameter distribution in comprehensive form. In the next section some examples will illustrate the matter discussed above.

5.3. *Some examples*

5.3.1. *The synchronous decay*

Some calculated kinetic energy distributions for the fragments A and B, resulting from the synchronous decay of a symmetric parent molecular ABA, are shown in figure 4. As outlined before, Gaussian distribution functions have been used to simulate the distribution of the bond angle α. A common width of $\Delta\alpha = 10°$ has been applied to distributions about centres α_0 of 60°, 90°, 120° and 150° (top to bottom). The Gaussian parameter distribution yields almost Gaussian, but slightly skewed kinetic energy distributions, which have lesser widths for smaller bond angles α_0, due to the decreasing value of the gradient $\mathrm{d}\alpha/\mathrm{d}E$. The scaling of the kinetic energy axis refers in all cases to the total kinetic energy ε (i.e. $E_{\text{kin}} = 0{\cdot}7$ means $E_{\text{kin}} = 70\%$ of ε). The masses of all particles are assumed to be equal (i.e. $m_A = m_B$), so that in accordance with equations (34) and (35) the limiting values of the kinetic energies are

$$\varepsilon/6 \leqslant E_{\text{kin, A}} \leqslant \varepsilon/2 \quad \text{and} \quad 0 \leqslant E_{\text{kin, B}} \leqslant 2\varepsilon/3.$$

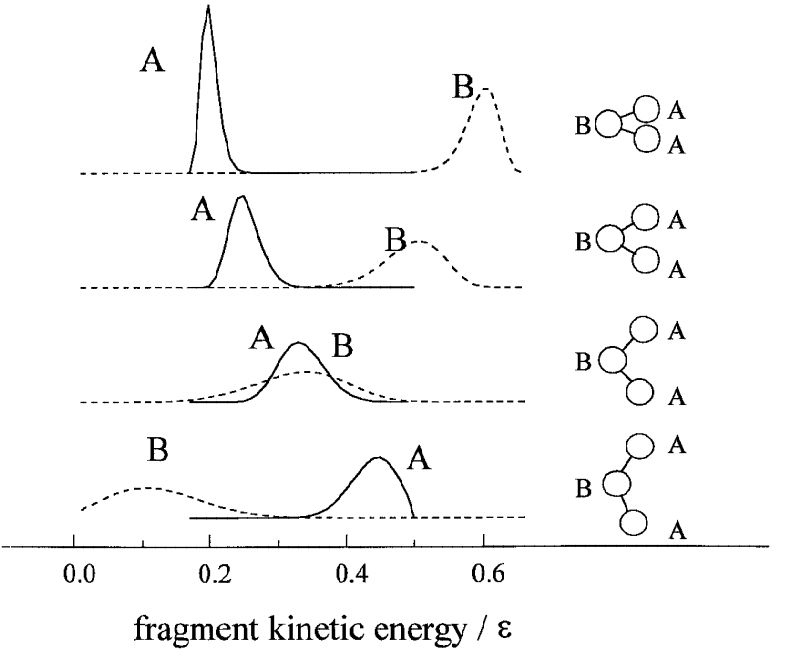

Figure 4. Simulations of fragment kinetic energy distributions for a synchronous decay of a symmetric parent molecule ABA with $m_A = m_B$. The bond angle distribution $f_\alpha(\alpha)$ was assumed to be a Gaussian distribution with a width of 10°, with distribution centres α_0 = 60°, 90°, 120° and 150°, respectively, increasing from the top to the bottom trace. The mean kinetic energy of fragment A increases with increasing bond angle α, while the kinetic energy of fragment B correspondingly decreases.

5.3.2. *The sequential decay*

All subsequently discussed cases, including sequential decays as well as asynchronous concerted decays, have been calculated for atomic fragments (i.e. $E_{int} = 0$), having mass ratios of $m_A/m_B = m_C/m_B = 5/4$, if numbers are given. Energies are given in units of E_{av}. For non-atomic fragments which internal degrees of freedom E_{av} has to be replaced by p_0.

An analytic solution of equation (70) for a sequential decay exists only for two cases:

(a) for a sharp, delta-like distribution of the energy deposition: $f_{AB}(E_{AB}) = \delta(E_{AB} - E_0)$,

(b) if the distribution of the energy deposition is constant in the whole range for E_{AB}: $f_{AB}(E_{AB}) = \text{const.} = c_{AB}$ for $0 \leqslant E_{AB} \leqslant E_{av}$.

The first case is described by a vanishing width of the parameter distribution ($\Delta E_{AB} \to 0$), whereas for the second case the width of the parameter distribution tends to infinity ($\Delta E_{AB} \to \infty$).

In the first case ($\Delta E_{AB} \to 0$) the integral disappears due to the action of the δ-function in the numerator, and one obtains the following analytical solution for the kinetic energy distribution of the fragment A:

$$f_E(E_{kin,\,A}) \propto \frac{1}{[-E_{AB}^2 + 2a(E_{kin,\,A})\,E_{AB} + b(E_{kin,\,A})]^{1/2}}. \tag{76}$$

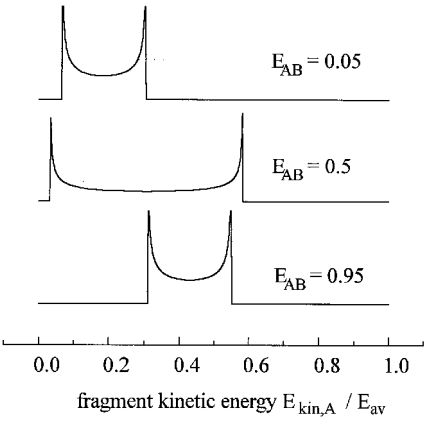

Figure 5. Simulated kinetic energy distributions of fragment A for a sequential decay with sharp distribution of the energy deposition E_{AB}, with increasing energy deposition values from top to bottom. The average kinetic energy increases with increasing energy deposition. The most abundant kinetic energies are found at the edges of the distributions.

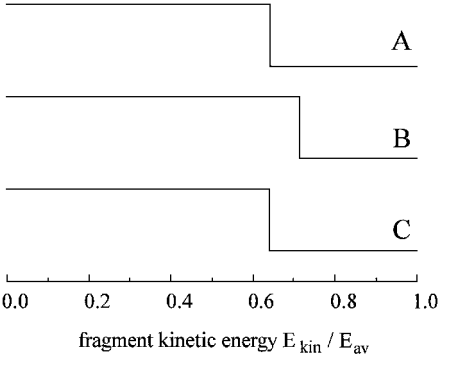

Figure 6. Simulation of the kinetic energy distributions of all fragments for a sequential mechanism with a constant distribution of the energy deposition. All kinetic energy distributions also have constant amplitudes. Maximum and minimum kinetic energies are defined by the mass ratios of the fragments.

The accessible range for the kinetic energy is restricted by the integration limits in equation (69). f_E is an unambiguous function of the two variables $E_{kin,\,A}$ and E_{AB}. The kinetic energy of fragment C is single-valued: $E_{kin,\,c} = m_{AB}/m_{ABC}(E_{av} - E_{AB} - E_{int,\,C})$. The kinetic energy distribution of fragment A is very broad for medium values of the energy deposition and becomes narrower for large as well as for small values of E_{AB}. For $E_{AB} = 0$ and $E_{AB} = 1$ it becomes single-valued, too. At the same time the centre of the kinetic energy distribution is shifted from low to high kinetic energies when increasing the energy deposition. Since the kinetic energy $E_{kin,\,A}$ for forward and backward scattering is only negligibly changed for a change in the decay angle, it is easily understood that the maximum and the minimum values for the kinetic energy at a given energy deposition E_{AB} are the most probable ones. This manifests itself mathematically in equation (76) by the fact that the denominator vanishes at the integration limits. Figure 5 illustrates the kinetic energy distributions of fragment A for three sharply defined values of the energy deposition.

In the second case ($\Delta E_{AB} \to \infty$), it is obvious from equation (64) that the kinetic

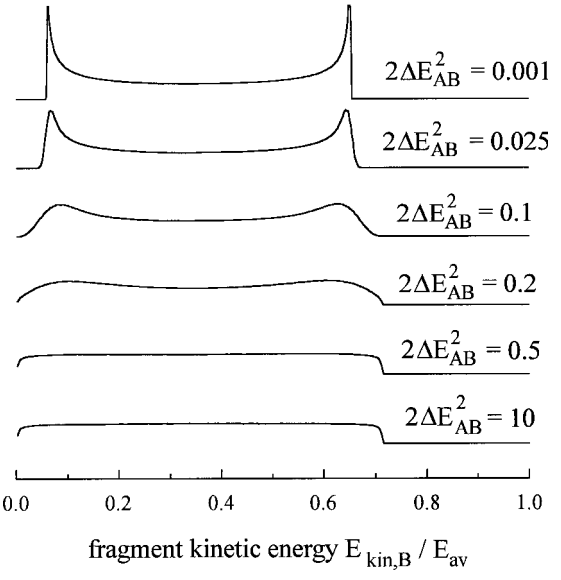

Figure 7. Simulation of the kinetic energy distributions for fragment B resulting from a sequential decay. The average energy deposition has been assumed to be 0•5 E_{av}. The width of the parameter distribution increases in going from the top to the bottom trace. The upper trace corresponds to a sharp distribution, as shown in figure 5, whereas the lower trace describes the constant amplitude case, described in figure 6.

energy of fragment C, which is generated in the first decay step, is likewise equally distributed as the energy deposition E_{AB}. For the fragments A and V, resulting from the second decay step, the numerator of the fraction under the integral in equation (70) becomes constant and the integration limits are equal to the two poles of the denominator expression so that the integral yields real values only. Surprisingly, performing the integration yields constant values for the kinetic energy distributions of both fragment A and B:

$$f_E(E_{kin,A}) = \text{const.}, \quad f_E(E_{kin,B}) = \text{const.}, \quad f_E(E_{kin,C}) = \text{const.} \tag{77}$$

The accessible ranges for the kinetic energies of the final fragments are determined by the mass ratios of the fragments, as stated below and as illustrated in figure 6:

$$0 \leqslant E_{kin,A} \leqslant \frac{m_B + m_C}{m_{ABC}} E_{av}.$$

$$0 \leqslant E_{kin,B} \leqslant \frac{m_A + m_C}{m_{ABC}} E_{av}.$$

$$0 \leqslant E_{kin,C} \leqslant \frac{m_A + m_B}{m_{ABC}} E_{av}. \tag{78}$$

After having discussed the limiting cases, we turn to those problems that arise from 'real' distributions of the energy deposition. Unfortunately, an analytical solution is not available for these problems. However, the character of the corresponding kinetic energy distributions should be intermediate with respect to the 'infinitely sharp' and the 'infinitively broad' distributions. That this is indeed the case can be seen from figure 7, where for the central trace of figure 5 ($E_{AB,0} = 0,5$) kinetic energy distributions

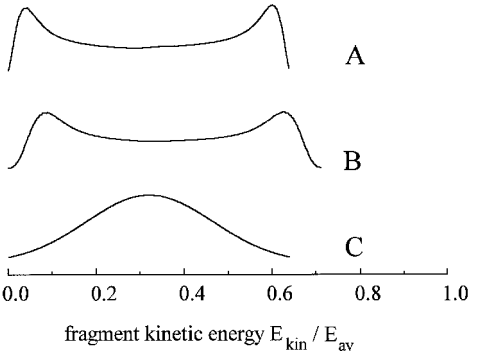

Figure 8. Simulated kinetic energy distributions for all fragments for a sequential decay with a parameter distribution corresponding to the third trace from the top in figure 7.

of particle A have been calculated for different widths ΔE_{AB} of the parameter distribution $f_{AB}(E_{AB})$. Any one of the depicted kinetic energy distributions has been calculated by summing up 500 single distributions that were calculated for single values of E_{AB} according to equation (76) after having been weighted by the amplitude of the distribution function $f_{AB}(E_{AB})$. The top traces, for narrow parameter distributions, resemble the kinetic energy distribution for the delta-like case with characteristic maxima at the edges of the distribution, whereas the lower traces, for broad parameter distributions, resemble the constant amplitude distribution, as discussed immediately before. The agreement of the numerically calculated lower trace in figure 7 with the analytically calculated middle trace in figure 6, which show identical distributions, is excellent. For intermediate widths of the parameter distribution a smooth transition takes place between the limiting cases. Different centres of the parameter distribution show qualitatively the same behaviour [184].

Thus, the following two features of a kinetic energy distribution resulting from a purely sequential decay have been obtained.

Every sequential decay induces a typical form of the kinetic energy distribution, which is characterized either by a double maximum at the edges of the distribution, marking forward and backward scattering for narrow parameter distributions, or by a (possibly skewed) rectangular shape for correspondingly broad parameter distributions. For none of the investigated cases could a shape be derived that was qualitatively different, e.g. resembling a single Gaussian kinetic energy distribution, without imposing severe restrictions on the internal energy distributions of the fragments or assuming an at least bimodal parameter distribution. In order to account for the possible influence of fragment internal energies, either the experimental set-up has to allow for measuring internal energies, e.g. by employing a spectroscopic technique, or the investigated system has to be carefully chosen in order to exclude internal energy contributions, e.g. if only atomic fragments are generated.

Even for relatively narrow parameter distributions the information about the centre of the distribution will be lost due to the broadening of the kinetic energy distribution, resembling the 'infinitely broad' case. Nevertheless, whereas the centre of the distribution loses some of its significance for broad distributions, the sequential character of the decay is always fully maintained.

We selected one of the kinetic energy distributions of figure 7 (top third, $E_{AB,0} = 0{\cdot}5$ and $\Delta E_{AB} = 0{\cdot}1$) and calculated the kinetic energy distributions for all fragments A, B and C. The results are shown in figure 8. The Gaussian distribution of the kinetic

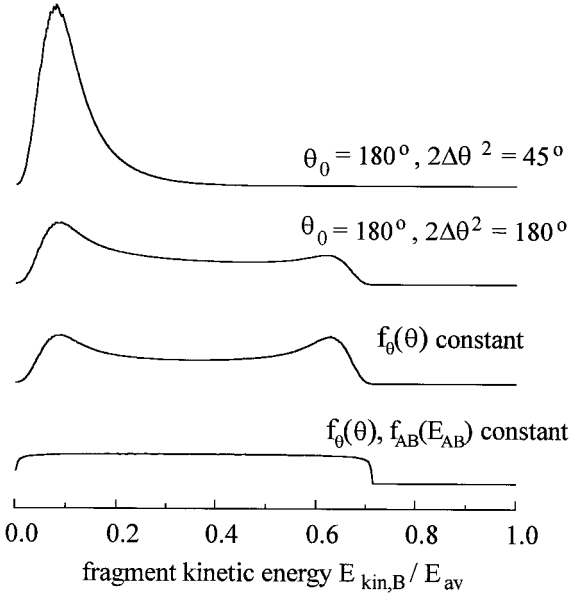

Figure 9. Simulated kinetic energy distributions of fragment B for an asynchronous concerted decay. Fragment B is backward scattered with a distribution of the energy deposition corresponding to figure 8. The width of the decay angle distribution $f_\theta(\theta)$ increases from top to bottom. The upper trace is characteristic for a pronounced backward scattering while the trace third from the top is equally distributed with respect to the decay angle and must be classified as being of sequential character. It is identical to the third trace from the top in figure 7. The lower trace corresponds to constant amplitude distributions for both parameters, the energy deposition E_{AB} and the decay angle θ.

energy of fragment C results from the proportionality relation of equation (64). The kinetic energy distribution for fragment B is very similar to the one for fragment A, except for the total width, which is slightly smaller due to the mass ratio m_A/m_B = 1•25. However, this must be the case for a sequential decay, in fact, for identical masses of m_A and m_B the kinetic energy distributions are also identical.

5.3.3. *The asynchronous decay*

The difference between the asynchronous concerted decay and the sequential decay is only due to the distribution function $f_\theta(\theta)$ of the decay angle θ, that additionally appears in the numerator in the integral of equation (73). In the preceding discussion of the sequential decay, the kinetic energy distributions of figure 6 were calculated for single values of the energy deposition E_{AB}. Every value of the kinetic energy in these distributions corresponds to one and only one value of the decay angle θ due to the unambiguous relationship between these two quantities. Introducing a distribution function $f_\theta(\theta)$ therefore selects those parts in the kinetic energy distribution that correspond to the preferred values of θ. To obtain the kinetic energy distributions for the asynchronous concerted decay, the respective distributions for single values of the energy deposition E_{AB} have to be modified in this way, to be weighted by the amplitude of the distribution $f_{AB}(E_{AB})$, similar to the procedure that has been used for the sequential decay, and to be summed up for all values of E_{AB}.

We subsequently employed this procedure in the case of backward scattering of fragment A. The sets of kinetic energy distributions depicted in figures 9–11 belong to

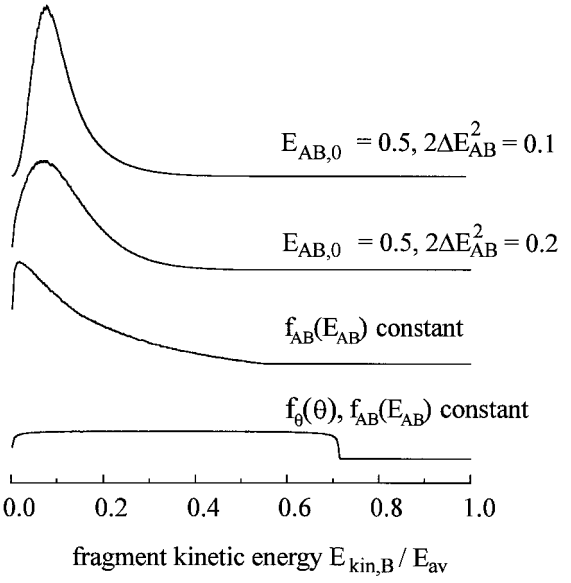

Figure 10. Corresponding simulated kinetic energy distributions as in figure 9 with identical start and end points, but a different transition from the top to the bottom trace. Instead of increasing the width of the decay angle distribution, here the width of the distribution of the energy deposition was increased.

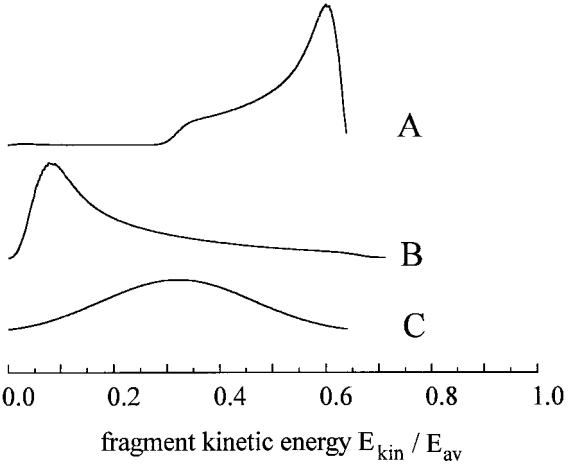

Figure 11. Simulated kinetic energy distributions for all fragments for an asynchronous concerted decay with parameter distributions intermediate between the top two traces in figure 9.

the same narrow distribution of the energy deposition E_{AB} that caused the purely sequential distributions of figure 8 ($E_{AB,0} = 0{\cdot}5$, $2\Delta E_{AB}^2 = 0{\cdot}1$). In figure 9 the distribution of the decay angle is broadened in going from the top to the bottom trace, thus the first trace, counting from top to bottom, represents strongly pronounced backward scattering, whereas the third trace depicts the case with no angular preference at all, which is of sequential character and has been shown before as the third trace in figure 7. The lower trace represents constant amplitudes of both the decay angle and the energy deposition.

The kinetic energy distributions of figure 10 show the transition form from pronounced backward scattering with narrow distribution of the energy deposition to the case of constant amplitudes for both parameter distributions as well, but contrary to the set shown in figure 9, here the distribution of the energy deposition has been broadened for a fixed distribution of the decay angle. It is obvious that start and end points in the series are identical, but the transition proceeds differently. In general, the angular anisotropy is more strongly pronounced in the latter set of kinetic energy distributions. Owing to the larger number of parameters the asynchronous concerted decay is capable of inducing a larger variety of kinetic energy distributions as the other two mechanisms discussed before.

Figure 11 is the analogue of figure 8 for the asynchronous concerted decay. For a set of parameter distributions all kinetic energy distributions of the three fragments were calculated. The parameter distributions were chosen to be similar to the ones used for calculating the kinetic energy distributions of figure 8: $E_{\mathrm{AB},\,0} = 0{\cdot}5$, $2\Delta E^2_{\mathrm{AB}} = 0{\cdot}1$, $\theta = 0°$ and $\Delta\theta = 90°$. Note that now fragment A is scattered in a forward direction, whereas fragment B is the one that is scattered backwards, and that the width of the angular distribution is intermediate between the top two traces depicted in figure 9. This intermediate width preserves the forward scattering character, but at the same time allows for a wide range of fragment kinetic energies. The effect of the forward scattering character, but at the same time allows for a wide range of fragment kinetic energies. The effect of the forward scattering is clearly seen for fragment A, carrying preferably high kinetic energy, whereas the distribution for fragment B, being scattered backwards, peaks at a kinetic energy value below 10% E_{av}. Both kinetic energy distributions show a low and a high energy 'tail', respectively, due to the width of the decay angle distribution, which allows a small fraction of the fragments to reverse the directions of motion. The kinetic energy distribution of fragment C is identical, of course, to the one presented for the sequential decay, since the first fragmentation step is the same for the two mechanisms.

Although the parameter distributions of the complete sets of kinetic energy distributions presented do not differ very much from each other, the energy distributions that would be observed in an experiment are not alike at all. Thus, from experimentally observing the fragment kinetic energy distributions, even subtle differences in the decay mechanisms can be detected by the kinematic analysis.

We have shown that each fragmentation mechanism induces fragment kinetic energy distributions that are specific for the respective parameter distributions. Vice versa it is possible to determine the character of the decay mechanism together with the corresponding parameter distribution having made a few plausible assumptions, e.g. Gaussian distributions of the parameter values. Every kinetic energy distribution can be described by the following expression:

$$\begin{aligned} f_{\mathrm{E}}(E_{\mathrm{kin}}) = {} & A^{\mathrm{syn}} f_{\mathrm{E}}^{\mathrm{syn}}(E_{\mathrm{kin}}, E_{\mathrm{int}}, \alpha_0, \Delta\alpha) \\ & + A^{\mathrm{seq}} f_{\mathrm{E}}^{\mathrm{seq}}(E_{\mathrm{kin}}, E_{\mathrm{int}}, E^{\mathrm{seq}}_{\mathrm{AB},\,0}, \Delta E^{\mathrm{seq}}_{\mathrm{AB}}) \\ & + A^{\mathrm{conc}} f_{\mathrm{E}}^{\mathrm{conc}}(E_{\mathrm{kin}}, E_{\mathrm{int}}, E^{\mathrm{conc}}_{\mathrm{AB},\,0}, \Delta E^{\mathrm{conc}}_{\mathrm{AB}}, \theta_0, \Delta\theta) \end{aligned} \tag{79}$$

Here the A^i are the contributions of the pure decay mechanism to the overall process, which implies that their sum has to equal unity: $A^{\mathrm{syn}} + A^{\mathrm{seq}} + A^{\mathrm{conc}} = 1$. E_{kin} and E_{int} are quantities that are observable in the experiment, whereas θ_0, $\Delta\theta$, $E_{\mathrm{AB},\,0}$, ΔE_{AB}, α_0 and $\Delta\alpha$ are the quantities characterizing the parameter distributions according to the previous sections. As outlined before, it does not have to be possible for every three body decay to unambiguously determine all contributions and the corresponding

parameters. However in most cases, only one or two of the pure mechanisms will operate in competition with each other, so that the number of parameters is significantly reduced, and an unambiguous interpretation of the experiment data becomes possible. Taking into account the significantly different shapes of the kinetic energy distributions, where only slight alterations of the underlying parameter distributions have been made, we feel that the kinematic analysis will be a powerful tool in the analysis of the three body decay.

6. Competing fragmentation channels in phosgene photodissociation

For a number of reasons we have applied our approach to the photodissociation of phosgene ($COCl_2$), where a three body decay generates two chlorine atoms and one carbon monoxide molecule:

$$COCl_2 + h\nu \rightarrow CO + 2\,Cl. \tag{80}$$

Firstly, owing to the relative simplicity of the parent molecule, the three body decay products do not possess many internal degrees of freedom that might obscure the effect of the underlying mechanisms. Second, all products are accessible to experimental observation. Third, the generation of an atomic fragment in the first bond cleavage, by whatever mechanism, assures the applicability of the model as presented above. Last, but not least, not much is known about primary photoproducts from reaction (80), although it possesses significance for tropospheric and stratospheric chemistry [185–187].

Phosgene is a planar star-like molecule with a carbon atom in the centre, which is doubly bound to an oxygen atom and singly bound to the two chlorine atoms. The ground state is C_{2v} with $^1A_1$ symmetry. Phosgene is the fully chlorinated analogue to formaldehyde (H_2CO) and, therefore, also resembles the acetone molecule ($(CH_3)_2CO$), both of which are by far better characterized with respect to their respective photochemical behaviour. The bond length $r_{C=O}$ between the carbon and the oxygen atom is $111{\cdot}6 \pm 0{\cdot}2$ pm, while the bond lengths r_{C-Cl} between the carbon the chlorine atoms amount to $14{\cdot}6 \pm 0{\cdot}4$ pm. The Cl–C–Cl bond angle is $\alpha = 111{\cdot}3 \pm 0{\cdot}1°$ [188, 189].

The rotational constants are $A = 0{\cdot}08049 \pm 0{\cdot}00002\ cm^{-1}$, $B = 0{\cdot}11675 \pm 0{\cdot}00002\ cm^{-1}$ and $C = 0{\cdot}26423 \pm 0{\cdot}00001\ cm^{-1}$ [188,189]. The eigenvalues of the normal modes lie between 285 cm^{-1} and 1827 cm^{-1} and are compiled in table 6. As expected, the softest vibrational mode is the Cl–C–Cl bending mode, while the strongest one is the C═O stretching mode [190–195]. The soft vibrational modes and the small rotational constants demand that experiments be performed under the low temperature conditions a supersonic jet provides, in order to limit the number of populated states of the parent molecule prior to the photodissociation. Even then, for moderate cooling to 15 K, the parent will carry angular momentum of ~ 7 quanta, if only the rotation about the principal axis is considered, which is the main source of angular momentum transfer from parent molecule rotation onto the CO fragment. As a result of the small rotational constants, this contribution is insignificant with respect to the energetics of the photodissociation. However, this excitation needs to be taken into account in an angular momentum analysis of the process.

The first, weak absorption continuum of phosgene starts at 305 nm and exhibits a maximum at 232 nm [196–200]. Contrary to the corresponding transition of formaldehyde it is only weakly structured. Over the entire range of the first continuum vibrational bands are observed, which are themselves featureless and could be

Table 6. Normal modes of the phosgene molecule.

Mode	Description	ω (cm^{-1})
ν_1	C–Cl symmetric stretch	567
ν_2	C═O stretch	1827
ν_3	Cl–C–Cl symmetric bend	285
ν_4	C–Cl antisymmetric stretch	849
ν_5	Cl–C–Cl antisymmetric bend	440
ν_6	Cl_2–C═O out of plane	582

assigned for the long wavelengths. The vibrational bands become increasingly diffuse for shorter wavelengths, which is thought to be due to predissociation of the excited state.

The absorption in this wavelength range excites phosgene from the X^1A_1 electronic ground state into the first electronically excited A^1A_2 state [199]. This transition is symmetry forbidden and exhibits only a small oscillator strength of $f = 1{\cdot}04 \times 10^{-3}$. It becomes symmetry allowed for a non-planar $COCl_2$. Within molecular orbital theory the transition corresponds to a $\pi^* \leftarrow$ n excitation of a non-bonding electron into an antibonding orbital of the CO bond [201]. Apart from an increase in the C═O bond length from 116·6 pm to 132·6 pm with a corresponding reduction of the eigenvalue of the C═O stretch from 1827 cm^{-1} to 1135 cm^{-1}, this excitation induces a non-planar configuration: the oxygen departs from the molecular plane, reducing the symmetry group from C_{2v} to C_s. The remaining molecular constants are only insignificantly affected [199].

The absorption of a photon in the first absorption continuum transfers sufficient energy in the phosgene molecule to dissociate it. Below we have compiled the energetically accessible decay channels for the absorption of a photon with a wavelength above 200 nm. They can be classified into three groups with chemically different products:

two molecular products CO and Cl_2: $COCl_2 + h\nu \rightarrow CO + Cl_2$, (81 *a*)

a chloroformyl radical and a chlorine atom: $COCl_2 + h\nu \rightarrow COCl + Cl$, (81 *b*)

a carbon monoxide and two chlorine atoms: $COCl_2 + h\nu \rightarrow CO + 2\,Cl$. (81 *c*)

In addition to the three body decay (81 *c*) two other decay channels can be operative, which we will call the molecular decay (81 *a*) and the radical decay (81 *b*). The energy of a photon with a wavelength above 200 nm is not sufficient to produce either electronically excited carbon monoxide or atomic carbon or oxygen. Table 7 lists the possible photoproducts in detail [75, 202].

So far the investigation of phosgene photodissociation [203–205] has been limited to final product analysis and kinetics. At a photolysis wavelength of 253 nm the CO quantum yield ϕ_{CO} (253 nm) is unit [205]. In experiments where radical scavengers were added, a sequential three body decay has been postulated, where first a chloroformyl radical (COCl) and a chlorine atom are produced, with the COCl radical carrying sufficient internal energy in order to decay into carbon monoxide and a second chlorine atom [203, 204]. This mechanism has also been suggested from theoretical calculations [206]. Only very recently has it been possible to directly observe chlorine atoms in their electronic $^2P_{3/2}$ ground state as primary photoproducts at a photolysis wavelength of 248 nm [207]. In a previous set of experiments we observed both $^2P_{3/2}$ ground state and $^2P_{1/2}$ excited spin–orbit state chlorine atoms at the slightly shorter

Table 7. Energetically accessible product channels for absorption of a photon with a wavelength above 200 nm: the molecular, the radical and the three body decay channel. The latter can produce chemically identical, but physically distinguishable products by the three decay mechanisms discussed in the text.

Decay	Products	Dissociation energy (cm^{-1})	Threshold wavelength (nm)	Remarks
Molecular	$CO(X^1\Sigma^+) + Cl_2(X^1\Sigma_g^+)$	8700	1149•4	
	$CO(X^1\Sigma^+) + Cl_2(A^3\Pi_{1u})$	26140	382•6	spin forbidden
	$CO(X^1\Sigma^+) + Cl_2(B^3\Pi_{0u}^+)$	26510	377•2	spin forbidden
Radical	$COCl(X^2A') + Cl(^2P_{3/2})$	26100	383•1	
	$COCl(X^2A') + Cl(^2P_{1/2})$	26980	370•6	
Three body	$CO(^1\Sigma^+) + Cl(^2P_{3/2}) + Cl(^2P_{3/2})$	28700	348•4	
	$CO(^1\Sigma^+) + Cl(^2P_{3/2}) + Cl^*(^2P_{1/2})$	29580	338•1	
	$CO(^1\Sigma^+) + Cl^*(^2P_{1/2}) + Cl^*(^2P_{1/2})$	30460	328•3	

dissociation wavelengths of 235 nm and 237 nm, respectively, by the REMPI—TOF technique [208]. No evidence of the radical channel was found, and the analysis of the spin polarization and the spin-selective kinetic energy distributions led us to propose a concerted, but non-synchronous mechanism to be active rather than a sequential one, with competing dissociation pathways being responsible for the observed spin-selectivity. We also predicted a significant internal excitation of the carbon monoxide fragments.

To complement the previous data we have additionally monitored the CO fragments by the same experimental procedure and treated the observed kinetic energy distributions by the kinematic analysis presented in the previous section.

6.1. *Experimental methods*

A detailed description of the experimental set-up of the experiment has been given elsewhere [184, 209]. Basically it consists of a home-built single-field TOF spectrometer with a ratio of the acceleration to the drift region of 1:2 at a total length of 58 cm. The spectrometer was evacuated to a base pressure of 10^{-4} Pa (10^{-6} mbar) by a 360 l s^{-1} turbo molecular pump and a 500 l s^{-1} oil diffusion pump. Pure phosgene (Messer Griesheim) was fed into the spectrometer via a supersonic jet, generated in an inductively driven pulsed nozzle (General Valve). The nozzle diameter was 0•5 mm, and the valve was operated at a stagnation pressure of typically 2×10^4 Pa (300 mbar) and a pulse duration of 250 μs, resulting in an operational background pressure of less than 10^{-3} Pa (10^{-5} mbar) at a repetition rate of 10 Hz.

Simultaneous dissociation of phosgene and state-selective detection of the CO molecules was performed using an excimer laser pumped dye laser (Lambda Physik LPD 3000, Lambda Physik LPX 605i). The dye laser operated with Coumarin 4–7 at a repetition rate of 10 Hz, its output was frequency doubled by a BBO crystal and focused into the spectrometer by a 200 mm quartz lens. It intersected the molecular beam at an angle of 54°, while the spectrometer formed an angle of 90° with the propagation direction of the laser beam. The angle between the spectrometer axis and the electric field vector of the linearly polarized laser light could be varied from 0° to 90° in order to investigate the spatial fragment distribution. The intensity of the laser light and the particle density in the supersonic beam were carefully controlled to avoid kinetic energy transfer onto the fragments due to space charge effects. The laser

intensity was typically kept around 200 μJ per pulse. The particle density in the expansion zone was varied in order to investigate the space charge induced distortion of the TOF profiles and was kept well below the onset of Coulomb distortion for the measurements.

The CO fragments were ionized by REMPI, using the $B^1\Sigma^+$ state as resonant intermediate [210–213]. The employed wavelength around 230·1 nm for realizing this (2 + 1) detection is almost at the maximum of the phosgene absorption spectrum, where it exhibits a cross-section of $1{\cdot}2 \times 10^{-19}$ cm^2. Under our detection conditions we realized a photon flux of more than 10^{19} photons per pulse cm^2. As a consequence, the dissociation as well as the ionization step were saturated, which was confirmed by the observation of a quadratic dependence of the ion signal intensity on the laser intensity.

The experimental performance of the set-up was greatly enhanced by operating the system in three modes: (a) the drift mode, (b) the acceleration mode and (c) the Doppler mode. In all modes the ions are detected by a double stage multichannel plate assembly (Galileo) with an active diameter of 40 mm. In the drift mode no acceleration field is applied. In this case the spectrometer consists simply of a drift tube with length s = 58 cm, and the time of flight t is inversely proportional to the (laboratory) speed v of the ion $t = s/v$. After passing a discriminator (FAST 7011), the ion signal is monitored by a multihit time-to-digital converter (FAST 7885) with a time resolution that can be varied from 5 ns to 80 ns, and stored in a data buffer (FAST MCD/PC). Typical acquisition times for a single TOF profile are 3000 s with a total of 3×10^5 ion counts. This mode is highly accurate for determining kinetic energies, but insensitive to slow particles due to the laboratory to centre of mass transformation that has to be performed when working in a supersonic expansion.

In the acceleration mode the ions are accelerated by a moderate static electric field of typically 10^3 V m^{-1} in the acceleration region and detected after passing the drift tube. Here the ions are mass selected, and instead of the total speed, the measured quantity is the velocity component v_x along the spectrometer axis, monitored by the mass peak broadening. A linear relationship between the velocity component v_x and the deviation Δt from the centre t_0 of the time of flight profile holds for our spectrometer geometry:

$$\Delta t = \frac{8t_0^2}{3s} v_x. \tag{82}$$

Since the velocity component v_x is perpendicular to the velocity of the molecular beam, no laboratory to centre of mass transformation has to be performed in this case. The ion signal is monitored by a digital oscilloscope (LeCroy 9450). This procedure is sensitive for all velocities down to zero, but, due to the shorter flight times, the accuracy in the determination of kinetic energies is lower than in the drift mode. Combining the two modes yields experimental data both with the high accuracy of the drift mode and the completeness of the acceleration mode.

The Doppler mode employs strong acceleration fields of the order of 10^4 V m^{-1} in order to assure the arrival of all ions that are generated in one laser pulse at the particle detector. This mode serves for the determination of quantum state populations. Although the Doppler broadening of the spectral lines has not been used for obtaining kinetic energy distributions due to the much lower accuracy compared to the evaluation of the TOF data, it is a most welcome tool to check for the correctness of the kinetic energy distributions, derived from the TOF measurements, by an independent method.

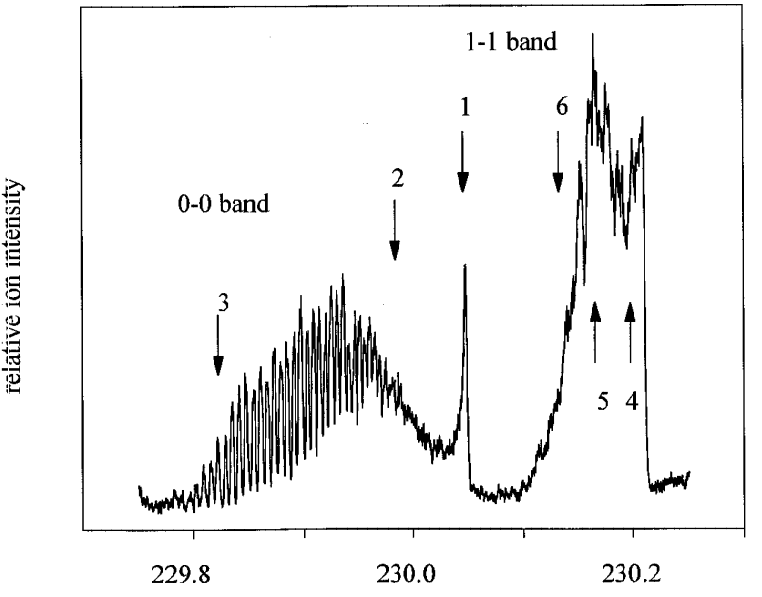

Figure 12. Experimentally observed Q branches of the 0–0 and the 1–1 bands of the B ← X transition of CO resulting from the photodissociation of phosgene at 230 nm. The intensities have been normalized with respect to the laser power. The rotational overlap in the 1–1 band is due to predissociation of the CO B state in $v = 1$. The arrows mark the states for which time of flight data have been obtained in order to derive the respective quantum state resolved kinetic energy distributions. The numbers are explained in table 6.

All three operational modes were calibrated with respect to their accuracy in determining kinetic energies by the well-characterized photodissociation of HI [212—216] at 243 nm and of molecular Cl_2 [212, 213, 217–223] at 308 nm, monitoring H [224–226] and Cl [226–228] fragments, respectively. The experimentally determined values are in excellent agreement with the values that were calculated from the spectrometer geometry. The kinetic energy resolution is energy dependent and is approximately 5% for the energy values encountered here, which has been experimentally verified by the Cl_2 dissociation data. Moreover, for the acceleration mode it was carefully checked that data from varied acceleration conditions yielded identical results. For all acquisition modes, the background signal was monitored immediately after each measurement, with the laser delayed with respect to the gas pulse under otherwise identical conditions and subtracted from the previously obtained TOF profile. Further data processing was performed by a personal computer.

6.2. *Experimental results*

6.2.1. *Doppler spectra*

Figure 12 shows the 0–0 and the 1–1 bands of the CO(B ← X) transition after normalization with respect to the laser power. Both bands consist of a very intense Q branch only. O and S branches were observed as well, but with very weak intensities, while P and R branches are absent for two-proton Σ–Σ transitions [229–230]. Owing to the very small difference for the rotational constants $B' = 1{\cdot}912\ cm^{-1}$ of the B state and $B'' = 1{\cdot}9313\ cm^{-1}$ of the ground state, intense blue-shaded bandheads are observed. No signal in the wavelength range of the 2–2 band was observed, neither for

Table 8. Quantum numbers and wavelength positions for the six transitions that have been studied by the time of flight measurements.

Profile	Wavelength (nm)	v	J
1	230·049	0	0
2	229·981	0	31
3	229·826	0	61
4	230·208	1	14
5	230·167	1	34
6	230·137	1	44

CO^+ nor for any one of the possible ionic fragments O^+ or C^+. However, due to the predissociation of the B state of CO for $v \geqslant 2$, product generation in higher vibrational states cannot be ruled out. It can easily be seen from figure 12 that already the 1–1 band is affected by predissociation: rotational lines overlap due to their short lifetime broadening, and around $J' = 18$ an additional perturbation causes an irregular intensity distribution.

The spectra of figure 12 were recorded using linearly polarized laser light. Rotating the plane of polarization by 90° with respect to the spectrometer axis did not result in changes of intensities or shapes of single lines or the entire spectrum.

Both vibrational bands exhibit a strong rotational excitation up to $J = 64$ for $v = 0$ and $J = 55$ for $v = 1$. Since parent molecule rotation is largely suppressed by the supersonic expansion, the angular momentum of the CO product must be generated in the dissociation process. Higher rotational states ($J \geqslant 30$) of the 0–0 band have separated Doppler broadened lines with a width significantly broader than the laser linewidth of 0·2 cm^{-1}, and serve therefore as an independent test for the correctness of the kinetic energy distributions obtained from the TOF profiles.

TOF profiles were obtained at different wavelength positions (marked by arrows in figure 12 and listed in table 8) in both the acceleration and the drift modes. Thus, (v, J)-state selective kinetic energy distributions of the recoiling CO product were obtained.

The 0–0 band additionally exhibits a very intense ion signal for low rotational levels at the bandhead. The intensity of these overlapping lines ($J = 0, 1, 2$) are well described by a Boltzmann distribution with a temperature parameter of 15 K. The good agreement of this simulation with the experimental data indicates that this part of the spectrum is not due to nascent CO products from the photolysis of phosgene but due to CO impurities that were cooled to 15 K in the supersonic expansion. Therefore, this part of the spectrum serves as a 'thermometer', to determine the initial temperature of the phosgene parent prior to dissociation.

6.2.2. *Rotational populations*

The molecular constants of the X and B states of CO are sufficiently well-known to calculate the line positions of the rotational transitions in the 0–0 and the 1–1 bands and to simulate the spectra. The spectra width of the rotational lines, due to Doppler broadening and laser linewidth, can be determined from the separated high J lines. If this width is considered to be essentially constant for all J, which in good approximation is the case, then the amplitude of every transition is a measure of the integrated line intensity, which in turn is proportional to the $(2J+1)$-fold degeneracy of the lower populated state [230, 231].

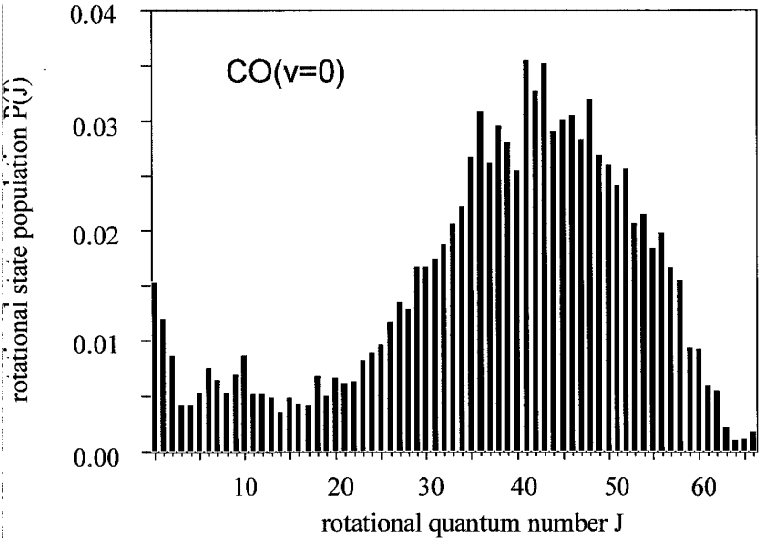

Figure 13. Rotational state population of CO in $v = 0$ from the photodissociation of phosgene as analysed from the spectrum in figure 12. The distribution is neither thermal nor statistical.

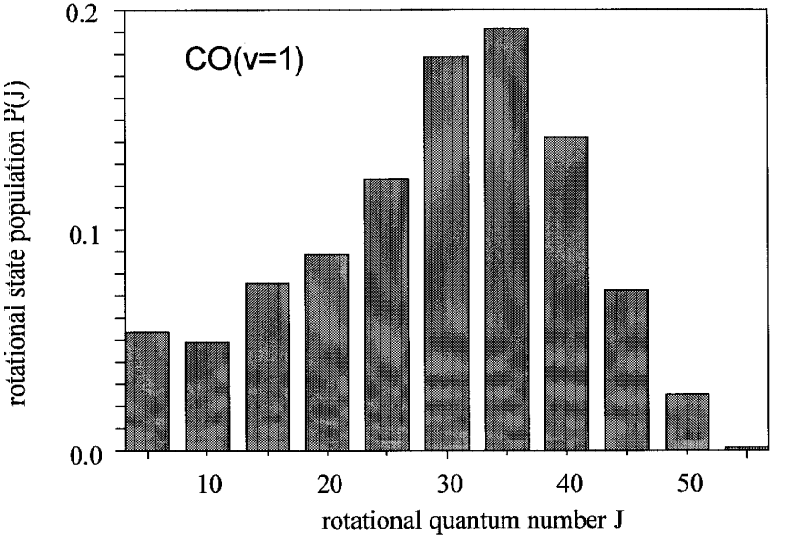

Figure 14. Rotational state population of CO in $v = 1$ from the photodissociation of phosgene. Due to the rotational overlap intervals containing five rotational states have each been evaluated rather than single rotational states.

A sum of Gaussian functions $I(v)$ with centres $v_0(J)$ and a common width Δv was fitted to the observed spectrum of the 0–0 band:

$$I(v) = \sum_J A(J) \exp\left[-\frac{(v - v_0(J))^2}{2\Delta v^2}\right], \tag{83}$$

where the amplitudes $A(J)$ describe the intensities of the transitions. The approximation of the lineshapes by Gaussian functions is justified, since the TOF data

yield a broad kinetic energy distribution, which, although not Boltzmann, give rise to almost Gaussian Doppler lineshapes. The population of the rotational states for $v'' = 0$ is shown in figure 13. The distribution peaks at $J = 43$ and it can neither be characterized by a temperature nor by a statistical model. The mean rotational excitation is 3240 cm^{-1}, which is proof of the dynamic generation of angular momentum in the dissociation process.

The procedure was modified for determining the rotational population of the 1–1 band, because the rotational lines are not separated from each other and their width is unknown. In the analysis of the spectrum we considered the intensities of intervals containing 5 rotational levels each and compared the intensities of those intervals to each other. Using this approach we obtained the rotational population for $v'' = 1$ shown in figure 14, which is similar to the one for $v'' = 0$. The maximum is found around $J'' = 37$, and the mean rotational energy is 1650 cm^{-1}. This shift to lower energies amounts to 73% of the vibrational energy.

6.2.3. *Time of flight profiles*

The acceleration TOF profiles that were observed for the marked positions of figure 12 are shown in figures 15 and 16. With the exception of profile 1, which was recorded at the bandhead of the 0–0 band, all profiles exhibit two characteristic maxima, which are caused by forward and backward flying particles in conjunction with ion fly-out (particles that miss the detector due to high velocity components perpendicular to the spectrometer axis). The presence of ion fly-out is proved by the lower ion intensities at the centres of the TOF in comparison to the wings and implies the generation of fragment velocities higher than the ratio of the TOF t_0 from the ionization spot to the detector and the detector radius r_D, which in our case (t_0 = 20 μs, r_D = 2 cm) amounts to 1000 m s^{-1}. The fragments missing due to fly-out are accounted for in the data analysis procedure presented below, which has been previously outlined in more detail [184, 208].

Profile 1 proves the previously postulated CO impurity. The width of the profile of 25 ns corresponds to the duration of the laser pulse and can therefore be evaluated in order to obtain an upper limit for the particle velocity. Employing equation (82) one obtains the upper limit to be as low as 100 m s^{-1}. This low velocity cannot be caused in the dissociation process, but corresponds to a mean particle velocity of CO at a temperature of 13 K, a value that agrees closely with the rotational temperature from the simulation of the strong 0–0 bandhead signal. However, a more detailed analysis of the profile yields a very small fraction of fast CO fragments, which manifest themselves in the tails of the profile that only slowly approaches the baseline for large deviations Δt from the centre t_0 of the profile. While this fraction cannot be analysed quantitatively in the acceleration mode due to the much larger number of slow particles, this will be possible in the drift mode, since the numerous slow jet-cooled particles that dominate the signal in the acceleration mode miss the detector due to the collective velocity of the molecular beam. However in this case it is not possible to make use of the complementary sensitivities of the two modes for high and low energy particles, and one is left with the observation of the high energy particles only.

The remaining five acceleration TOF profiles have two additional features to be considered. First, for increasing rotational and vibrational excitation of the fragments a smaller width of the TOF profiles is found. This observation corresponds to a decreasing kinetic energy content for increasing internal energies of the fragments. This effect is also seen for the Doppler broadening, but is small enough not to affect

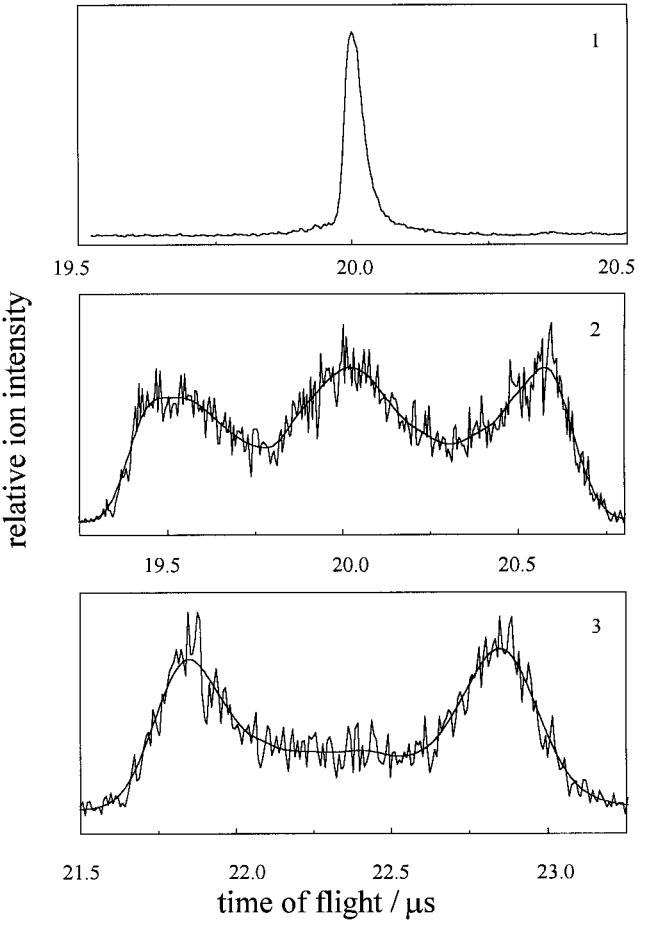

Figure 15. Acceleration time of flight profiles for the three states in $v = 0$. The solid lines in 2 and 3 result from smoothing the raw data. Note the marked difference between profile number 1 and all other observed acceleration time of flight profiles.

the accuracy of the determination of the rotational state population, which assumed a common width for all rotational levels. Second, some profiles have a third maximum at the centre, which gives rise to a bimodal kinetic energy distribution. We very carefully considered any possible explanation that might mark these maxima as artefacts: collisions of the ionized CO with other particles, simultaneous excitation of neighbouring rotational levels with selection of different velocity components along the spectrometer axis, fragmentation of the ionized parent molecular ion, non-resonant ionization of CO, wall collisions of the ionized CO, and clustering of phosgene in the supersonic expansion. Each of these hypotheses results in different experimentally observable effects on the shape of the TOF profiles and can be investigated by changing the experimental parameters, as there are the stagnation pressure of phosgene prior to the expansion, laser intensity and wavelength. For none of these parameters were the expected variations in the shape of the TOF profile observed. Moreover, it is not plausible that only some rotational levels should be affected in the present experiments which were conducted under identical conditions for all rotational levels investigated. Therefore, being forced to reject all of the

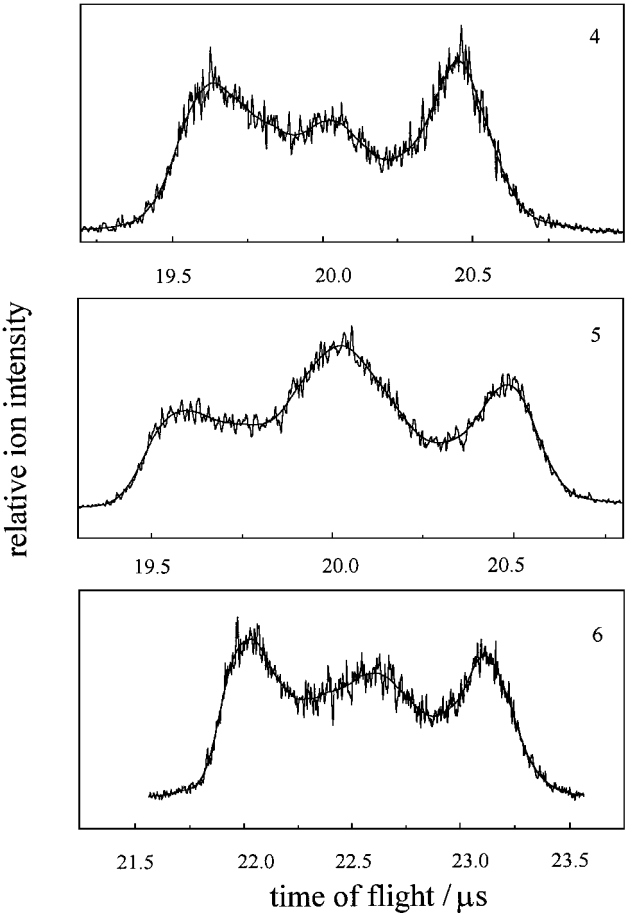

Figure 16. Acceleration TOF profiles corresponding to figure 15 for $v = 1$.

arguments discussed above the third maxima are characteristic for the dynamics of the decay process, and the corresponding bimodalities are real.

Some of the corresponding drift TOF profiles are shown in figure 17 after background correction. Here, the profile 1 observed at the 0–0 bandhead is not qualitatively different from the other profiles, as was the case for the acceleration data. The reason is that the large number of cold CO molecules that were responsible for the differences in the acceleration profiles do not impinge on the detector due to their low velocities and the comparatively high collective velocity of the molecular beam perpendicular to the spectrometer axis.

6.2.4. *Kinetic energy distributions*

The independence of the shapes of the TOF and the Doppler profiles of the polarization direction of the laser indicates an isotropic fragment distribution. Since the excited $^1A_2$ state of phosgene is not repulsive, possible pathways to dissociation are either internal conversion in high vibrationally excited levels of the electronic ground state or vibronic predissociation via the $^1B_2$ state [208]. Both pathways are slow and involve an internal energy redistribution which requires a long time when compared to

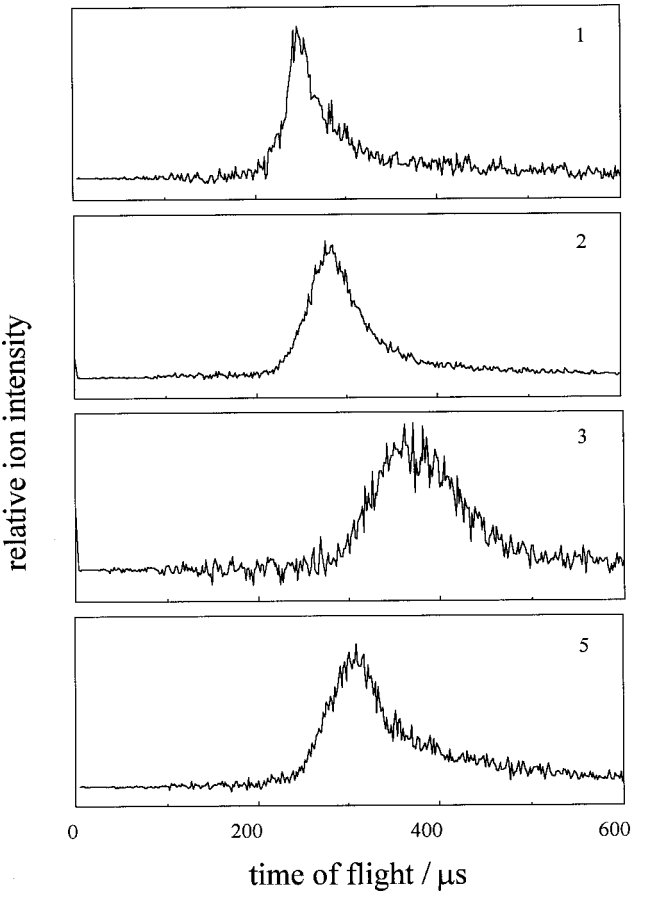

Figure 17. Drift TOF profiles for three states in $v = 0$ and one state in $v = 1$.

a direct fragmentation mechanism on a time-scale of some 10 fs. During this time the original alignment of the parent molecule that has been induced by the absorption of linearly polarized light is lost due to the rotational excitation remaining in the parent molecule after the supersonic expansion. The time period for a full rotation of the phosgene parent about one of its principal axes of inertia is estimated to be approximately 50 ps, taking into consideration a remaining thermal energy corresponding to 15 k. This is also the lower limit for the lifetime of the excited phosgene molecule.

The data evaluation procedure for obtaining kinetic energy distributions from the combined acceleration and drift TOF profiles makes implicit use of the isotropic fragment distribution [184]. In the absence of ion fly-out for the acceleration measurements, due to the linear relationship (82) between the measured quantity, the flight time deviation Δt from the centre of the TOF profile t_0, and the velocity component v_x along the spectrometer axis, the TOF data evaluation procedure is identical to the evaluation procedure for Doppler profiles, with Δt replacing Δv, the Doppler shift, and t_0 replacing v_0, the line centre. In particular, an isotropic single-valued velocity distribution yields a rectangular profile and a Boltzmannian distribution manifests itself in a Gaussian TOF profile. While for the given geometry no laboratory to centre of mass transformation is required, ion fly-out must, however,

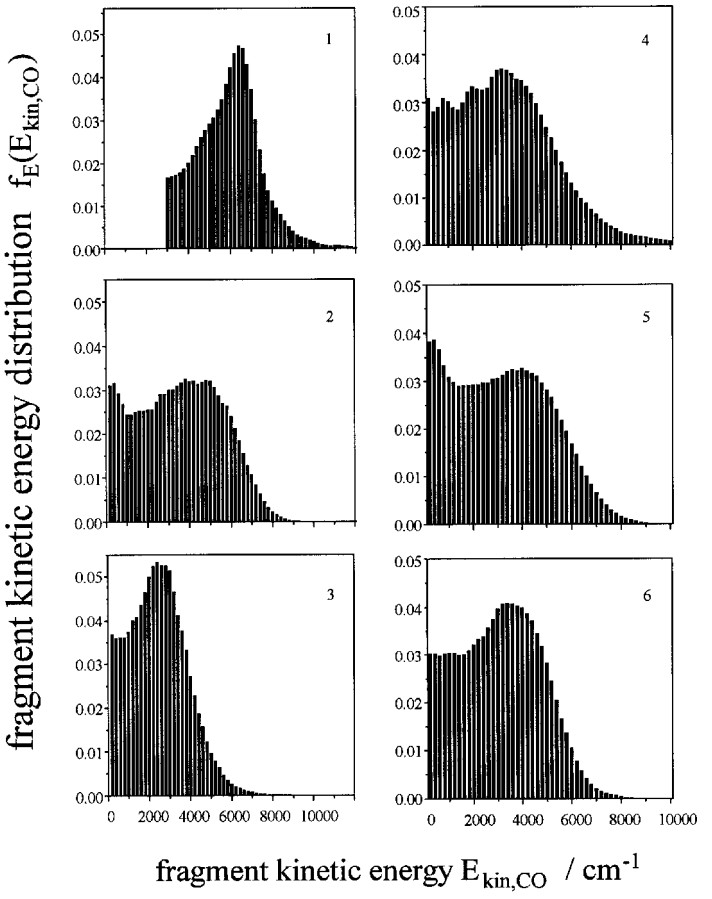

Figure 18. Complete kinetic energy distributions for all investigated states from the analysis of the combined acceleration and drift TOF data, as described in the text. The *y* axis is scaled with respect to the abundance of CO molecules in kinetic energy intervals of 200 cm^{-1} width. For state 1 only the drift data have been observed. Therefore, kinetic energy values below 3000 cm^{-1} cannot be shown.

be accounted for, which can best be done by an iterative procedure as previously described [184, 208]. In contrast, for the drift measurements the laboratory to centre of mass transformation is essential. In short, the procedure followed here was to first convert the drift data to highly accurate velocity distributions which are characteristic of the high energy particles, but lack information about slow particles. Second, the iteration procedure yielded complete velocity distributions from the acceleration data with a lower degree of accuracy, which were subsequently adjusted within the experimental error (mainly resulting from the finite duration of the laser pulse) to match the drift data. Finally, the accurate and complete velocity distributions were converted to the desired kinetic energy distributions.

Following this procedure, the kinetic energy distributions of figure 18 were obtained. For profile 1, where the low energy fragments could not be observed due to the dominance of the jet-cooled CO impurity, only the drift data were evaluated. Therefore, only kinetic energy values above 3000 cm^{-1} appear in the kinetic energy spectrum.

Table 9. Quantum state specific energy forms and contents for all investigated states from table 6. J and v are the rotational and the vibrational quantum numbers, respectively, E_{rot} and E_{vib} the corresponding internal energies. $\bar{E}_{kin,\,CO}$ is the average value for the CO fragment distributions of figure 18. $\bar{E}_{kin,\,Cl}$, the quantum state specific mean kinetic energy of the Cl atoms, was calculated from the difference of the available energy and the sum of all other energies, based on the generation of two ground state chlorine atoms. The f values accounts for the relative participation of the respective energy form in the energy partitioning.

Profile	J	v	E_{rot}	E_{vib}	$\bar{E}_{kin,\,CO}$	$\bar{E}_{kin,\,Cl}$	$\bar{E}_{kin,\,tot}$	f_{rot}	f_{vib}	f_{kin}
1	0	0	0	0	(5740)	(4520)	14780	0·00	0·00	1·00
2	31	0	1910	0	3450	4710	12870	0·13	0·00	0·87
3	61	0	7300	0	2350	2565	7480	0·49	0·00	0·51
4	14	1	420	2170	3390	4400	12190	0·03	0·15	0·82
5	34	1	2370	2170	3100	3570	10240	0·16	0·15	0·69
6	44	1	3930	2170	2960	2860	8680	0·27	0·15	0·58

The transformation of the TOF profiles in kinetic energy distributions leads to a much higher density of data points for low energies as compared to higher energies. In order to avoid a higher weight of the low energy amplitudes in the fit procedure, we calculated mean values for a standard size interval of fragment kinetic energy, before actually performing the fits. The size of these intervals has been chosen small enough to keep sufficiently many data points for the fit procedure, i.e. significantly more than adjustable parameters, but not smaller than the kinetic energy resolution of the apparatus, which in the investigated energy range was of the order of 200 cm^{-1}.

The data extracted from the fragment energy distribution are compiled in table 9. For each investigated state the mean kinetic energy has been determined. For CO in $v = 0$. $J = 0$ the contribution of slow molecules was assumed to be constant below 3000 cm^{-1}. The resulting speculative character of the obtained value of the mean kinetic energy for this state is marked by parentheses in table 9. High internal CO excitation coincides plausibly with low CO kinetic energy contents. Correspondingly a broad range for the respective mean kinetic energies of the Cl partner fragments must be observed. These were calculated from the energy amount by which the total available energy exceeds the sum of the CO energies in all degrees of freedom, based on the assumption that two ground state chlorine atoms with equal mean kinetic energies will be produced.

6.3. *Fragmentation channels*

For each one of the six kinetic energy distributions an individual fit was performed for the parameter values that characterize decay channels (equation (81)). First, we tried to achieve a satisfactory agreement by considering single mechanisms only. The agreement of the results of these attempts with the experimentally derived distributions is in general poor. Only for the asynchronous concerted case could a qualitatively satisfactory agreement be achieved, in that a bimodality can be simulated, but neither the positions nor the widths of the two maxima are produced correctly. Therefore, it seems most likely that competing mechanisms operate, as will be discussed below in further detail.

The contribution of more than one dissociation channel was accounted for using equation (79), fitting the respective parameters and amplitudes. We present the results of this fit procedure for CO ($v = 1$) in figure 19, while all results are compiled in table

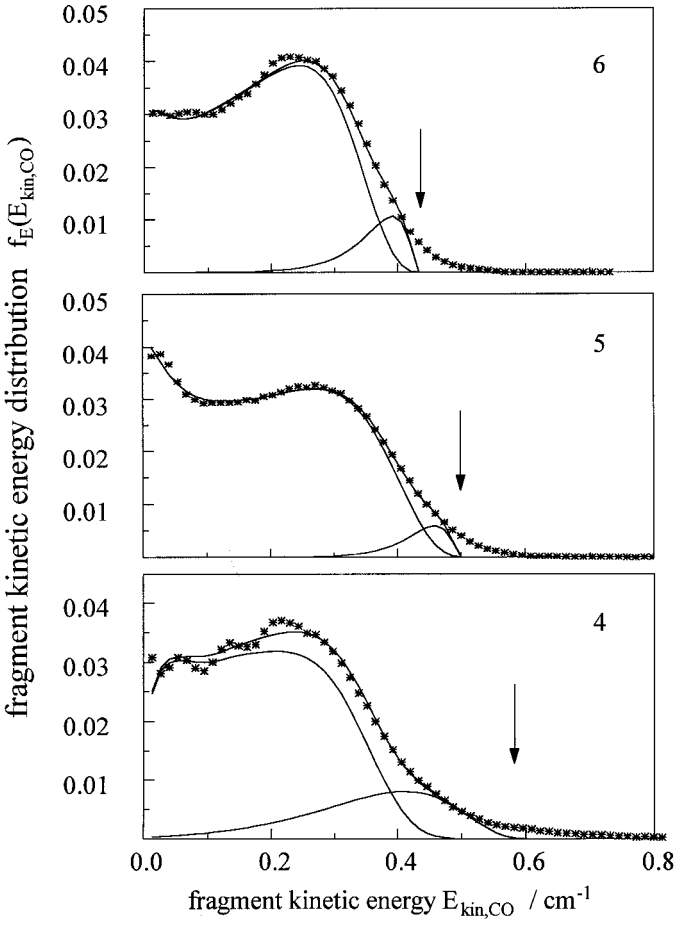

Figure 19. Fit of the decay models (solid lines) to the experimentally observed data (asterisks). The contributions of the synchronous and asynchronous concerted mechanisms and the sum of both are shown together in one graph for each state. The contribution of the synchronous mechanism are the high energy distributions for all states shown. The arrows mark the limiting energy that separates the three body from the molecular decay channel. The contribution of the molecular channel is insignificant.

10. Experimental data are shown as asterisks and the contributions of each decay channel as well as the sum of all contributions as solid lines. The agreement between the calculated data and the experiment is very good qualitatively as well as quantitatively, if competing pathways are considered. A minor discrepancy remains in the high energy part of the spectrum and is due to the resolution of our apparatus and to the neglect of the insignificant contribution of the molecular channel.

6.3.1. *The principal channel: asynchronous mechanism*

One can draw some important conclusions about the decay mechanism from a qualitative discussion of the kinetic energy distributions displayed in figure 18. The dominating features are two maxima: a weakly pronounced maximum at very low energies and a more strongly pronounced maximum at higher energies that reaches to the limiting energy which indicates the onset of the molecular regime. The distributions resemble those previously presented simulated kinetic energy distributions with a

narrow distribution of the energy deposition E_{AB} (here: E_{COCl}) and a broad distribution of the decay angle θ. The double maximum is due to the narrow energy deposition distribution, since a broader distribution allows the corresponding kinetic energy distribution to appear increasingly unstructured. The dominating high energy peak is evidence of the CO molecule being principally forward scattered, whereas the more weakly pronounced low energy maximum proves a non-negligible participation of backward scattered CO fragments also. From these considerations we expect a broad distribution of the decay angle θ around a value of 180°. The angle θ is defined with respect to the direction of motion of the second chlorine atom rather than the direction of the CO fragment, with the meaning of backward and forward scattering being reversed.

The quantitative analysis of the kinetic fragment energy distributions yields a principal contribution of the asynchronous concerted channel with the parameter values listed in table 10, which agree closely with the qualitative considerations in the preceding paragraph. Accordingly the contribution of the asynchronous concerted channels accounts for approximately 80% of all decay processes, with a standard deviation of 20%. No tendency for a change of this value is found for changes in the internal excitation of the CO fragments. The intermediate COCl particle, which exists only in the very short period between the first and the second C–Cl bond cleavages, carries on average 10% more of the total available energy E_{av} as internal excitation than is eventually found as internal energy of the CO product. The kinetic energy release in the second step is therefore small and does not significantly influence the kinetic energies of the final fragments. Due to the forward scattering the CO increases its kinetic energy by a small amount, whereas the kinetic energy of the chlorine atom from the second decay step is accordingly decreased. Owing to its large mass, the velocity of the COCl intermediate is always small, too, so that a large fraction of slow chlorine atoms is expected from the CO kinetic energy data. However, the decay angle distribution is very broad and, thus the opposite case, forward scattered chlorine atoms and backward scattered CO molecules, contributes to a non-negligible extent, giving rise to the low energy maximum in the CO fragment kinetic energy distribution. This interpretation also supplies a physically meaningful and plausible explanation for the previously discussed third maxima observed in the acceleration TOF data.

The parameter distributions for the asynchronous concerted decay channel are depicted in figure 20 for the CO state with $v = 0$, $J = 61$. The width of the decay angle distribution calls for some reflection on the distinction between the sequential and the asynchronous concerted decay mechanisms. Although every possible decay angle is realized in the phosgene dissociation, including those where the two decay steps are independent of each other, we will not consider the process to proceed sequentially. The reason is that there are different weights for every decay angle. Accordingly the independence criterion is not fulfilled for all decay processes, but only for selected ones, which is insufficient in order to call the process sequential.

While no information on the lifetime of the excited phosgene parent molecule is available from the parameter values (although we have discussed this issue before in the context of the isotropy of the dissociation process) it is obvious that the lifetime of the COCl intermediate cannot exceed its mean rotational period, since otherwise the decay angle θ would be equally distributed and the process would be sequential. Therefore, an upper limit for the COCl lifetime is obtained from comparison with its rotational period. Since there is no information obtained on the angular momentum of the COCl radical or its geometry, we rather crudely approximated a value of

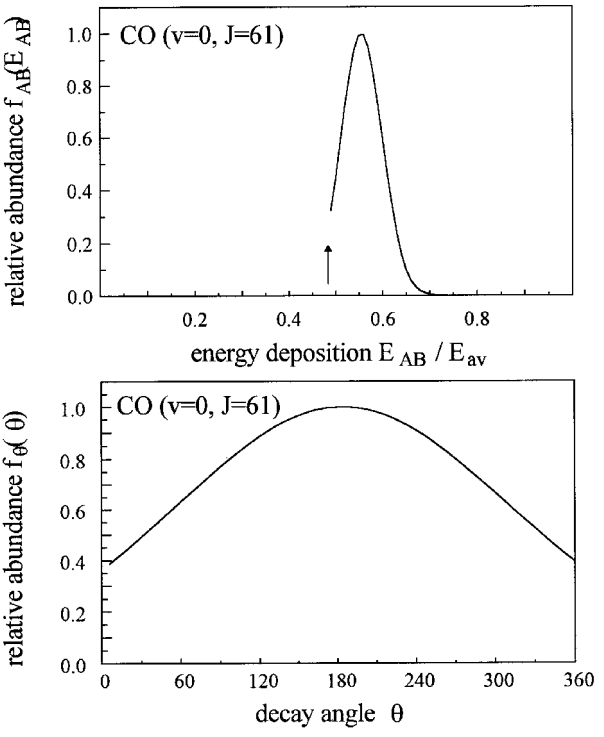

Figure 20. Parameter distribution of the energy deposition and the decay angle, obtained from the fit procedure for the CO state with $J = 61$ and $v = 0$. Note the very broad angular distribution and the narrow distribution for the energy deposition centred at values only slightly above the CO internal excitation, which is denoted by arrows.

τ_{COCl} = 50 ps for low rotational excitation ($J = 1$) and a linear geometry. This value is based on an estimated moment of inertia of 8×10^{-41} kg m^{-2}. Taking into account the non-planar conformation of phosgene in the excited $^1A_2$ state, the small rotational constants of COCl and $COCl_2$ and the high rotational excitation of the CO fragments, we are convinced that the actual angular momenta are much higher and a lifetime τ_{COCl} in the order of 1 ps seems to be a more realistic value.

6.3.2. *The secondary channel: synchronous mechanism*

The main features of the kinetic energy distributions are well reproduced by the asynchronous concerted mechanism as discussed in the previous section. For high kinetic energies just below the limiting energy to the molecular regime, however, a satisfactory agreement is not achieved. This energy range can be much better described by contributions from the synchronous mechanism. A moderate excitation of the Cl–C–Cl bending mode is sufficient in order to close the gap between the calculated distribution on the basis of solely the asynchronous concerted mechanism and the experimental data. The reason is that, due to the projection of the chlorine atom velocities on the axis of motion of the CO fragment, large changes in the (small) bond angle correspond to only minor changes in the (high) CO fragment recoil velocities.

The participation of the synchronous channel is 17% on average with a standard deviation of 13%. The exact values are again listed in table 10. The mean bond angle of the excited phosgene molecule at the decay time is 107°. This value is very close to the 111° Cl–C–Cl bond angle of the excited phosgene, which is exactly the same as the

Table 10. Results from the fit procedures simulating the kinetic energy distribution for the transitions 1–6. The amplitudes A contain the contributions of the respective mechanisms in the overall decay process, $E_{int,\,CO}$ is the internal energy of the observed CO state, $E_{AB,\,0}$ and ΔE_{AB} are the parameters describing the distribution of the energy deposition for the sequential and the asynchronous concerted mechanisms, θ_0 and $\Delta\theta$ describe the decay angle distribution for the asynchronous concerted mechanism, and α_0 and $\Delta\alpha$ describe the bond angle distribution for the synchronous concerted mechanism. All energies are given in units of the available energy E_{av}, all angles in degrees, the distribution widths are 1σ. Additionally the difference between the centre of the energy deposition distribution $E_{AB,\,0}$ and the internal energy $E_{int,\,CO}$ of the CO fragment are indicated, and also, where applicable, the respective mean values averaged over the observed quantum states. If the average values are mechanism specific, they have been weighted with the respective amplitudes A.

	1	2	3	4	5	6	Mean
$E_{int,\,CO}$	0·00	0·13	0·49	0·20	0·31	0·41	
A^{conc}	64%	95%	62%	81%	94%	89%	81%
A^{syn}	35%	5%	35%	17%	4%	8%	17%
A^{mol}	< 1%	0%	< 3%	< 2%	< 2%	< 3%	< 2%
$E_{AB,\,0}$	0·19	0·27	0·56	0·22	0·47	0·56	
ΔE_{AB}	0·05	0·13	0·06	0·10	0·15	0·13	0·10
$E_{AB,\,0} - E_{int,\,CO}$	0·19	0·14	0·07	0·02	0·16	0·15	0·12
θ_0	180°	190°	184°	182°	182°	187°	184°
$\Delta\theta$	130°	190°	183°	231°	215°	160°	187°
α_0	115°	98°	111°	112°	67°	68°	109°
$\Delta\alpha$	31°	29°	37°	30°	32°	34°	34°

value for the ground state [199]. This is a common feature for this class of molecule, and is also known for formaldehyde (H_2CO) [232] and thiophosgene ($CSCl_2$) [233]. The width of the bond angle distribution is 33° on average and accounts for a significant excitation of the ν_3 Cl–C–Cl bending mode. We did not attempt to quantitatively determine this excitation, since the potential energy surface for this mode is unknown and the harmonic oscillator approximation is inappropriate for this large excitation. That the excitation is indeed large can be seen from the comparison with the zero point amplitude which we estimated to be 5°, approximating the bending vibration by a linear oscillation of the two Cl atoms with the force constant of the bending mode.

6.3.3. *The negligible channel: molecular decay*

The additional energy from the bond energy of the chlorine molecule makes the molecular decay channel special, in that the CO fragments must possess a higher kinetic energy than the CO products generated by mechanisms producing two chlorine atoms:

$$E_{kin,\,CO}^{mol} = \frac{m_{Cl_2}}{m_{COCl_2}}(E_{av} + E_{diss,\,Cl_2} - E_{int,\,Cl_2} - E_{int,\,CO}). \tag{84}$$

The expression $E_{diss,\,Cl_2} - E_{int,\,Cl_2}$ is always greater than zero, because otherwise the chlorine molecule would dissociate into two separated atoms. The limiting kinetic energy for the molecular channel is therefore given by

$$E_{kin,\,CO}^{limit} = \frac{m_{Cl_2}}{m_{COCl_2}}(E_{av} - E_{int,\,CO}). \tag{85}$$

This limiting energy depends on the internal excitation of the observed CO fragment and separates the molecular regime from the three body regime. In figure 19 it is marked by arrows. Kinetic energies higher than the limiting energy, i.e. on the right side of the arrow, correspond to the molecular channel. In no case did the integration of the experimental data in the corresponding high energy parts of the observed kinetic energy distributions yield a contribution of more than 3% for the molecular decay. The detailed data can be found in table 10.

We believe, however, that the molecular channel does not contribute at all to the overall decay, and that the amplitudes should better be regarded as upper limits for the following reasons. First, the resolution of $\sim 5\%$ of our apparatus has not explicitly been taken into account by a deconvolution procedure for the experimental data. A respective forward convolution of the calculated kinetic energy distributions correspondingly leads to kinetic energy values above the limiting energy, which is exactly the observed effect, without implying the generation of a chlorine molecule. Second, the energetic range of the molecular regime, where we observed non-zero values, is very narrow compared to the dissociation energy of the chlorine molecule: $E_{\mathrm{diss,\ Cl_2}} = 20\,000\ \mathrm{cm}^{-1}$. If the participation of the molecular channel were real, this would mean that very high internally excited chlorine molecules would be produced exclusively, with the internal excitation close to the dissociation limit, a scenario which is very unlikely.

In conclusion, the total decay process can be characterized as being contributed to by two competing mechanisms. The principal mechanism is the asynchronous concerted three body decay and occurs approximately five times as often as the secondary mechanism, the synchronous three body decay. The characteristic features of the synchronous channel is a decay via the equilibrium configuration of the excited state with a significant excitation of the ν_3 bending model, while the asynchronous mechanism produces mostly forward scattered CO molecules after only little excitation of the COCl intermediate. The COCl lifetime should be of the order of 1 ps.

6.4. *Angular momentum analysis*

In numerous cases the angular momentum analysis yields detailed insight into the mechanism of a chemical reaction. If the angular momentum prior to the reason is known, then by monitoring the rotational state populations of the reaction products one can obtain information about the orbital angular momentum of the system after the reaction has taken place, which in turn allows the impact parameter to be determined, since the sum of the rotational and the orbital angular momenta of the products has to be equal to the initial angular momentum of the reactants.

If a reaction produces more than two fragments, then, in general, the angular momentum analysis is not as powerful as compared with the two product case, due to the underdetermined kinetic equations. Moreover, the concept of orbital angular momentum is not applicable in those cases where no preferred direction of motion exists. In most cases only statements concerning upper and lower limits of angular momenta can be made. For the three body decay of phosgene different rotational states might be populated by identical decay parameters, depending on the values for the C=O bond length $r_{C=O}$, the Cl–C–Cl bond angle α and the out-of-plane angle β.

Nevertheless, the photodissociation of phosgene is a system where the angular momentum analysis allows more than simply proving the absence of contradictions between the experimentally observed data and the conclusions drawn. First, the two

atomic fragments carry a negligible amount of angular momentum in comparison to the CO rotational excitation. Second, at least for the synchronous mechanism, the orbital angular momentum is unambiguously defined, since the direction of motion of the CO fragment is a reference axis for all produced fragments. In this favourable case the conservation of angular momentum can be written as

$$\mathbf{J}_{COCl_2} = \mathbf{J}_{CO} + \mathbf{J}_{Cl}^{(1)} + \mathbf{J}_{Cl}^{(2)} + \mathbf{L}, \tag{86}$$

where $\mathbf{J}_{COCl_2}$ describes the rotational excitation of the phosgene parent prior to dissociation, $\mathbf{J}_{CO}$, $\mathbf{J}_{Cl}^{(1)}$ and $\mathbf{J}_{Cl}^{(2)}$ describe the product rotational angular momenta, and $\mathbf{L}$ denotes the orbital angular momentum with respect to the motion axis of the CO molecule. The angular momenta of the chlorine fragments as well as the initial angular momentum of the parent are small, the first because of the atomic nature of the fragments, the second because of the rotational cooling in the supersonic expansion. Therefore, to a good approximation the following relationship holds:

$$\mathbf{J}_{CO} + \mathbf{L} \approx \mathbf{O} \quad \text{resp.} \quad J_{CO} = |\mathbf{J}_{CO}| \approx |\mathbf{L}| = L. \tag{87}$$

Since J_{CO} is an observable quantity, L is easily determined, and from the knowledge of the orbital angular momentum of the system one obtains restrictions for the molecular geometry at the decay time with respect to the above-mentioned quantities $r_{C=O}$, α and β. In order to evaluate these restrictions, one needs to take a closer look at the orbital angular momentum of the phosgene system.

The orbital angular momentum of a two body system is in general defined as

$$L = \mu v b, \tag{88}$$

where μ is the reduced mass, v the relative fragment velocity and b the impact parameter of the system. If only the synchronous three body decay is taken into consideration, the respective quantities have simply to be defined with respect to the symmetry axis of the molecule, which is at the same time the direction of motion of the CO fragment. This procedure results in taking into account only those components of the Cl fragment velocities that are parallel to the CO axis of motion. Subsequently we will discuss in more detail the quantities in equation (88).

The reduced mass μ is given by considering the corresponding two body decay into a CO molecule and a Cl_2 'quasi' molecule:

$$\mu = \frac{2 m_{Cl}\, m_{CO}}{m_{COCl_2}} = 20 \text{ amu}. \tag{89}$$

The relative fragment velocity is obtained from summing up the absolute value v_{CO} of the CO fragment velocity and the Cl fragment velocity component v_{Cl} along the CO axis of motion:

$$v = v_{CO} + v_{Cl} = v_{CO}\left(1 + \frac{m_{CO}}{2 m_{Cl}}\right). \tag{90}$$

The impact parameter b is the projection of the distance between the carbon atom and the centre of mass of the CO molecule. For the synchronous decay it is only

different from zero if the molecular geometry becomes non-planar. Then the impact parameter depends in the following way on the out-of-plane angle β:

$$b = r_{C=O} \frac{m_O}{m_{CO}} \sin \beta, \tag{91}$$

where $r_{C=O}$ is the length of the C=O bond and m_O and m_{CO} are the masses of the oxygen atom and the CO molecule, respectively. Note that for $\beta = 0$, describing a planar molecule, the impact parameter vanishes in agreement with the preceding paragraph.

Combining equations (89)–(91) one obtains the following expression for the orbital angular momentum L:

$$L = \frac{2m_{Cl}\, m_O}{m_{COCl_2}} \left(1 + \frac{m_{CO}}{2m_{Cl}}\right) v_{CO}\, r_{C=O} \sin \beta. \tag{92}$$

For the synchronous decay the orbital angular momentum is therefore unambiguously determined by the geometry and the energetics of the system. The number n of angular momentum quanta is given by

$$n = \frac{L}{\hbar} = \frac{2m_{Cl}\, m_{CO}}{\hbar m_{COCl_2}} \left(1 + \frac{m_{CO}}{2m_{Cl}}\right) v_{CO}\, r_{C=O} \sin \beta. \tag{93}$$

Thus, it is possible to draw conclusions on the parent molecule geometry from the observation of angular momenta as well as to predict the rotational excitation of the CO fragment from a given decay geometry.

The most critical relationship exists between n and the value of β. Varying β from 0° to 90° realizes all possible values for n between zero and the maximum value, which is determined by the CO fragment velocity and the C=O bond length. Moreover, the velocity v_{CO} as an important observable quantity can assume values in the broad range between 0 m s^{-1} and 3000 m s^{-1}. However, for the latter one has to take into account the conservation of energy that is not given credit in equation (93), and that does not permit the realization of large velocities of e.g. 3000 m s^{-1} and the corresponding maximum angular momentum of 100 $\hbar$ at the same time. For determining the possible CO fragment velocities the CO rotational energy has to be considered according to

$$0 \leqslant v_{CO} \leqslant v_{CO}^{max} = 2\left[\frac{m_{Cl}}{m_{COCl_2} m_{CO}} (E_{av} - E_{int,\,CO})\right]^{1/2}. \tag{94}$$

The largest observed rotational excitation of the CO fragment is $J_{CO} = 64$. For the rotational state with $J_{CO} = 61$, that has been investigated in detail in our experiments, 49% of the available energy E_{av} is trapped as internal rotational energy $E_{int,\,CO}$ in the CO fragment (cf. table 11), so that only the remaining 51% of the available energy can be distributed onto the total kinetic energies of all products. According to the parameter distributions derived for the synchronous decay, 22% of the available energy is found as kinetic energy in the CO fragments, corresponding to a mean velocity of $v_{CO} = 1600$ m s^{-1} for the CO fragment. This velocity induces an excitation of the CO fragment of 54 quanta for the maximum out-of-plane angle $\beta = 90°$. This is in good agreement with the experimentally observed value of 61 quanta, when the thermal parent molecule rotational excitation and the angular momenta of the

Table 11. Mean kinetics energies of CO and Cl fragments for the synchronous and the asynchronous concerted decay mechanisms. The values were derived from the weighted averages of the respective contributions to the overall decay for all profiles investigated, as depicted in figure 19 for profiles 4–6, based on the production of two ground state chlorine atoms. The values in column 1 are in parentheses because the low energy component for CO ($v = 0$, $J = 0$), could not be observed, and have not been considered in obtaining the mean values. The sum of each column is 1 for every mechanism. One has to remember that two identical chlorine atoms are generated in the synchronous mechanism. All energies are given in units of E_{av}. Note the pronounced anticorrelation of $\bar{E}^{conc}_{kin,\,Cl(1)}$ and $E_{int,\,CO}$. Further details are given in the text.

Profile	1	2	3	4	5	6	Mean
		$v = 0$			$v = 1$		
			Asynchronous concerted mechanism				
$E_{int,\,CO}$	0·00	0·13	0·49	0·20	0·31	0·41	
$\bar{E}^{conc}_{kin,\,CO}$	(0·38)	0·24	0·13	0·19	0·20	0·19	0·19
$\bar{E}^{conc}_{kin,\,Cl(1)}$	(0·59)	0·49	0·26	0·45	0·38	0·32	0·38
$\bar{E}^{conc}_{kin,\,Cl(2)}$	(0·03)	0·14	0·12	0·16	0·11	0·08	0·12
			Synchronous mechanism				
$E_{int,\,CO}$	0·00	0·13	0·49	0·20	0·31	0·41	
$\bar{E}^{syn}_{kin,\,CO}$	(0·43)	0·44	0·22	0·36	0·43	0·36	0·36
$\bar{E}^{syn}_{kin,\,Cl}$	(0·29)	0·21	0·14	0·22	0·13	0·11	0·16

chlorine atoms are taken into account, that were neglected in going from equation (86) to equation (87). While these additional angular momenta may also lead to a decrease in the induced CO rotational excitation, this does not contradict our argument. It simply means that those few fragments that are observed in $J_{CO} = 61$ are generated via a strong deviation from a planar geometry, and that the initial angular momentum of the phosgene adds to the dynamically induced rotational angular momentum of the CO fragment.

The previously discussed energy analysis within the frame of our kinematic model cannot yield these conclusions on the out-of-plane angle β, since β does not directly affect the energetics of the process. In the favourable case of phosgene dissociation, however, one obtains as a qualitative result that the ν_4 out-of-plane bending mode is significantly excited. In general, such a conclusion cannot be drawn for any three body decay, which is the reason that the angular momentum analysis has been dealt with in this special section on phosgene dissociation rather than in one of the preceding sections containing more general considerations on three body decays as such.

Another qualitative result of the angular momentum analysis is that either the sequential or the asynchronous concerted mechanism must play a significant role in the overall dissociation process. This can be seen from the existence of very slow CO fragments with a large rotational excitation, since for the synchronous mechanism alone, according to equation (93) small values for v_{CO} also imply small values for n. This result has already been obtained in greater detail directly from analysing the kinetic energy distributions, but it strengthens our confidence that backward scattered CO fragments from the asynchronous decay are generated in the phosgene dissociation.

6.5. *Chlorine fragment energetics*

Knowledge of the parameter distributions for each decay mechanism allows a mechanism specific determination of the mean kinetic energies of the CO molecule. Having experimentally observed the internal CO energy, we were able to determine the

corresponding mean kinetic energies of the chlorine atoms in a mechanism specific manner also. The energies obtained via this approach are compiled in table 11. The basis for the calculation was the generation of two ground state chlorine atoms. Thus, no additional internal energy, apart from the known value for CO, had to be considered. This assumption is justified from the recent results of phosgene photodissociation [184, 207, 208], where the excited spin–orbit state only contributed to less than 5% at 248 nm and to 16% at 235 nm, respectively.

It can be seen from the data in table 11 that the asynchronous concerted mechanism produces one fast and one slow chlorine atom at a time, while the synchronous decay produces two slow atoms. The fast atom resulting from the first bond cleavage in the asynchronous concerted decay carries almost all kinetic energy that is released in the dissociation process. Its velocity therefore depends strongly on the internal excitation of the CO molecule. This dependence is indeed seen in table 11, as is the much weaker dependence of the velocity of the second chlorine atom on the CO internal energy. The generation of two slow chlorine atoms by the synchronous mechanism is also a consequence of associating the fastest CO molecules with this mechanism.

The kinetic energy of the chlorine fragments is therefore contributed to by three qualitatively different channels: (a) the first bond cleavage of the asynchronous concerted mechanism, (b) the second bond cleavage of the asynchronous concerted mechanism, and (c) the synchronous mechanism. Channel (a) induces significantly larger kinetic energies in the corresponding chlorine fragment than the other two channels and should therefore be experimentally distinguishable from those. The energies of the products from channels (b) and (c) are very similar, however, and cannot be expected to be experimentally resolved. From these arguments we expect from the CO experimental data a bimodal kinetic energy distribution for the chlorine fragments, where we estimate for the centres a value of 13% of the total available energy for the slow component and a value of 38% for the fast component. These values are derived from the mean kinetic energies of table 11 after weighting with the contributions of the two considered mechanisms. Consequently, the intensity ratio of the slow to the fast component is given by

$$\frac{A^{\text{conc}} + 2A^{\text{syn}}}{A^{\text{conc}}} = \frac{81 + (2 \times 17)}{81} = 1{\cdot}4. \tag{95}$$

Indeed, in a previous study on the chlorine atom kinetics from the photodissociation of phosgene at 235 nm we have observed a bimodal kinetic energy distribution [208]. While the qualitative agreement with the predictions from the CO data analysis is good, the intensity ratio of 3 : 1 and the mean kinetic energy values of 7% and 29% of the total available energy are different and do not lie within the experimental error of the CO data analysis.

This quantitative discrepancy can be explained by the generation of highly vibrationally excited CO molecules ($\nu_{CO} \geqslant 2$), which are not experimentally observable with the detection scheme employed in our experiments due to the predissociation of the intermediate resonant $B^2\Sigma^+$ state. The main argument favouring this explanation is the smaller values for the chlorine atom kinetic energies as compared to the expectations. It must be remembered in this context that a higher internal excitation of the CO molecule takes the energy mainly from the fast chlorine atom and, to a lesser degree only, from the slow atom. The difference in the intensity ratios suggests a higher

contribution of the synchronous channel for highly vibrationally excited CO fragments, favouring the generation of only slow Cl atoms.

Based on our experimentally observed kinetic energy distributions of the chlorine atoms an information theoretic analysis of the underlying decay mechanism has been performed [71], similar to the analysis of the acetone three body decay [9, 72, 91]. In remarkable agreement with the results of the kinematic analysis presented in this work, a preferred generation of two coincidentally generated chlorine atoms with small kinetic energies on the one hand and of fast–slow pairs on the other hand was found. We identify the slow–slow atom pairs with those fragments of the synchronous decay and the fast–slow pairs with those of the asynchronous concerted decay. This point of view is supported by the angular constraints for the two chlorine atoms: the statistical analysis yields preferentially the same direction or motion for the two atoms, which in turn corresponds to forward scattering of the CO fragment.

The very good agreement of the two basically different approaches used for the investigation of the phosgene photodissociation cannot be taken for granted; this strengthens our confidence in the presented conclusions. We would like to note at this point that the application of the statistical approach is appropriate in those cases where relatively few experimental data characterizing the system under consideration are available, while in those cases where detailed observations have been made, the kinematic analysis is the method of choice.

7. Concluding remarks

Facing a wide variety of results, experimental methods and analysis procedures, we intended to compile, review and compare the existing data scattered in the literature on molecular three body decay, in response to the increased attention the scientific community has recently paid to this issue. Due to over 70 years of effort in this area, including almost 30 years of interest in the dynamics of three body decays, it is very unlikely that we have not left anything or anybody out, and we would like to apologize to all of those whose contributions do not appear within this work. We believe, however, that each contribution leads to a deeper understanding of molecular three body decay, and, hopefully, will stimulate further research on this topic.

A number of experimental approaches were discussed in some detail, namely photofragment spectroscopy with its numerous variations, and coincidence measurements which could become a much more valuable tool in this field than they are today. We also discussed existing kinematic and statistical data analysis procedures, and the applications to a large number of molecules, including azomethane, acetone and acetyl compounds, all of which have been intensively studied in the last few months.

Additionally to reviewing the existing data, a novel approach is presented for analysing the dynamics of molecular systems undergoing three body decay with the objective of characterizing the system in terms of concertedness and synchronicity. The approach is based on kinematic analysis under strict application of conservation laws. The definition of decay mechanisms with the introduction of physically meaningful parameters and the consequent consideration of parameter distributions allows us to gain detailed insight into the dissociation dynamics without requiring wave packet evolution calculations or the knowledge of the potential energy surface topologies involved.

We analysed the three body decay of phosgene utilizing this approach and obtained a clear picture of the dissociation process. No significant contribution of a

molecular channel, producing chlorine molecules, was found. Likewise, the generation of a stable chloroformyl radical had been ruled out in previous studies, so that every dissociation process upon irradiation around 230 nm yields three fragments, two chlorine atoms and a carbon monoxide molecule. For this three body decay, the asynchronous concerted mechanism is the dominant dissociation channel, accounting for over 80% of the products. The chlorine fragments move preferentially in the same direction, resulting in forward scattering of the carbon monoxide. A less abundant decay channel is the synchronous mechanisms, in which the two bonds cleave in unison and that accounts for the remaining products. The geometry of the decaying parent resembles the ground state equilibrium geometry with significant excitations of the ν_3 in-plane and the ν_4 out-of-plane bending modes. For both mechanisms the CO fragments are generated with high internal excitation.

Our approach is particularly well-suited for molecules of the size of phosgene, which are beyond today's capabilities of performing quantum mechanical calculations, yet simple enough, not to exhibit too many product degrees of freedom that would finally reduce the significance of the results of the kinematic method. In any case, in order to obtain meaningful data, at least one dissociation product has to be experimentally, well characterized, meaning the knowledge of product state and kinetic energy distributions, preferably as a joint distribution matrix. While this method is in no way limited to parent molecules decaying into one or more atomic fragments, the analysis procedure is significantly simplified if this is the case. The procedure may be modified accordingly if the first bond cleavage, for the asynchronous scenarios, allows for arbitrary orientations of the intermediate particle velocity and angular momentum vectors with respect to each other, a case that has not been explicitly dealt with in the present work.

This method is not meant to be a universal tool for the analysis of three body decays. From what has been said above, it should be clear that the application to medium sized molecules is most promising. Medium sized in this context should be understood as being composed of three to six atoms without restrictions on the size of the involved atoms. Some examples of those molecules have been discussed in this work and include, to name a few, methane and methane compounds, simple carbonyl and sulphonyl compounds, but also water and ozone. For small systems consisting of light atoms, quantum mechanical calculations provide a much more detailed picture of the nature of molecular dissociation although the highly excited states involved in the three body decay pose very challenging problems for the theoretician. For large systems of the size of acetone or larger, apart from some qualitative arguments based on product state and kinetic energy distributions, statistical methods remain the appropriate tools.

Acknowledgments

We are indebted to Dr T. Haas for his contributions to the experimental set-up, data acquisition and evaluation, and for numerous fruitful discussions. We would like to thank Professor F. J. Comes and Professor E. A. Reinsch for stimulating discussions, and Professor A. J. Stace for communicating results prior to publication. Financial support of the Deutsche Forschungsgemeinschaft and the Fonds der Chemischen Industrie is gratefully acknowledged.

References

[1] Borden, W. T., Loncharich, R. J., and Houk, K. N., 1988, *Annu. Rev. phys. Chem.*, **39,** 213.

[2] Dewar, M. J. S., 1984, *J. Am. chem. Soc.*, **106,** 209.

[3] (*a*) Woodward, R. B., and Hoffmann, R., 1969, *Angew. Chem. Int. Edn. Engl.*, **8,** 781; (*b*) Woodward, R. B., and Hoffmann, R., 1971, *The Conservation of Orbital Symmetry* (Weinheim: Verlag Chemie, Academic Press).

[4] Hsieh, S., and Eland, J. H. D., 1995, *J. chem. Phys.*, **103,** 1006.

[5] Eland, J. H. D., 1993, *Chem. Phys. Lett.*, **203,** 353.

[6] Nenner, I., and Eland, J. H. D., 1992, *Z. Phys.* D, **25,** 47.

[7] Kim, S. K., Pedersen, S., and Zewail, A. H., 1995, *J. chem. Phys.*, **103,** 477.

[8] North, S. W., Blank, D. A., Gezelter, J. D., Longfellow, C. A., and Lee, Y. T., 1995, *J. chem. Phys.*, **102,** 4447.

[9] Strauss, C. E. M., and Houston, P. L., 1990, *J. phys. Chem.*, **94,** 8751.

[10] Ramsperger, H. C., 1928, *J. Am. chem. Soc.*, **49,** 912.

[11] Ramsperger, H. C., 1929, *J. Am. chem. Soc.*, **51,** 2134.

[12] Norrish, R. G. W., Crone, H. G., and Saltmarsh, O. D., 1934, *J. chem. Soc.*, 1456.

[13] Busch, G. E., Cornelius, J. F., Mahoney, R. T., Morse, R. I., Schlosser, D. W., and Wilson, K. R., 1970, *Rev. Sci. Instrum.* **41,** 1066.

[14] Felder, P., 1994, *Chimia*, **48,** 43.

[15] Schnieder, L., Meier, W., Welge, K. H., Ashfold, M. N. R., and Dixon, R. N., 1990, *J. chem. Phys.*, **92,** 7027.

[16] Mordaunt, D. H., Ashfold, M. N. R., and Dixon, R. N., 1994, *J. chem. Phys.*, **100,** 7360.

[17] Eland, J. H. D., 1987, *Molec. Phys.*, **61,** 725.

[18] Zewail, A. H., 1994, *Femtochemistry: Ultrafast Dynamics of the Chemical Bond* (Singapore: World Scientific).

[19] Khundkar, L. R., and Zewail, A. H., 1990, *Ann. Rev. phys. Chem.*, **41,** 15.

[20] Coggiola, M. J., Schulz, P. A., Lee, Y. T., and Shen, Y. R., 1977, *Phys. Rev. Lett.*, **38,** 17.

[21] Wodtke, A. M., and Lee, Y. T., 1985, *J. phys. Chem.*, **89,** 4744.

[22] Wodtke, A. M., 1986, PhD thesis, University of California, Berkeley, USA.

[23] Zhao, X., 1988, PhD thesis, University of California, Berkeley, USA.

[24] Zhao, X., Nathanson, G. M., and Lee, Y. T., 1992, *Acta Physico-Chim. Sinica*, **8,** 70.

[25] Letokhov, V. S., 1987, *Laser Photoionization Spectroscopy* (Orlando, Florida: Academic).

[26] Henri, V., and Howell, O. R., 1930, *Proc. R. Soc.*, **A128,** 178.

[27] Ashfold, M. N. R., and Howe, J. D., 1994, *Ann. Rev. phys. Chem.*, **45,** 57.

[28] Belbruno, J. J., 1995, *Int. Rev. phys. Chem.*, **14,** 67.

[29] Drabbels, M., Morgan, C. G., McGuire, D. S., and Wodtke, A. M., 1995, *J. chem. Phys.*, **102,** 611.

[30] Zande, W. J. v. d., Zhang, R., Zare, R. N., McKendrick, K. G., and Valentini, J. J., 1991, *J. phys. Chem.*, **95,** 8205.

[31] Chandler, D. W., and Houston, P. L., 1987, *J. chem. Phys.*, **87,** 1445.

[32] Bracewell, R. N., 1986, *The Fourier Transform and its Applications* (New York: McGraw-Hill), p. 262.

[33] Heck, A. J. R., and Chandler, D. W., 1995, *Ann. Rev. phys. Chem.*, **46,** 335.

[34] Eland, J. H. D., 1991, *Vacuum Ultraviolet Photoinization and Photodissociation of Molecules and Clusters*, edited by C. Y. Ng (Singapore: World Scientific), p. 297.

[35] Codling, K., Frasinski, L. J., Hatherly, P. A., and Stankiewicz, M., 1990, *Phys. Scr.*, **41,** 433.

[36] Frasinski, L. J., Codling, K., and Hatherly, P. A., 1989, *Science*, **246,** 1029.

[37] Eland, J. H. D., 1989, *Accts chem. Res.*, **22,** 381.

[38] Wort, F. S., Royds, R. N., and Eland, J. H. D., 1986, *J. Electron Spectrosc. Relat. Phen.*, **41,** 297.

[39] Wiley, W. C., and McLaren, I. H., 1955, *Rev. Sci. Instrum.*, **26,** 1150.

[40] Lavollée, M., and Bergeron, H., 1992, *J. Phys.* B, **25,** 3101.

[41] Herschbach, D. R., 1962, *Disc. Faraday Soc.*, **33,** 149.

[42] Miller, W. B., Safron, S. A., and Herschbach, D. R., 1967, *J. chem. Soc. Faraday Disc.*, **44,** 108.

[43] KROGER, P. M., and RILEY, S. J., 1977, *J. chem. Phys.*, **67,** 4483.
[44] KROGER, P. M., and RILEY, S. J., 1979, *J. chem. Phys.*, **70,** 3863.
[45] SMITH, D. J., and GRICE, R., 1991, *Molec. Phys.*, **73,** 1371.
[46] JARVIS, R. D., LAMING, G. J., and GRICE, R., 1990, *Molec. Phys.*, **70,** 667.
[47] JARVIS, R. D., HARKIN, J. H., SMITH, D. J., and GRICE, R., 1990, *Chem. Phys. Lett.*, **167,** 90.
[48] JARVIS, R. D., and GRICE, R., 1989, *Molec. Phys.*, **66,** 675.
[49] JARVIS, R. D., and GRICE, R., 1988, *Molec. Phys.*, **65,** 1205.
[50] GRICE, R., 1995, *Int. Rev. phys. Chem.*, **14,** 315.
[51] FORD, K. W., and WHEELER, J. A., 1959, *Ann. Phys.*, **7,** 287.
[52] DIXON, R. N., 1986, *J. chem. Phys.*, **85,** 1866; GERICKE, K.-H., KLEE, S., COMES, F. J., and DIXON, R. N., 1986, *Ibid*, 4463.
[53] BUSCH, G. E., and WILSON, K. R., 1972, *J. chem. Phys.*, **56,** 3626.
[54] GEJO, T., FELDER, P., and HUBER, J. R., 1995, *Chem. Phys.*, **195,** 423.
[55] RICE, O. K., and RAMSPERGER, H. C., 1927, *J. Am. chem. Soc.*, **49,** 1617.
[56] KASSEL, L. S., 1928, *J. phys. Chem.*, **32,** 225.
[57] BAER, T., DEPRISTO, A. E., and HERMANS, J. J., 1982, *J. chem. Phys.*, **76,** 5917.
[58] CARNEY, T. E., and BAER, T., 1982, *J. chem. Phys.*, **76,** 5968.
[59] WOODWARD, C. A., UPHAM, J. E., STACE, A. J., and MURRELL, J. N., 1989, *J. chem. Phys.*, **91,** 7612.
[60] STRAUSS, C. E. M., 1990, PhD thesis, Cornell University, Ithaca, USA.
[61] (*a*) GRANDY, W. T., 1985, *Maximum-Entropy and Bayesian Methods in Inverse Problems*, edited by C. R. Smith and W. T. Grandy (Dordrecht: Reichel), p. 1; (*b*) JAYNES, E. T., 1985, *Maximum-Entropy and Bayesian Methods in Inverse Problems*, edited by C. R. Smith and W. T. Grandy (Dordrecht: Reichel), p. 21.
[62] JAYNES, E. T., 1978, *Maximum Entropy Formalism* Cambridge: MIT, p. 15.
[63] SHANNON, C. E., 1948, *Bell System Tech. J.*, **27,** 379, 623.
[64] GERICKE, K.-H., GLÄSER, H. G., MAUL, C. and COMES, F. J., 1990, *J. chem. Phys.*, **92,** 411.
[65] MAUL, C., GLÄSER, H. G., and GERICKE, K.-H., 1989, *J. Chem. Soc. Faraday Trans.*, **2,** 85, 1297.
[66] GERICKE, K.-H., 1988, *Phys. Rev. Lett.*, **60,** 561.
[67] LEVINE, R. D., 1981, *Adv. chem. Phys.*, **47,** 239.
[68] LEVINE, R. D., 1978, *Ann. Rev. phys. Chem.*, **29,** 59.
[69] LEVINE, R. D., 1978, *Maximum Entropy Formalism* (Massachusetts: Cambridge; MIT), p. 247.
[70] BERNSTEIN, R. B., and LEVINE, R. D., 1975, *Adv. atom. molec. Phys.*, **11,** 215.
[71] HAAS, T., 1995, *Charakterisierung naszenter Photofragmente zur Aufklärung der Zerfallsdynamik von Stickstoffwasserstoffsäure und Phosgen* (Frankfurt: Wissenschafts-Verlag Dr. Maraun).
[72] HALL, G. E., VANDENBOUT, D., and SEARS, T. J., 1991, *J. chem. Phys.*, **94,** 4182.
[73] (*a*) JONES, A. B., BUXEY, A. L. M., JUKES, P. R., SMITH, J. A., and STACE, A. J., 1995, *J. chem. Phys.*, **103,** 474; (*b*) STACE, A. J., 1996, private communication.
[74] ENGEL, P. S., 1980, *Chem. Rev.*, **80,** 99.
[75] ANDREWS, B. K., BURTON, K. A., and WEISMAN, R. B., 1992, *J. chem. Phys.*, **96,** 1111.
[76] BURTON, K. A., and WEISMAN, R. B., 1990, *J. Am. chem. Soc.*, **112,** 1804.
[77] ADAMS, J. S., BURTON, K. A., ANDREWS, B. K., WEISMAN, R. B., and ENGEL, P. S., 1986, *J. Am. chem. Soc.*, **108,** 7935.
[78] HOLT, P. L., MCCURDY, K. E., ADAMS, J. S., BURTON, K. A., WEISMAN, R. B., and ENGEL, P. S., 1985, *J. Am. chem. Soc.*, **107,** 2180.
[79] NORTH, S. W., LONGFELLOW, C. A., and LEE, Y. T., 1993, *J. chem. Phys.*, **99,** 4423.
[80] HU, C.-H., and SCHAEFER, H. F. III, 1994, *J. chem. Phys.*, **101,** 1289.
[81] LEE, E. K. C., and LEWIS, R. S., 1980, *Adv. Photochem.*, **12,** 1.
[82] POTZINGER, P., and BÜNAU, G. v., 1968, *Ber. Bunsenges.*, **72,** 195.
[83] LAKE, J. S., and HARRISON, A. J., 1959, *J. chem. Phys.*, **30,** 361.
[84] GAINES, G., DONALDSON, D. J., STRICKLER, S. J., and VAIDA, V., 1988, *J. phys. Chem.*, **92,** 2762.
[85] DONALDSON, D. J., GAINES, G., and VAIDA, V., 1988, *J. phys. Chem.*, **92,** 2766.
[86] WATKINS, K. W., and WORD, W. M., 1974, *Int. J. chem. Kinet.*, **6,** 855.

[87] Brouard, M., McPherson, M. T., Pilling, M. J., Tulloch, J. M., and Williamson, A. P., 1985, *Chem. Phys. Lett.*, **113,** 413.
[88] Lightfoot, P. D., Kirwan, S. P., and Pilling, M. J., 1988, *J. phys. Chem.*, **92,** 4938.
[89] Woodbridge, E. L., Fletcher, T. R., and Leone, S. R., 1988, *J. phys. Chem.*, **92,** 5387.
[90] Donaldson, D. J., and Leone, S. R., 1986, *J. chem. Phys.*, **85,** 817.
[91] Trentelman, K. A., Kable, S. H., Moss, D. B., and Houston, P. L., 1989, *J. chem. Phys.*, **91,** 7498.
[92] Kawasaki, M., Sato, H., Shinohara, H., and Nishi, N., 1987, *Laser Chem.*, **7,** 109.
[93] Ondrey, G. S., and Bersohn, R., 1984, *J. chem. Phys.*, **81,** 4517.
[94] Campbell, R. J., and Schlag, E. W., 1967, *J. Am. chem. Soc.*, **89,** 5103.
[95] Houston, P. L., 1987, *J. phys. Chem.*, **91,** 5388.
[96] North, S. W., Blank, D. A., and Lee, Y. T., 1994, *Chem. Phys. Lett.*, **224,** 38.
[97] Hochstrasser, R. M., and King, D. S., 1975, *J. Am. chem. Soc.*, **97,** 4760.
[98] Zhao, X., Miller, W. B., Hintsa, E. J., and Lee, Y. T., 1989, *J. chem. Phys.*, **90,** 5527.
[99] Nahon, L., Morin, P., Larzilliere, M., and Nenner, I., 1992, *J. chem. Phys.*, **96,** 3628.
[100] Glownia, J. H., and Riley, S. J., 1980, *Chem. Phys. Lett.*, **71,** 429.
[101] Coulter, D., Dows, D., Reisler, H., and Wittig, C., 1978, *Chem. Phys.*, **32,** 429.
[102] Burland, D. M., Carmona, F., and Pacansky, J., 1978, *Chem. Phys. Lett.*, **56,** 221.
[103] Hochstrasser, R. M., and King, D. S., 1976, *J. Am. chem. Soc.*, **98,** 5443.
[104] Karl, R. R. Jr., and Innes, K. K., 1975, *Chem. Phys. Lett.*, **36,** 275.
[105] Scheiner, A. C., Scuseria, G. E., and Schaefer, H. F. III, 1986, *J. Am. chem. Soc.*, **108,** 8160.
[106] Mordaunt, D. H., Ashfold, M. N. R., and Dixon, R. N., 1994, *J. chem. Phys.*, **100,** 7360.
[107] Slanger, T. G., and Black, G., 1982, *J. chem. Phys.*, **77,** 2432.
[108] Stranges, D., Yang, X., Chesko, J. D., and Suits, A. G., 1995, *J. chem. Phys.*, **102,** 6067.
[109] Strauss, C. E. M., Kable, S. H., Chawla, G. K., Houston, P. L., and Burak, I. R., 1991, *J. chem. Phys.*, **94,** 1837.
[110] Wang, H., Chen, X., and Weiner, B. R., 1993, *J. phys. Chem.*, **97,** 12260.
[111] Baum, G., Effenhauser, C. S., Felder, P., and Huber, J. R., 1992, *J. phys. Chem.*, **96,** 756.
[112] Chen, X., Asmar, F., Wang, H., and Weiner, B. R., 1990, *J. phys. Chem.*, **95,** 6415.
[113] Kawasaki, M., Kasatani, K., Sato, H., Shinohara, H., Nishi, N., Ohtoshi, H., and Tanaka, I., 1994, *Chem. Phys.*, **91,** 285.
[114] Chen, X., Wang, H., Weiner, B. R., Hawley, M., and Nelson, H. H., 1993, *J. phys. Chem.*, **97,** 12269.
[115] Jonah, C., Chandra, P., and Bersohn, R., 1971, *J. chem. Phys.*, **55,** 1903.
[116] Pattengill, M. D., 1983, *Chem. Phys.*, **75,** 59.
[117] Baughcum, S. L., and Leone, S. R., 1982, *Chem. Phys. Lett.*, **89,** 183.
[118] Kellman, M. E., Pechukas, P., and Bersohn, R., 1981, *Chem. Phys. Lett.*, **83,** 304.
[119] Tamir, M., Halavee, U., and Levine, R. D., 1974, *Chem. Phys. Lett.*, **25,** 38.
[120] North, S. W., Blank, D. A., and Lee, Y. T., 1994, *Chem. Phys. Lett.*, **224,** 38.
[121] Deshmukh, S., and Hess, W. P., 1944, *J. chem. Phys.*, **100,** 6429.
[122] Deshmukh, S., Myers, J. D., Xantheas, S. S., and Hess, W. P., 1994, *J. phys. Chem.*, **98,** 12535.
[123] Lane, I. C., Meehan, R., and Powis, I., 1995, *J. phys. Chem.*, **99,** 12371.
[124] Calvert, J. G., and Layne, G. S., 1953, *J. Am. chem. Soc.*, **75,** 856.
[125] Norrish, R. G. W., and Griffiths, J. G. A., 1928, *J. chem. Soc.*, 2829.
[126] Osamura, Y., Schaefer, H. F. III, Dupuis, M., and Lester, W. A. Jr., 1981, *J. chem. Phys.*, **75,** 5828.
[127] Osamura, Y., and Schaefer, H. F. III, 1981, *J. chem. Phys.*, **74,** 4576.
[128] Loge, G. W., Parmenter, C. S., and Rordorf, B. F., 1988, *Chem. Phys. Lett.*, **74,** 309.
[129] Hepburn, J. W., Buss, R. J., Butler, L. J., and Lee, Y. T., 1983, *J. phys. Chem.*, **87,** 3738.
[130] Burak, I., Hepburn, J. W., Sivakumar, N., Hall, G. E., Chawla, G. K., and Houston, P. L., 1987, *J. chem. Phys.*, **86,** 1258.
[131] Mordaunt, D. H., Lambert, I. R., Morley, G. P., Ashfold, M. N. R., Dixon, R. N., Western, C. M., Schnieder, L., and Welge, K. H., 1993, *J. chem. Phys.*, **98,** 2054.
[132] Baum, G., Felder, P., and Huber, J. R., 1993, *J. chem. Phys.*, **98,** 1999.

[133] WANNENMACHER, E. A. J., FELDER, P., and HUBER, J. R., 1991, *J. chem. Phys.*, **95,** 986.
[134] REBBERT, R. E., and AUSLOOS, P. J, 1975, *J. Photochem.*, **4,** 419.
[135] KHUNDKAR, L. R., and ZEWAIL, A. H., 1990, *J. chem. Phys.*, **92,** 231.
[136] KNEE, J. L., KHUNDKAR, L. R., and ZEWAIL, A. H., 1985, *J. chem. Phys.*, **83,** 1996.
[137] SAPERS, S. P., and HESS, W. P., 1992, *J. chem. Phys.*, **97,** 3126.
[138] HINTSA, E. J., ZHAO, X., and LEE, Y. T., 1990, *J. chem. Phys.*, **92,** 2280.
[139] NAGATA, T., and KONDOW, T., 1993, *J. chem. Phys.*, **98,** 290.
[140] SMITH, J. A., GOTTS, N. G., WINKEL, J. F., HALLETT, R. A., WOODWARD, C. A., STACE, A. J., and WHITAKER, B. J., 1992, *J. chem. Phys.*, **97,** 397.
[141] GOTTS, N. G., HALLETT, R. A., SMITH, J. A., and STACE, A. J., 1991, *Chem. Phys. Lett.*, **181,** 491.
[142] NAGATA, T., HIROKAWA, J., and KONDOW, T., 1991, *Chem. Phys. Lett.*, **176,** 526.
[143] NAGATA, T., HIROKAWA, J., IKEGAMI, T., KONDOW, T., and IWATA, S., 1990, *Chem. Phys. Lett.*, **171,** 433.
[144] WOODWARD, C. A., WHITAKER, B. J., and STACE, A. J., 1990, *J. chem. Soc. Faraday Trans.*, **86,** 2069.
[145] CHEN, Z. Y., ALBERTONI, C. R., HASEGAWA, M., KUHN, R., and CASTLEMAN, A. W. JR., 1989, *J. chem. Phys.*, **91,** 4019.
[146] SNODGRASS, J. T., ROEHL, C. M., and BOWERS, M. T., 1989, *Chem. Phys. Lett.*, **159,** 10.
[147] WOODWARD, C. A., UPHAM, J. E., STACE, A. J., and MURRELL, J. N., 1989, *J. chem. Phys.*, **91,** 7612.
[148] LEVINGER, N. E., RAY, D., ALEXANDER, M. L., and LINEBERGER, W., 1988, *J. chem. Phys.*, **89,** 5654.
[149] KIM, H.-S., JARROLD, M. F., and BOWERS, M. T., 1986, *J. chem. Phys.*, **84,** 4882.
[150] JARROLD, M. F., ILLIES, A. J., and BOWERS, M. T., 1984, *J. chem. Phys.*, **81,** 222.
[151] HABERLAND, H., KOLAR, T., LUDEWIGT, C., RISCH, A., and SCHMIDT, M., 1991, *Z. Phys.* D, **20**, 33.
[152] HABERLAND, H., ISSENDORF, B. V., KOLAR, T., KORNMEIER, H., LUDEWIGT, C., and RISCH, A., 1991, *Phys. Rev. Lett.*, **67,** 3290.
[153] ALBERTONI, C. R., KUHN, R., SARKAS, H. W., and CASTLEMAN, A. W. JR., 1987, *J. chem. Phys.*, **87,** 5043.
[154] MAGNERA, T. F., and MICHL, J., 1992, *Chem. Phys. Lett.*, **192,** 99.
[155] DELUCA, J. J., and JOHNSON, M. A., 1989, *Chem. Phys. Lett.*, **162,** 445.
[156] IKEGAMI, T., NAGATA, T., and KONDOW, T., 1992, *Physics and Chemistry Finite Systems: From Clusters to Crystals*, Vol. I, edited by P. Jena, S. N. Khanna, and B. K. RAO (Dordrecht: Kluwer Academic) p. 417.
[157] BOWERS, M. T., PALKE, W. E., ROBINS, K., ROEHL, C., and WALSH, S., 1991, *Chem. Phys. Lett.*, **180,** 235.
[158] GADEA, F. X., 1991, *Z. Phys.* D, **20,** 25.
[159] GADEA, F. X., and AMARAUCHE, M., 1990, *Chem. Phys.*, **140,** 385.
[160] BÖHMER, H.-U., and PEYERIMHOFF, S. D., 1989, *Z. Phys.* D, **11,** 239.
[161] KUNZ, P. J., and WALDORF, J., 1988, *Z. Phys.* D, **8,** 195.
[162] BÖHMER, H.-U., and PEYERIMHOFF, S. D., 1986, *Z. Phys.* D, **3,** 195.
[163] HESSLICH, J., and KUNZ, P. J., 1986, *Z. Phys.* D, **2,** 251.
[164] WADT, W. R., 1981, *Appl. Phys. Lett.*, **38,** 1030.
[165] MICHELS, H. H., HOBBS, R. H., and WRIGHT, L. A., 1979, *Appl. Phys. Lett.*, **35,** 153.
[166] KEESEE, R. G., and CASTLEMAN, A. W. JR., 1986, *J. phys. Chem. Ref. Data*, **15,** 1011.
[167] HIRAOKA, K., and MORI, T., 1989, *J. chem. Phys.*, **90,** 7143.
[168] BUELOW, S., RADHAKRISHNAN, G., CATARANZITE, J., and WITTIG, C., 1985, *J. chem. Phys.*, **83,** 444.
[169] SHIN, S. K., CHEN, Y., NICKOLAISEN, S., SHARPE, S. W., BEAUDET, R. A., and WITTIG, C., 1991, *Adv. Photochem.*, **16,** 249.
[170] GERBER, R. A., MCCOY, A. B., and GARCIA-VELA, A., 1994, *Ann. Rev. phys. Chem.*, **45,** 275.
[171] ELAND, J. H. D., and SHEAHAN, J. R., 1994, *Chem. Phys. Lett.*, **223,** 531.
[172] ELAND, J. H. D., 1991, *Laser Chem.*, **11,** 259.
[173] P. LABLANQUIE, NENNER, I., MILLIE, P., MORIN, P., ELAND, J. H. D., HUBIN-FRANSKIN, M. J., and DELWICHE, J., 1985, *J. chem. Phys.*, **82,** 2951.

[174] Dujardin, G., Leach, S., Dutuit, O., Guyon, P.-M., and Richard-Viard, M., 1984, *Chem. Phys.*, **88,** 339.
[175] Morin, P., Lavollee, M., and Simon, M., 1993, In Proceedings of the 10th VUV Conference, edited by F. J. Wuilleumier, Y. Petroff, and I. Nenner (Singapore: World Scientific), p. 211.
[176] Le Coat, Y., Ziesel, J.-P., and Guillotin, J.-P., 1994, *J. Phys.* B, **27,** 965.
[177] Sizun, M., Goursaud, S., Ziesel, J. P., Azria, R., and Tronc, M., 1985, *Chem. Phys.*, **95,** 189.
[178] Tronc, M., Ziesel, J. P., Azria, R., Sizun, M., and Goursaud, 1985, *Chem. Phys.*, **95,** 179.
[179] Azria, R., Ziesel, J. P., Abouaaf, R., Bouby, L., and Tronc, M., 1983, *J. Phys.* B, **16,** L7.
[180] Carlson, T. A., and White, R. M., 1966, *J. chem. Phys.*, **44,** 4510.
[181] Green, W. H. Jr., Moore, C. B., and Polik, W. F., 1992, *Ann. Rev. phys. Chem.*, **43,** 591.
[182] Moore, C. B., Weisshaar, J. C., 1983, *Ann. Rev. phys. Chem.*, **34,** 525.
[183] Ondrey, G. S., and Bersohn, R., 1983, *J. chem. Phys.*, **79,** 175.
[184] Maul, C., 1995, *Konkurrierende Dynamik beim Dreikörperzerfall von Molekülen* (Frankfurt: Wissenschafts-Verlag Dr. Maraun).
[185] Helas, G., and Wilson, S. R., 1992, *Atmospheric Environment*, **26A,** 2975.
[186] Wilson, S. R., Crutzen, P. J., Schuster, G., Griffith, D. W. T., and Helas, G., 1988, *Nature*, **334,** 689.
[187] Kindler, T. P., Chameides, W. L., Wine, P. H., Cunnold, D. M., Alyea, F. N., and Frank, J. A., 1995, *J. geophys. Res.*, **100,** 1235.
[188] Robinson, G. W., 1953, *J. chem. Phys.*, **21,** 1741.
[189] Herzberg, G., 1966, *Molecular Spectra and Molecular Structure III, Electronic Spectra and Electronic Structure of Polyatomic Molecules* (New York: Van Nostrand Reinhold).
[190] Ananthakrishnan, R., 1937, *Proc. Ind. Acad. Sci.*, **5A,** 285.
[191] Bailey, C. R., and Hale, J. B., 1938, *Phil. Mag.*, **25,** 98.
[192] Nielsen, A. H., Burke, T. G., Woltz, P. J. H., and Jones, E. A., 1952, *J. chem. Phys.*, **20,** 596.
[193] Catalano, E., and Pitzer, K. S., 1958, *J. Am. chem. Soc.*, **80,** 1054.
[194] Overend, J., and Evans, J. C., 1959, *Trans. Faraday Soc.*, **55,** 1817.
[195] Schneider, B., and Stoker, J., 1961, *Coll. Czech. Chem. Comm.*, **26,** 1221.
[196] Letokhov, V. S., Mashin, V. I., and Puretzky, A. A., 1977, *Progr. Quant. Electr.*, **5,** 139.
[197] LaPaglia, S. R., and Duncan, A. B. F., 1961, *J. chem. Phys.*, **34,** 125.
[198] Giddings, L. E., and Innes, K. K., 1963, *J. Molec. Spectrosc.*, **8,** 328.
[199] Moule, D. C., and Foo, P. D., 1971, *J. chem. Phys.*, **55,** 1262.
[200] Klee, S., 1995, private communication.
[201] Reinsch, E. A., 1995, private communication.
[202] Moore, W. B., Sander, S. P., Howard, C. J., Ravishankara, A. R., Kolb, C. E., Molina, M. J., Golden, D. M., Hampson, R. F., and Kurylo, M. J., 1992, *Chemical Kinetics and Photochemical Data for Use in Stratospheric Modelling*, Pasadena (JPL Publication), p. 92.
[203] Heicklen, J. J., 1965, *J. Am. chem. Soc.*, **87,** 445.
[204] Wijnen, M. H. J., 1961, *J. Am. chem. Soc.*, **83,** 3014.
[205] Okabe, H., 1977, *J. chem. Phys.*, **66,** 2058.
[206] Francisco, J. S., and Li, Z., 1989, *J. phys. Chem.*, **93,** 8118.
[207] Chichinin, A. I., 1993, *Chem. Phys. Lett.*, **209,** 459.
[208] Maul, C., Haas, T., Gericke, K.-H., and Comes, F. J., 1995, *J. chem. Phys.*, **102,** 3238.
[209] Haas, T., Maul, C., Gericke, K.-H., and Comes, F. J., 1993, *Chem. Phys. Lett.*, **202,** 108.
[210] Krupenie, P. H., 1966, *The Band Spectrum of Carbon Monoxide* (Washington DC: National Bureau of Standards 5, USGPO).
[211] Loge, G. W., Tiee, J. J., and Wampler, F. B., 1983, *J. chem. Phys.*, **79,** 196.
[212] Huber, G., and Herzberg, G., 1979, *Molecular Spectra and Molecular Structure IV, Constants of Diatomic Molecules* (New York: Van Nostrand Reinhold).
[213] Okabe, H., 1978, *Photochemistry of Small Molecules* (New York: Wiley).
[214] Clear, R. D., Riley, S. J., and Wilson, K. R., 1975, *J. chem. Phys.*, **63,** 1340.
[215] Huebert, B. J., and Martin, R. M., 1968, *J. phys. Chem.*, **72,** 3046.

[216] MULLIKEN, R. S., 1937, *Phys. Rev.*, **51,** 310.
[217] HERZBERG, G., 1950, *Molecular Spectra and Molecular Structure I, Spectra of Diatomic Molecules* (Princeton: Van Nostrand).
[218] GIBSON, G. E., and BAYLISS, N. S., 1933, *Phys. Rev.*, **44,** 188.
[219] TURNER, L. A., 1926, *Phys. Rev.*, **27,** 397.
[220] RADZIENSKI, L. J., and KAUFMAN, V., 1969, *J. Opt. Soc. Am.*, **59,** 424.
[221] MATSUMI, Y., TONOKURA, K., and KAWASAKI, M., 1992, *J. chem. Phys.*, **97,** 1065.
[222] LEROY, R. J., 1974, *Can. J. Phys.*, **52,** 246.
[223] LI, L., LIPERT, R. J., LOBUE, J., CHUPKA, W. A., and COLSON, S. D., 1988, *Chem. Phys. Lett.*, **151,** 335.
[224] TONOKURA, K., MATSUMI, Y., KAWASAKI, M., and KASATANI, K., 1991, *J. chem. Phys.*, **95,** 5065.
[225] BASHKIN, S., and STONER, J. O., 1975, *Atomic Energy Levels and Grotian Diagrams I* (Amsterdam: North-Holland).
[226] MOORE, C. E., 1949, *Atomic Energy Levels*, Circular 467, National Bureau of Standards.
[227] BASHKIN, S., and STONER, J. O., 1978, *Atomic Energy Levels and Grotian Diagrams II* (Amsterdam: North-Holland).
[228] AREPALLI, S., PRESSER, N., ROBIE, D., and GORDON, R., 1985, *Chem. Phys. Lett.*, **118,** 88.
[229] HALPERN, J. B., ZACHARIAS, H., and WALLENSTEIN, R., 1980, *J. molec. Spectrosc.*, **79,** 1.
[230] BRAY, R. G., and HOCHSTRASSER, R. M., 1976, *Molec. Phys.*, **31,** 1199.
[231] SPIGLANIN, T. A., and CHANDLER, D. W., 1987, *Chem. Phys. Lett.*, **141,** 428.
[232] JONES, V. T., and COON, J. B., 1969, *J. molec. Spectrosc.* **31,** 137.
[233] LOMBARDI, J. R., 1970, *J. chem. Phys.*, **52,** 6126.